CP AND THE THREE PION DECAY OF THE K^{O}

Thesis by

Michael Leigh Mallary

In Partial Fulfillment of the Requirements

for the Degree of

Doctor of Philosophy

California Institute of Technology

Pasadena, California

1972

(Submitted December 10,1971)

ACKNOWLEDGEMENTS

I am especially grateful to my research advisor, Professor Frank Sciulli, whose idea it was to perform this experiment. His advice, encouragement, patience, and sense of relevance have been invaluable in my education. It has also been both personally and professionally gratifying to have worked with Professors David Binnie, Ricardo Gomez, Charles Peck, Alvin Tollestrup, and Dr. Bruce Sherwood, who assisted in the design and running of this experiment. I am thankful for the contributions and example of Dr. John Gallivan, whose efforts on the companion Ke_3 experiment were invaluable to this experiment. I am grateful for the contribution of Dr. James van Putten who designed and built the lead plate shower chambers.

The contributions of the members of the Lofgren Group and the Bevatron Operating staff of the Lawrence Radiation Laboratory to the preparation and running of this experiment are greatly appreciated. Messrs.W.Friedler,H.Grow, A.Lake, S. Sedleniek, D. Sell, and D. Toomer assisted in the design and the construction of the equipment. Messrs. D. Chu, P. Walden, K. Young, G. Murata, and J. Stanley helped in the set up and the running of this experiment. Messrs. J. Bridenthal, C. Lam, D. Molodowitch, J. Tam and L Young assisted in the data reduction. The scanning and measuring was supervised by J. Ferrari and the staff included J. Bruce, J. Edwards, M. Jolliff, M. Jorden, J. Lyon and G. Martin. Finally I am grateful to Linda Griffin for a fine effort in typing this manuscript.

The financial support of the National Science Foundation and the Atomic Energy Commission is greatly appreciated.

ABSTRACT

The time distribution of the decays of an initially pure K^o beam into $\pi^+\pi^-\pi^o$ has been analyzed to determine the complex parameter W (also known as η^{+-o} and (x + iy)). The K^o beam was produced in a brass target by the interactions of a 2.85 GeV/c π^- beam which was generated on an internal target in the Lawrence Radiation Laboratory (LRL) Bevatron. The counters and hodoscopes in the apparatus selected for events with a neutral (K^o) produced in the brass target, two charged secondaries passing through a magnet spectrometer and a γ-ray shower in a shower hodoscope.

From the 275K apparatus triggers, 148 $K \rightarrow \pi^+\pi^-\pi^o$ events were isolated. The presence of a γ-ray shower in the optical shower chambers and a two-prong vee in the optical spark chambers were devices used to isolate the events. The backgrounds were further reduced by reconstructing the momenta of the two charged secondaries and applying kinematic constraints.

The best fit to the final sample of 148 events distributed between .3 and 7.0 K_S lifetimes gives:

$$\mathrm{ReW} = -.05 \pm .17$$

$$\mathrm{ImW} = +.39 \begin{matrix} +.35 \\ -.37 \end{matrix} .$$

This result is consistent with both CPT invariance (ReW = 0) and CP invariance (W = 0). Backgrounds are estimated to be less than 10% and systematic effects have also been estimated to be negligible.

An analysis of the present data on CP violation in this decay mode and other K^o decay modes has estimated the phase of ϵ to be 45.3 ± 2.3 degrees. This result is consistent with the super weak theories of CP

violation which predicts the phase of ϵ to be 43^{o}. This estimate is in turn used to predict the phase of η^{oo} to be 48.0 ± 7.9 degrees. This is a substantial improvement on presently available measurements. The largest error in this analysis comes from the present limits on W from the world average of recent experiments. The $K \rightarrow \pi u \nu$ mode produces the next largest error. Therefore further experimentation in these modes would be useful.

TABLE OF CONTENTS

LIST OF FIGURES

Page

CHAPTER I - INTRODUCTION

The observation of the decay $K_L \rightarrow \pi^+\pi^-$ [1], and of interference between the K_S and K_L decays into $\pi^+\pi^-$ provides compelling evidence of a CP violation in the K^o - $\bar{K}^o$ system (see Appendix I). The observed CP violating amplitudes are of a magnitude of 2×10^{-3} of the CP conserving amplitudes. This observed CP violation could arise from a CP violation in the K^o and $\bar{K}^o$ transition amplitudes to 2π or from a CP violation in the K_S, K_L states (that is, K_S and K_L might not be eigenstates of CP). Present evidence[2] indicates that the first hypothesis cannot account for the observed effects in the 2π decay mode. On the other hand, the observation[3] of a charge asymmetry in the decays $K_L \rightarrow \pi^{\pm}e^{\mp}\nu$ demonstrate that the K_L state is not an eigenstate of CP.

In order for the K_S and K_L states not to be eigenstates of CP (assuming CPT invariance), it is necessary for K^o to $\bar{K}^o$ CP violating transitions to occur. These transitions might occur directly (super weak interaction theories) or through intermediate states (on and/or off the mass shell). Numerous conjectures[4] have been made as to the origin of this CP violating K^o-$\bar{K}^o$ transition. Glashow[5] has proposed that this transition might occur through a 3π intermediate state. This theory suggests that a maximal CP violation would also occur in the transition amplitudes for K^o and $\bar{K}^o$ into 3π in order to account for the size of the observed effect in $K \rightarrow 2\pi$. (A maximal violation means that the CP conserving amplitude is comparable to the CP violating amplitude.)

The three-body pion decays which we shall consider,

$$K^o \rightarrow \pi^+ + \pi^- + \pi^o \qquad (1.1a)$$

$$\bar{K}^o \rightarrow \pi^+ + \pi^- + \pi^o \qquad (1.1b)$$

primarily occur with final states of total isotropic spin I = 1. This is due to centrifugal barriers impeding other states (see Appendix II). If we define the complex amplitude for reaction (1.1a) as $Ye^{i\varphi}$ and the amplitude for reaction (1.1b) as $-\bar{Y}e^{i\bar{\varphi}}$, then CPT requires $Y = \bar{Y}$ and CP requires $\varphi = \bar{\varphi}$ and $Y = \bar{Y}$ (see Appendix III). Cabibbo[6] has shown that, assuming CPT invariance and the $|\Delta I| = 1/2$ rule for nonleptonic decays, the rates for K_L^o and K_S^o decay are, approximately,

$$\Gamma(K_L^o \rightarrow \pi^+\pi^-\pi^o) = \tfrac{1}{2}P\Gamma(K^+ \rightarrow \pi^+\pi^+\pi^-)\cos^2\frac{\varphi-\bar{\varphi}}{2} \qquad (1.2a)$$

$$\Gamma(K_S^o \rightarrow \pi^+\pi^-\pi^o) = \tfrac{1}{2}P\Gamma(K^+ \rightarrow \pi^+\pi^+\pi^-)\sin^2\frac{\varphi-\bar{\varphi}}{2}\ , \qquad (1.2b)$$

where $P = \pi^+\pi^-\pi^o/\pi^+\pi^+\pi^-$ is the phase space ratio.

Using recent data[7] on the K_L^o, K^+ decay rates, Equation (1.2a) gives

$$\varphi - \bar{\varphi} = 50^o \pm 6\ ,$$

predicting

$$\frac{\Gamma(K_S^o \rightarrow \pi^+\pi^-\pi^o)}{\Gamma(K_L^o \rightarrow \pi^+\pi^-\pi^o)} = .150\ {}^{+\ .017}_{-\ .023}\ .$$

This is similar to the maximal CP violation as described by Glashow and is not ruled out by present data on K_S^o decay (see Chapter V).

The purpose of this experiment is to search for a maximal CP violation in the decay amplitudes for K^o and $\bar{K}^o$ into 3π. In order to measure these amplitudes we observed the time distribution of the decay

of an initially pure K^o beam into $\pi^+\pi^-\pi^o$ over the range of times from .3 to 7 K_S lifetimes. In this time range interference between the CP forbidden transition $K_S \rightarrow 3\pi$ and the CP allowed transition $K_L \rightarrow 3\pi$ (see Appendix III) would be evidence of a CP violation. If we define the ratio of these two amplitudes to be:

$$W = \frac{\langle \pi^+\pi^-\pi^o | H_w | K_S \rangle}{\langle \pi^+\pi^-\pi^o | H_w | K_L \rangle} \tag{1.3}$$

then the time distribution of the decays in this experiment (from a K^o beam) is:

$$F(t) \sim e^{-t/\tau_L} + |W|^2 e^{-t/\tau_S} + 2\left[\mathrm{ReW}\cos(\Delta mt) - \mathrm{ImW}\sin(\Delta mt)\right] e^{-\frac{t}{2}\left(\frac{1}{\tau_L}+\frac{1}{\tau_S}\right)} \tag{1.4}$$

where τ_S and τ_L are the K_S and K_L lifetimes and Δm is the absolute value of the mass difference between the K_S and K_L.

Assuming that the I = 1 3π states are dominant (see Appendix III) it can be shown that $\mathrm{ReW} \neq 0$ is a violation of CPT invariance and $W \neq 0$ is a violation of CP invariance. In this experiment the resolution on ReW is $\pm$ .17 and the resolution on ImW is $\pm$ .35. Therefore a maximal CP violation ($\mathrm{ImW} \sim 1$) would be detectable.

Beyond the possibility of observing a large CP violation in this mode, the measurement of W is of use in various sum rules. The sum rule (the sum is over the final states (f) available to K^o decay and ζ_f is the phase space):

$$\left[i(m_L - m_S) + 1/2\ \gamma_S\right]\langle K_S | K_L \rangle = \pi \sum_f \zeta_f \langle f | T | K_S \rangle \langle f | T | K_L \rangle \tag{1.5}$$

has been used by Schubert[8] to demonstrate that the present data on CP violation in K^o decay is consistent with CP and T violation and

at the same time it is consistent with CPT conservation. The contribution to this sum from the 3π mode is $W\gamma_{K_L \to \text{all } 3\pi}$.

Lee and Wu[9] have shown that the sum

$$\Gamma_{K\bar{K}} = \sum_f \pi\zeta_f \left[\langle K|H_w|3\pi\rangle\langle 3\pi|H_w|\bar{K}\rangle - \langle \bar{K}|H_w|3\pi\rangle\langle 3\pi|H_w|K\rangle \right] \qquad (1.6)$$

can be used (assuming CPT invariance) to determine the phase of ϵ. The K_S and K_L states are defined in terms of ϵ and the K^o and $\bar{K}^o$ states by:

$$\begin{aligned} |K_S\rangle &= \left[(1+\epsilon)|K^o\rangle + (1-\epsilon)|\bar{K}^o\rangle\right] / \sqrt{2(1+|\epsilon|^2)} \\ |K_L\rangle &= \left[(1+\epsilon)|K^o\rangle - (1-\epsilon)|\bar{K}^o\rangle\right] / \sqrt{2(1+|\epsilon|^2)} \quad . \end{aligned} \qquad (1.7)$$

The contribution to this sum from the 3π mode is $i\text{Im}W\gamma_{K_L \to \text{all } 3\pi}$. Presently the limits on the accuracies of these sums (equations 1.5 and 1.6) come from the Ke_3 modes and the $K \to 3\pi$ modes. This will be discussed further in Chapter V.

To conclude this discussion, the measurement of W can determine whether or not there is a maximal CP violation in $K \to 3\pi$ and possibly account for the observed CP violations in other decay modes. Further, the experimental limits placed on W are of aid in refining our knowledge of the CP and CPT (ϵ and δ[10]) violating parameters in the K_S and K_L states.

CHAPTER II - APPARATUS

The purpose of this experiment was to observe the time distribution of the decay of an initially pure K^o beam into π^+, π^-, π^o. In order to do this the apparatus (Figure 1) had three main parts: the Production-Decay Region (I), in which the K^o's were produced and their decay observed, the Momentum Spectrometer Region (II), in which the momentum of the charged secondaries was measured, and the Shower Region (III). In the latter region, gamma rays from the decay of the π^o were observed to shower in lead plate shower chambers. In this region the charged secondaries were observed not to shower (not electrons). The invariant mass of the charged secondaries (from region II) and the presence of at least one gamma ray shower from region III were devices used to eliminate backgrounds. The position distribution in region I of the vertex of the "vee" formed by the charged secondaries together with a knowledge of the momentum distribution of the K^o's were used to infer the time distribution of the decay $K \rightarrow \pi^+ \pi^- \pi^o$.*

The following five sections of this chapter are devoted to a more detailed description of these three regions of the apparatus and a more precise description of the triggering and the data recording.

I. Production-Decay Region

In this region of the apparatus (Figure 2) K^o were produced in a brass target by a 2.85 Gev π^- beam. Some typical reactions for producing K^o at this energy are:

---

* Information regarding the K^o momentum distribution was obtained by observing $K_S \rightarrow \pi^+\pi^-$ in calibration runs which were designed to trigger on this mode.

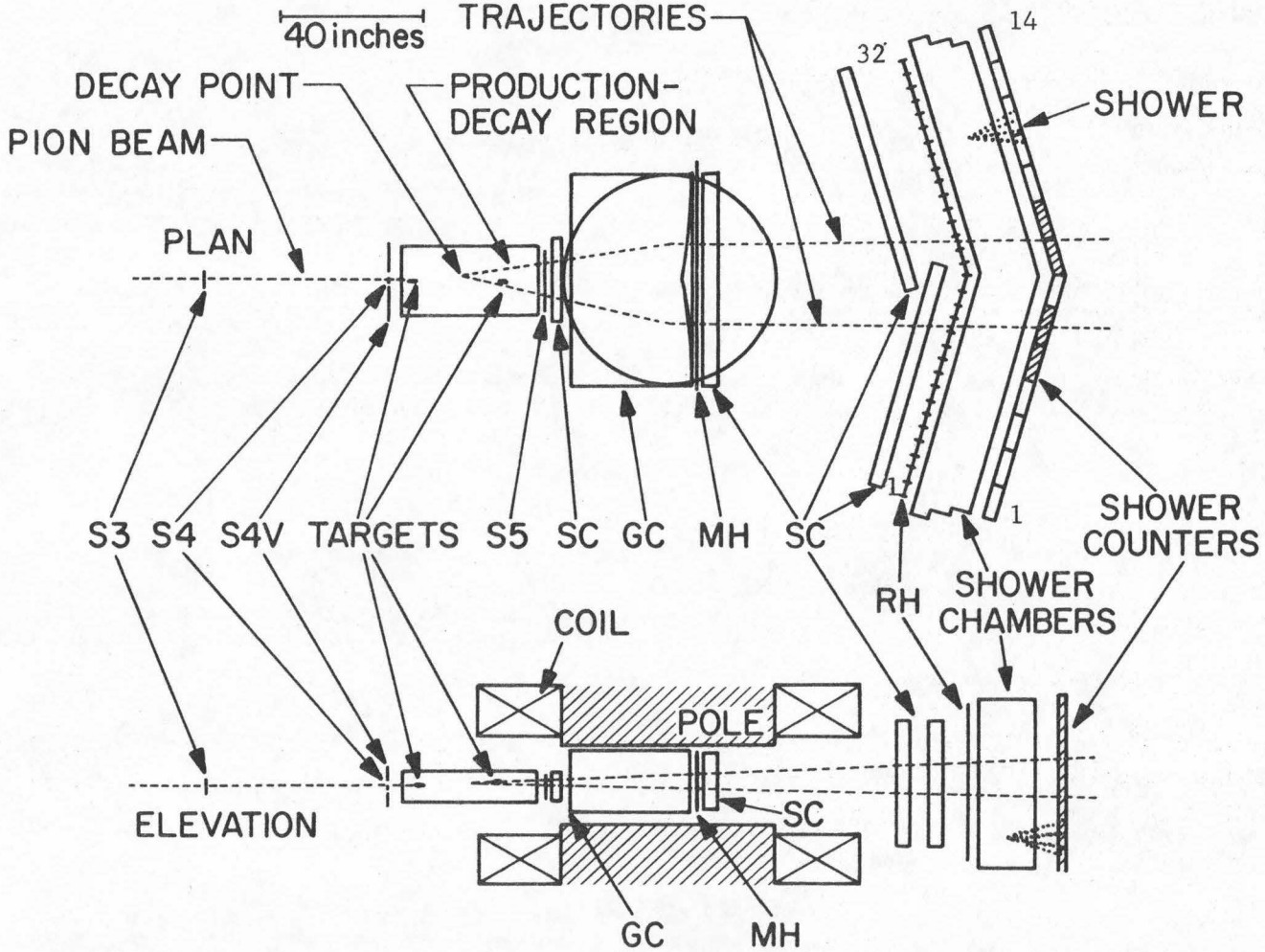

Figure 1 - The Apparatus.

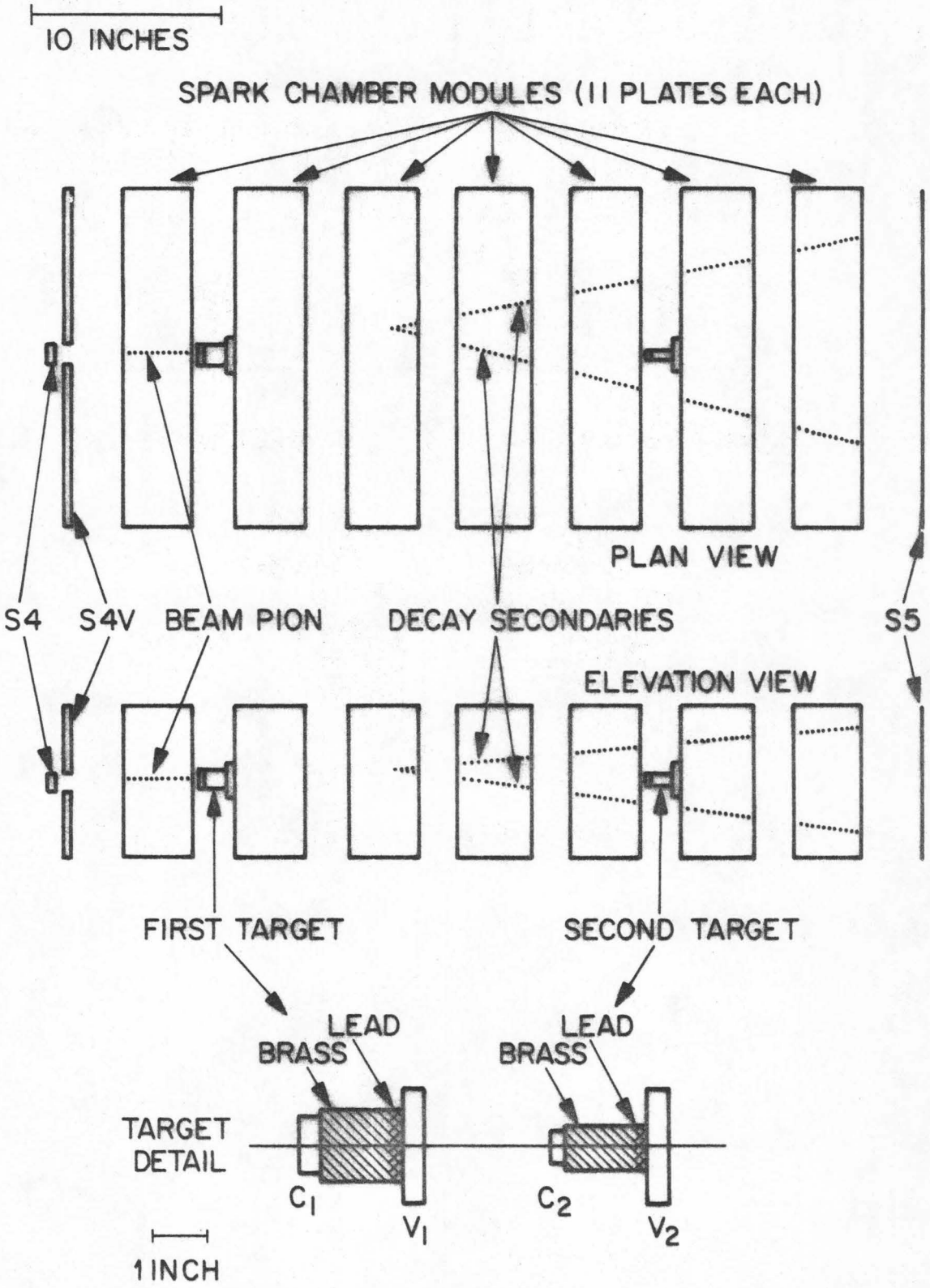

Figure 2 - The Production-Decay Region of the Apparatus.

$$\pi^- + p \rightarrow K^o + \Lambda \tag{2.1}$$

$$\pi^- + p \rightarrow K^o + \Lambda + \pi^o \tag{2.2}$$

$$\pi^- + p \rightarrow N + K^o + \overline{K}^o \tag{2.3}$$

The π^- beam (see Appendix IV) entered this region of the apparatus through counter S4. After passing through a spark chamber module which defined the spatial position of the incident beam particle, it entered the first brass target through counter C1. The π^- beam particle passed through the target and the veto counter V1 directly in back of the target without interacting 92% of the time. Most of the time when the beam particle interacted in the target it produced charged forward secondaries which triggered V1 and thus vetoed the event. In 10% of the interactions no charge forward secondaries were produced. These events are described by the notation $C1 \cdot \overline{V1}$ indicating that a beam pion triggered C1 but neither the beam nor a charged secondary triggered V1.

In addition to the first target there was a second target located 24" downstream of the first. The second target received 30% of the beam particles that passed through the first without interacting. The sequence $C_2\overline{V}_2$ from this target could also trigger the apparatus. The events from this target were not used in the final data sample because the background problems were worse and the information content of these events was small in comparison to the events from the first target.

The counter S5 fired 10% of the time in which a $C1\overline{V1}$ sequence occurred. The sequence $C1 \cdot \overline{V1} \cdot S5$ indicates that a beam particle produced a forward neutral in the target T1. The forward neutral (K, Λ, γ, or N) propagated past V1 into the decay region where it decayed or

interacted and produced charged secondaries. One or both of the charged secondaries passed through and triggered S5.

The decay region from T1 to S5 was 35" long (equivalent to 7 K_S life times at the mean K^o momentum). In this region there were six spark chamber modules for observing the "vee". The combined mass of these modules is .06 radiation lengths and .02 collision lengths.

II. Momentum Spectrometer Region

From the Production-Decay Region the secondaries entered the aperture of the momentum analyzing magnet. This magnet had a pole piece 60" in diameter and a 22" gap. Approximately 2/3 of the data was taken at 2.0 Kg and 1/3 at 2.8 Kg. The momentum resolution was 7%. The total material traversed was .05 radiation lengths.

On entering this region the secondaries passed through a spark chamber module (6 gaps) and into a gas Cerenkov counter containing freon at a pressure of one atmosphere (see Appendix VI). This counter would trigger on electrons but not on pions with an efficiency of 97%. It was used in veto in the data reduction thus rejecting events with electron secondaries. The pulse height from this counter was recorded for each event.

After leaving the gas counter at the center of the magnet, the secondaries passed through the Multiples Hodoscope counters (MH on Figure 1) and another spark chamber module (4 gaps). The MH counter consisted of 15 counters, 1 inch wide, oriented horizontally. The trigger required that two of these counters fire thus indicating two secondaries.

Next the secondaries exited from the back of the magnet and passed through another spark chamber module (6 gaps) and through the Rear Hodoscope counter (RH). The RH consisted of 32 counters, 4 inches wide, oriented vertically. The trigger required that 2 RH counters fire, reinforcing the requirement of 2 charged secondaries. In 85% of the data the secondaries were required to be on opposite sides of the RH. That is, one was required to go through RH #1-#16 and the other through RH #17-#32. In the remaining 15% of the data this requirement was not made.

III. Shower Region

After passing through the RH counters, the secondaries entered the shower chambers. There were 3 modules with 6 plates and 1 radiation length per module. If the secondaries were not electrons they passed through the shower chamber unimpeded approximately 80% of the time (approximately 20% of the time hadrons interacted). If they were electrons they would initiate an electron shower.

Directly in back of the shower chambers was a shower hodoscope of 14 sandwiched counters, 10" wide, oriented vertically. The sandwich consisted of a 3/8 inch thick piece of scintillator followed by 2 radiation lengths of lead followed by another piece of scintillator. Each scintillator had its own photo tube. The pulses from the 2 photo tubes were added and the sum for each of the 14 counters was part of the recorded data.

The role the shower counters played in the trigger was to enrich the events with associated gamma ray showers. A gamma ray that originated in the Production-Decay Region (either at the production point or the

decay point) could propagate freely through the system until it reached the 3 radiation lengths of lead in the shower chambers and the 2 radiation lengths in the shower counters. The chances of it not converting in the shower chambers is 5%. Once a gamma ray conversion has occurred the shower propagates back to the shower counters where it can leave a pulse between 0 and 7 times minimum ionizing. If the sum of the pulses on either side (SHC #1-#7 or #8-#14) was greater than 3 times minimum ionizing the trigger requirement of the shower counters was met.

In the data where the charged secondaries were required to be on opposite sides, this shower requirement could be met by the sum of a 2 times minimum ionizing shower and a minimum ionizing charged secondary. In the data where the charged particles could be on the same side, the trigger requirement could be met simply by one or both particles producing slightly greater than minimum ionizing pulses on the same side. When the charged particles were on the same side the shower was required to be on the opposite side in the final sample but not in the trigger.

IV. Triggering

To summarize the previous three sections, the apparatus was triggered by the following sequence of events: a 3 GeV π^- propagates through the beam tube and triggers counters S1, S2, S3, S4, and passes through a hole in S4V failing to trigger it. It then enters the target triggering counter C1 and interacts in the brass to produce a forward K^o which does not trigger counter V1. The K^o decays into $\pi^+\pi^-\pi^o$. The charged pions propagate through the spectrometer triggering S5, 2 MH counters and

2 RH counters. A gamma ray from the π^o decay propagates through the spectrometer and converts in the shower chambers where together with one of the charged pions it must leave a pulse greater than 3 times minimum ionizing (SH).

Under normal conditions $2x10^5$ π^- beam particles satisfying S3·S4·S4V entered the apparatus during 1 Bevatron pulse. On the average, only .38 T1 events per beam pulse occurred which satisfied the above trigger requirements. The effect of the various counter requirements are shown in Table 1.

V. Data Recording

The data for this experiment consisted of spark chamber information recorded on 3 frames of 35 mm film and counter information (both digital and analog) recorded on magnetic tape. There were two types of recording. The first type consisted of events which only partially fulfilled the above trigger requirements. This type of event generated a magnetic tape record but no film record. The second type of event was called a "pix" event because the spark chambers were fired thus generating a picture and a record on magnetic tape. Pix events occurred when the logic requirements for isolating $K^o \rightarrow \pi^+\pi^-\pi^o$ or $K^o \rightarrow \pi^{\pm}e^{\mp}\nu$ were satisfied. Calibration runs were also taken in which the logic requirements for events of the form $K^o \rightarrow \pi^+\pi^-$ could also generate pix events.

Both a plan view and a side view of all the spark chambers (labeled SC) in Figure 1 were photographed. In order to accomplish this, three separate optical systems with three separate cameras were employed. The division of the optics corresponds to the divisions of the first three sections of this chapter. That is, the Production-Decay Region, the

Required Counters	Added Counters	Purpose of Addition	Number of Successes Per Beam Pulse
$S_1 \cdot S_2$	$S_1 \cdot S_2$	Defines primary beam focus.	4.4×10^5
$S_1 \cdot S_2 \cdot S_3 \cdot S_4 \cdot \overline{S_4 V}$ *	$S_3 \cdot S_4 \cdot \overline{S_4 V}$	Defines beam in the production decay region.	2×10^5
(Beam)$\cdot C_1 \cdot \overline{V}_1$	$C_1 \cdot \overline{V}_1$	Suggests that a neutral has been produced in T1.	630
(Beam)$\cdot C_1 \cdot \overline{V}_1 \cdot S_5$	S_5	Implies that the neutral has decayed in the Production Decay Region.	63
(Beam)$\cdot C_1 \cdot \overline{V}_1 \cdot S_5 \cdot$MH$\cdot$RH	MH$\cdot$RH	Requires two charged secondaries in the MH and RH hodoscope apertures.	4.5
(Beam)$\cdot C_1 \cdot \overline{V}_1 \cdot S_5 \cdot$MH$\cdot$RH$\cdot$NS	NS	Requires that the two secondaries be on opposite sides of the RH.	2.2
(Beam)$\cdot C_1 \cdot \overline{V}_1 \cdot S_5 \cdot$MH$\cdot$RH$\cdot$NS$\cdot$SH	SH	Requires a 3 times minimum pulse on at least one side of the shower counters. This favors events with a γ-ray shower.	.38

*The combination $S_1 \cdot S_2 \cdot S_3 \cdot S_4 \cdot \overline{S_4 V}$ is represented by (Beam) in subsequent rows. $\overline{X}$ indicates that counter X is in veto (- = veto).

TABLE 1 - T1 Event Counter Requirements

Momentum Spectrometer Region, and the Shower Chamber Region. The plan view of the spark chambers just up stream of the RH (see Figure 1) appeared on the Shower film while both views of these chambers appeared on the Spectrometer film. While the Momentum Spectrometer film was used exclusively for track reconstruction and charge and momentum analysis, the film from the other two sections was used for scanning as well as momentum analysis.

As stated above, magnetic tape records were written for both the events that fully satisfied the pix requirements and for the ones that only partially satisfied them. The information in these records came from the various counters in both digital (on-off) and analog (pulse height) forms. The digital information was temporarily stored in a buffer (BS-1, Figure 3). The pulse heights were stored as charges in a bank of capacitors. After the spark chambers had fired, the computer read the digital information out of the buffer and directed the translation of the capacitor charges into 6 bit numbers. Thus the analog pulse heights were represented in the set of integers from 1 to 63. Pulse heights that corresponded to numbers greater than 63 were stored as the number 63. These 6 bit numbers were stored in pairs as 12 bit words in the computer memory. Similarly the digital information was combined into 12 bit words for storage, e.g., 12 counters to 1 computer word. After 3 events (both pix and non pix events) were accumulated in the memory of the computer, they were written as one record on the magnetic tape. In addition to recording this information, the computer kept histograms of various quantities as a check on the performance of the apparatus.

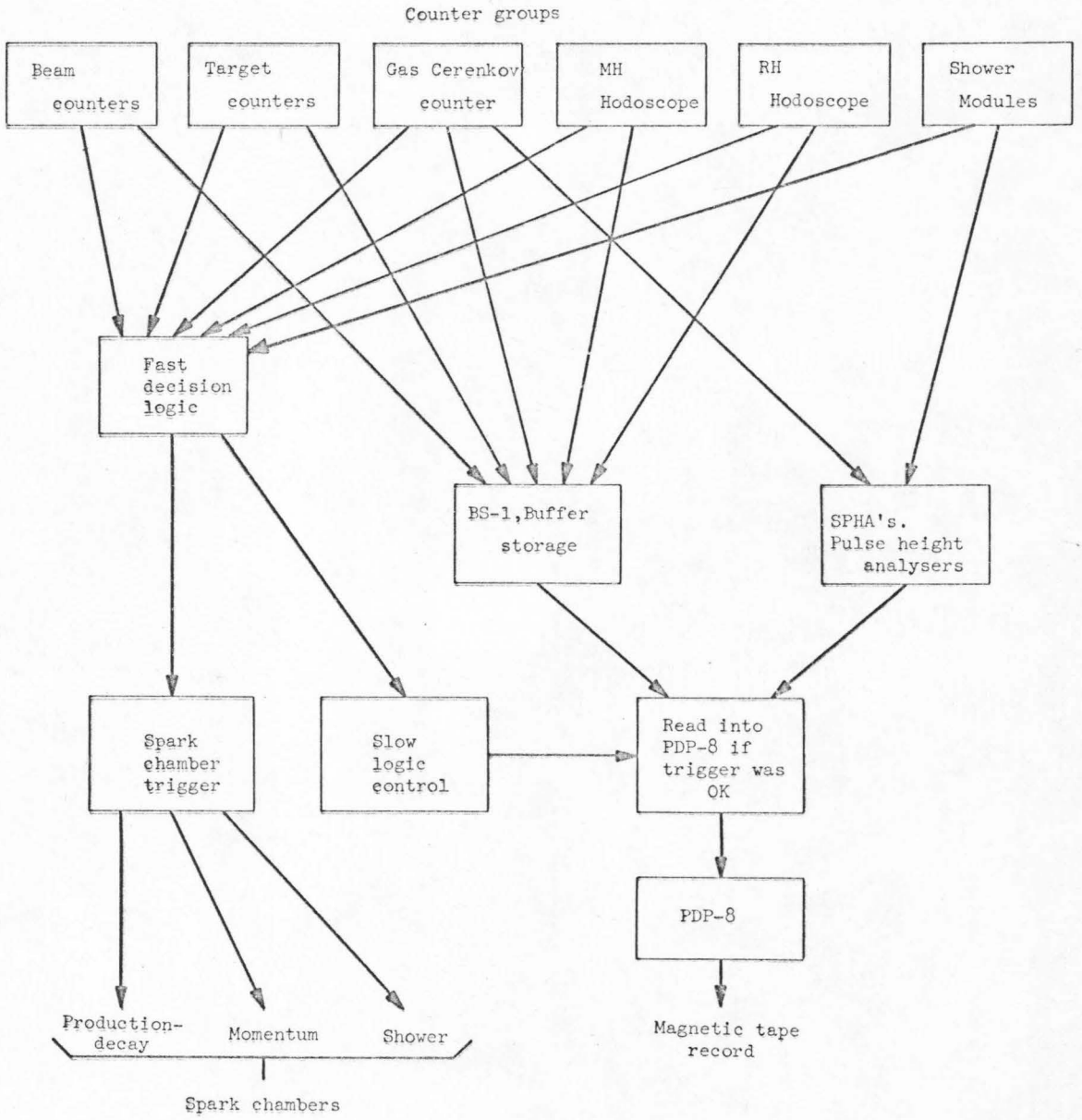

Figure 3 - Block Diagram of Data Recording and Triggering Logic.

From January to April 1968, 900 K pictures were taken with this apparatus of which 275 K were good $K \rightarrow \pi^+\pi^-\pi^o$ triggers. The magnetic field was reversed 25 times during this period. The total data taken at each polarity was the same. This was done to cancel out any geometric charge asymmetric effects in the apparatus. This was not so important for this experiment but was necessary for the Ke_3 experiment which was done in tandem with this one. Appendix XIII contains additional information on running procedures and checks on the apparatus. The reduction of these 275 K pictures to 148 final sample events is discussed in the next chapter.

CHAPTER III - DATA REDUCTION

The data reduction process in this experiment extracted 148 $K^o \rightarrow \pi^+ \pi^- \pi^o$ events from 275,664 apparatus trigger events. The principle backgrounds came from $K^o \rightarrow \pi^+ \pi^-$ events and $\Lambda \rightarrow p \pi^-$ events. These backgrounds occur 10^3 times more frequently than the signal and therefore require a reduction factor of $\approx 10^4$. This reduction was achieved in two ways. A reduction of 10^2 was obtained by requiring at least one associated gamma ray with each event. The gamma ray had to produce a visible photon shower in the shower chambers and a pulse (> 1.2 minimum ionizing) in the shower counters. A second reduction factor ($\sim 10^2$) was then obtained by the kinematic reconstruction of the events. The measured parameters enabled the reconstruction of invariant masses of the charged secondaries under various assumptions about the nature of the particles (whether they were pions or protons). These reconstructed masses then allowed the isolation of the $K \rightarrow \pi^+ \pi^- \pi^o$ events from the remaining background events.

The numerous steps in the data reduction are discussed below in the order in which they were applied. These steps are summarized in Table 2. The visual scan of the Production Decay Region was done late in the process so that it could receive enough attention to avoid biasing the position distribution of the decays.

I. The Computer Scan

The first step in the data reduction was to select likely candidates from the magnetic tape. The program designed for this purpose passed 12% of the candidates from the first target (T1). The events

Step	Purpose	Principle Reason for Failure	Percent Passed	Number Passed
Apparatus trigger	Selected for neutral decays into two charged secondaries with an associated γ-ray.	See Table 1	-	275,664
Computer scan of the magnetic tape.	Enriched the γ-ray concentration by requiring a pulse in a shower counter which was not associated with either charged secondary. Also took only T1 events.	No pulse found (see Table 3)	6.5	17,234
Visual scan shower chambers.	Looked for γ-ray conversions in the correct shower counters and two charged secondaries.	No γ-ray found	25	4,004
Production decay region visual scan.	Find a vee indicating that a neutral decayed into two charged secondaries.	No vee found	59	2,357
Measurement in the shower region and production decay region.	Measured the events and applied straightforward consistency requirements and remeasured poorly measured events.	Vees didn't meet the scanning criteria	85	1,992
Partial reconstruction	Reconstructed the vertex and the two particle trajectories with the above measurements.	Failed to find an acceptable MH counter for a trajectory	84	1,687
χ^2 cut.	Removes candidates with poor trajectories.	$\chi^2>100$ for 4 degrees of freedom.	90	1,523
Momentum Spectrometer measuring and reconstruction.	Reconstructs accurate trajectories and kinematic variables.	Couldn't fit a trajectory.	99	1,509

TABLE 2 - The Data Reduction

Step	Purpose	Principle Reason for Failure	Percent Passed	Number Passed
Shower Rescan	Apply stringent shower chamber criteria.	γ-ray caused by a pion.	68	1,016
Consistency cuts	$\chi^2/r<5$, opposite charges, small GC pulse, aperture cut.	-	88	898
Mass cuts	$M_{\pi^+\pi^-} < .38$ GeV removes $K \rightarrow \pi^+\pi^-$ $M_{p\pi^-} > 1.20$ GeV removes $\Lambda \rightarrow p\pi^-$	$M_{p\pi^-} < 1.20$ GeV	18	158
Fiducial volume cut	$9.5" < L < 41.0"$	$L > 41.0"$	94	148

(Continued) TABLE 2 - The Data Reduction

from the second target (T2) were not used because the background problems from this target were worse (the kinematic reconstruction was poor). Also the contribution of the T2 events to the knowledge of the time distribution (only the slope at early times could be extracted) was small compared to the contribution from the T1 events.

The cuts which the computer scan made on the data are summarized in Table 3 in the order in which they were applied. The T2 events were removed, then consistency cuts (#2-#6) were made on the data. These cuts reinforced the demands of the fast trigger logic. Next (cut #7) each of the two charged particles were required to leave a pulse of at least 1/2 minimum ionizing in at least one of two shower counters. The two pairs of shower counters (SHC) for each charged particle were determined from the two triggered Rear Hodoscope counters (RH) by the following formula (the division is "integer division", e.g., 3/2 = 2/2 = 1):

$$(SHC^{\#})_i = \begin{cases} (RH^{\#})_i/2 \\ \text{or} \\ (RH^{\#})_i/2-1 \end{cases} \qquad (3.1)$$

where $1 \leq SHC^{\#} \leq 14$, $2 \leq RH^{\#} \leq 31$; i labels the particle (1 or 2).

On the basis of a Monte Carlo calculation it was determined that only 1% of the pions from $K \rightarrow \pi^+ \pi^- \pi^o$ events would fail to meet this consistency requirement between the RH number and the SHC number. In Figure 1 these shower counters are shaded for the pion trajectories shown (dotted lines). Approximately 10% of the pions are expected to interact in the shower chambers. However, in most cases (80%) the

Cut	Purpose	Percent passed from one step to next
1 - T1	Take events from the first target only.	54
2 - PPG	Requires $\pi\pi\gamma$ trigger.	56
3 - NRH	Number of Rear Hodoscope counters fired is 2.	98
4 - NMH	Number of Multiples Hodoscope counters fired is 2.	97
5 - RH Blank	Reject events where Rear Hodoscope numbers 1 or 32 fired.	97
6 - TARG	Requires that the event be unambiguously T1 or T2 (rejects C1 C2 events).	95
7 - Pion Pulses	Requires a 1/2 minimum or greater pulse in Shower counters for each pion.	77
8 - γ Pulse	Requires a pulse in allowed Shower counter greater than 1.2 minimum ionizing for a γ ray.	19

TABLE 3 - Computer Scan

charged secondaries from the interaction meet the above shower counter pulse height requirements.

After it was determined that a correct shower counter had a pulse for each of the two triggered rear hodoscope counters, the program then looked for shower counters which met the γ-ray selection criteria. The requirements for these counters were:

(1) They must not be in the set of counters calculated from equation (3.1) (the pion counters).

(2) They must be on the same side of the apparatus (SHC numbers 1-7 or 8-14) as the 3 times minimum pulse which caused the fast logic apparatus trigger.

(3) They must have a pulse greater than 1.2 minimum ionizing.

The numbers of the shower counters that met the above criteria were printed out and used in the subsequent visual scan of the shower chambers.

The computer scan described above retained 17,234 T1 events. On the basis of 30 $K \rightarrow \pi^+ \pi^- \pi^o$ events which were isolated without the computer scan and on geometric considerations it is estimated that this process was ($75 \pm 10\%$) efficient at picking up good $K \rightarrow \pi^+ \pi^- \pi^o$ events.

II. The Shower Scan

After the computer scan, a visual scan of the shower chambers was conducted. The purpose of this scan was to find events with two good charged particle tracks corresponding to the two RH counters that fired and at least one good gamma ray shower going into the shower counter(s) designated in the computer scan.

If either of the charged particle tracks were obviously an electron shower, the event was rejected. If any tracks resulting from the charged tracks (interactions and scatterings) went into the shower counter designated for the gamma ray shower, the event was rejected. The charged particle tracks had to produce at least 3 sparks out of the 6 gaps in the first shower chamber module (there were 3 modules for a total of 3 radiation lengths) and its extrapolated trajectory had to be within 1 RH counter of a triggered RH counter.

The minimum amount of showering for an acceptable shower depended on the shower module in which the conversion took place. If the gamma ray converted in the last module then the minimum shower consisted of 3 sparks in a row (---). If it converted in the middle module it had to have at least one spark off to the side (-- ---=---). If the shower began in the first module it had to have at least two sparks in a row off to the side (-- ------ -==----).

The shower scan was 95% efficient at picking up events which satisfied the criteria. During this scan 25% of the events which passed the computer scan were accepted.

III. The Production-Decay Region Scan

This region of the apparatus was scanned for two prong "vees". This indicates the decay of a neutral particle into two charged particles. In order to prevent scanning inefficiencies from biasing the time distribution this region was doubled scanned. The two scanners were 98% and 96% efficient on the raw data which consisted mainly of $K \rightarrow 2\pi$ and $\Lambda \rightarrow p\pi$. The efficiency on the $K \rightarrow 3\pi$ events is not as well

known because of low statistics, but was found to be approximately (96 ± 2%) for each scanner. The efficiency as a function of decay position for the raw data is shown in Table 4.

In order to aid the scanners in finding the "vee", a setup was provided which enabled them to determine which Multiples Hodoscope (MH) counter the track projected into. Tracks originating in the first four spark chamber modules (Figure 2) had to project to within two counters (if #10 was the right one then #8, #9, #10, #11, and #12 were acceptable) of the correct one. If the vee began in the last two modules then the tracks had to project to within three counters of the correct one.

Once the tracks were found that fulfilled this MH requirement, the scanner would try to construct a vee out of them. The vertices of the vees as determined in the two perpendicular views had to agree to within 6 plates (approximately 2 inches) in order for the candidate to be acceptable. If there were any noticeable bends in either of the arms of the vee (greater than 4 degrees) the event was rejected. If either arm passed outside of an aperture located at S5 (Figure 2) the event was rejected. This aperture was set at ± 9 inches in the plan view and ± 5 inches in the side view. After the measuring and reconstruction, this aperture was narrowed to ± 8 inches and ± 4 inches in the two views respectively.

This phase of the scanning passed 59% of the candidates. When a good "vee" was found, the scanner noted the module number and the plate number (11 plates per module) of the vertex of the vee. Any time there was a discrepancy of more than 3 plate numbers (approximately 1 inch in space) between the vertex positions determined by the two scanners

Inches from Target	0.7-3.	3.-9.	9.-15.	15.-21.	21.-27.	27.-33.	Total .7-33.
Percent Efficiency Scanner # 1	98±.5	99±.5	99±1	100^{+0}_{-2}	99±1	95±2	98±.5
Percent Efficiency Scanner # 2	97±.5	98±1	99±1	91±5	93±3	94±2	96±.5

TABLE 4 - Vee Scanning Efficiency

or any time one of them found a vee and the other didn't,the event was examined by a physicist and the discrepancy was resolved. This occurred in 15% of the events which reached this stage of the scanning process.

IV. Measuring and Reconstruction

The computer scan, the shower scan, and the Production-Decay Region scan retained 2357 events. These events were next measured in the spark chambers, in the Shower Region, and the Production Decay Region. The positions and angles of each track in both regions were recorded by a digitized protractor measuring machine (see Appendix VIII for measurement accuracy). Using this information a vertex and a trajectory for each track were reconstructed. Next the events were measured in the Momentum Spectrometer Region using the previously calculated trajectory to aid in the measuring of the relevant tracks. Vertices and trajectories were again fitted using the measurement information from all the spark chambers.

The measuring process was more complicated than the above description. At various stages events could be rejected for a number of reasons. The overall attrition rate was 37%. The first place where events could be rejected was in the checking procedure applied to the Production-Decay Region and the Shower Region measurement. After measuring the events twice, 15% failed to pass this checking procedure. This check required the scanning MH and RH requirements to be met by the measured tracks. It required that the association of the tracks between the two views be consistent between the measurement and the scanning determination. In addition, the vertex positions in the two views had to agree with each other and with the visual determination to 1.5".

The measured events that passed the above checking procedure were then fitted in the computer. First, two lines were constructed connecting the vertex (best fitted vertex) with the position of the tracks in the Shower Region. If these lines failed to pass within one inch of the correct MH counters, the event was rejected; 16% of the events failed this test.

Events that passed the above test were then fitted to a vertex and two trajectories through the magnet. The association of tracks between the Shower Region and the Production Decay Region was determined from the elevation view (top to top, bottom to bottom). If this association didn't work the opposite one was attempted.

Next, a cut was put of the data which eliminated events with tracks whose fit had a chi square greater than 100 for 4 degrees of freedom; 10% of the events were eliminated by this cut. The above cuts mainly removed events with tracks that scattered in the magnet.

The remaining events were then measured in the Momentum Spectrometer Region. The measurer was instructed to measure all tracks and sparks within certain tolerances of the above fitted trajectory. The measurements which were closest to the fitted trajectory were then used to fit a new trajectory. If the calculated chi square per degree of freedom for a given measurement was greater than 18, or if a measurement could not be found within certain tolerances of the original fitted trajectory, then that particular spark chamber was dropped from the fit and a new fit attempted. The Production Decay Region chambers could not be dropped. Also, it was forbidden to drop both the shower chambers and spark chambers just upstream of the Shower Region. The typical track

retained 4 or 5 measurements (spark chambers) out of a maximum of 5. Only 1% of the events failed this final reconstruction.

V. Shower Rescan

The events which reconstructed well were next subjected to a rescan of the shower chambers by a physicist. A breakdown of the events rejected in this rescan is given in Table 5. Overall, 32% of the events were rejected at this stage. The principle reason for rejecting them was that the γ-ray was uncertain for one reason or another.

VI. Consistency Cuts

After the Shower Rescan the following cuts were made on the data in order to purify it further and remove the large $K \rightarrow 2\pi$ and $\Lambda \rightarrow p\pi$ backgrounds. Requiring that the charged secondaries have opposite charge removed 1% of the events. Then, 2% were removed by cutting the Gas Counter pulse at or below 1 (the typical electron pulse was 20). Next, 7% of the data was removed by narrowing the aperture at S5 (see Figure 2) to $\pm$ 8" from the centerline in the plan view and $\pm$ 4" in the elevation view. Tracks passing outside these limits had a large chance of scattering in the walls and the electronics of the spark chambers so these events were rejected. After this, 1.5% of the remaining events were removed by cutting the chi-square per degree of freedom for both tracks individually at 5*. Figure 4 shows the chi-squared distribution of the events before the Shower Rescan.

---

* If all the spark chamber measurements were used there were 16 degrees of freedom for each track.

Reason for Rejecting Event	Percent of those rejected
1) The γ-ray or the γ-ray's pulse was caused by a pion interaction or scattering.	45
2) One or both of the pions was an electron.	9
3) One of the pions couldn't be distinguished from a nearby track (ambiguous).	9
4) The γ-ray began in the first half of the first shower module and lined up well with a track in the spark chamber just up stream (the γ looked like an electron).	14
5) The γ-ray opened by more than 45° indicating a hadronic star.	6
6) Other reasons.	17

TABLE 5 - Shower Rescan Rejects

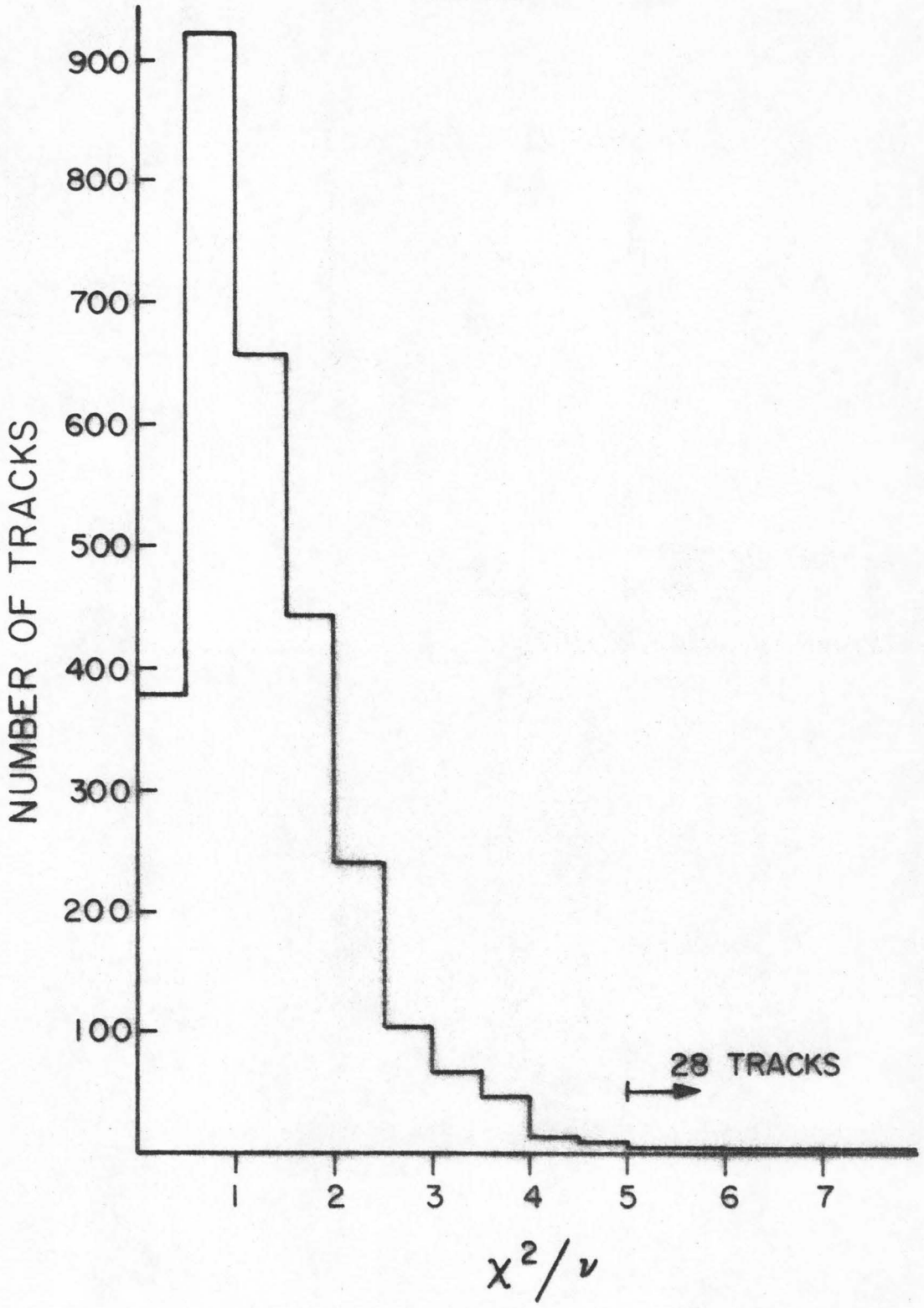

Figure 4 - Chi-square per degree of freedom for reconstructed tracks.

The above cuts removed a total of 10% of the data and were designed to remove events which were questionable. The next two cuts removed events which were not caused by errors in the observation process but were due to physical background processes and so these are discussed in the next section.

VII. Background Cuts

There are numerous physical processes that can lead to an event topography of a neutral particle producing two charged secondaries in association with a γ-ray. The K^o's in this experiment are made by associated production in the brass target:

$$\pi^- + p_{Brass} \rightarrow \Lambda + K^o \tag{3.2}$$

The two principle sources of background in this experiment arise when one of the strange particles in reaction (3.2) decays to a neutral mode (producing π^o's and therefore γ-rays) and the other decays to a charged mode (producing a vee). These reactions are:

$$K_S \rightarrow \pi^+ \pi^- \text{ while } \Lambda \rightarrow N\pi^o \hookrightarrow 2\gamma \tag{3.3}$$

and

$$\Lambda \rightarrow p\pi^- \quad \text{while } K_S \rightarrow 2\pi^o \rightarrow 4\gamma \tag{3.4}$$

Reactions similar to (3.3) and (3.4) can also occur in which the γ-ray comes from π^o production in the target* and the charged secondaries come from K_S and Λ decays. However, the ratio of Λ to K_S decays in the

* There is a 95% chance that one γ-ray from this source will convert in the target and veto the event. See reaction (2.2) with $\pi^o \rightarrow 2\gamma$ and γ+Brass $\rightarrow e^+e^-$.

data indicates that reactions (3.3) and (3.4) are the dominant sources of this type of background.

Another source of background caused by K_S decays is:

$$K_S \rightarrow \pi^+ \pi^- \gamma \qquad (3.5)$$

In order to reduce the background from this source and to remove the background from reactions (3.3) and (3.4) two mass cuts were applied to the data. The K_S background was reduced by removing events with a $\pi^+ \pi^-$ invariant mass, $M_{\pi^+\pi^-}$ (assumes both secondaries are pions), greater than .38 GeV. This removed approximately 250 K_S decays from the data. The background from reaction (3.4) was removed by assuming the positive secondary was a proton and the negative one was a pion. The invariant mass, $M_{p\pi^-}$, was then calculated and events with $M_{p\pi^-} < 1.20$ GeV were removed. This cut induced a charge asymmetry in the data. This offsets the time distribution at the 1% level (through interference with $K_S \rightarrow I = 2$ three-pion state) and is therefore negligible.

The effect of these two cuts on the data can be seen from Figures 5 and 6. Figure 5 is the $M_{p\pi^-}$ distribution with the K_S events removed and Figure 6 is the $M_{\pi^+\pi^-}$ distribution with the Λ events removed. It can be seen that approximately 400 Λ's and 200 K_S's were removed by these cuts*. This left 158 $K \rightarrow \pi^+ \pi^- \pi^o$ events in the peak with $M_{\pi^+\pi^-} < .38$ GeV (Figure 6).

*There were also approximately 150 events that could have been either Λ's or K_S's.

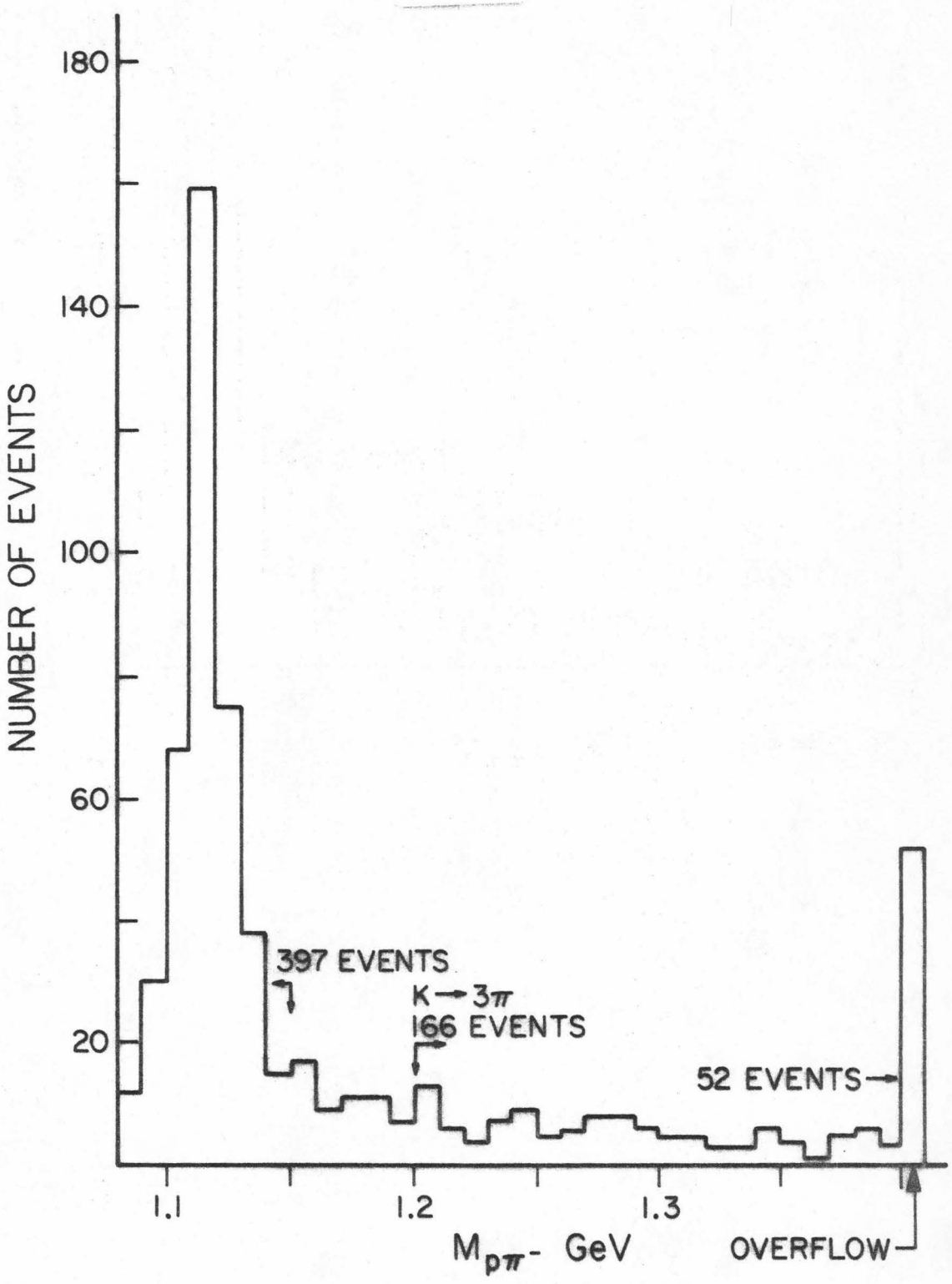

Figure 5 - Λ-mass distribution of the data events with $K \rightarrow 2\pi$ events removed.

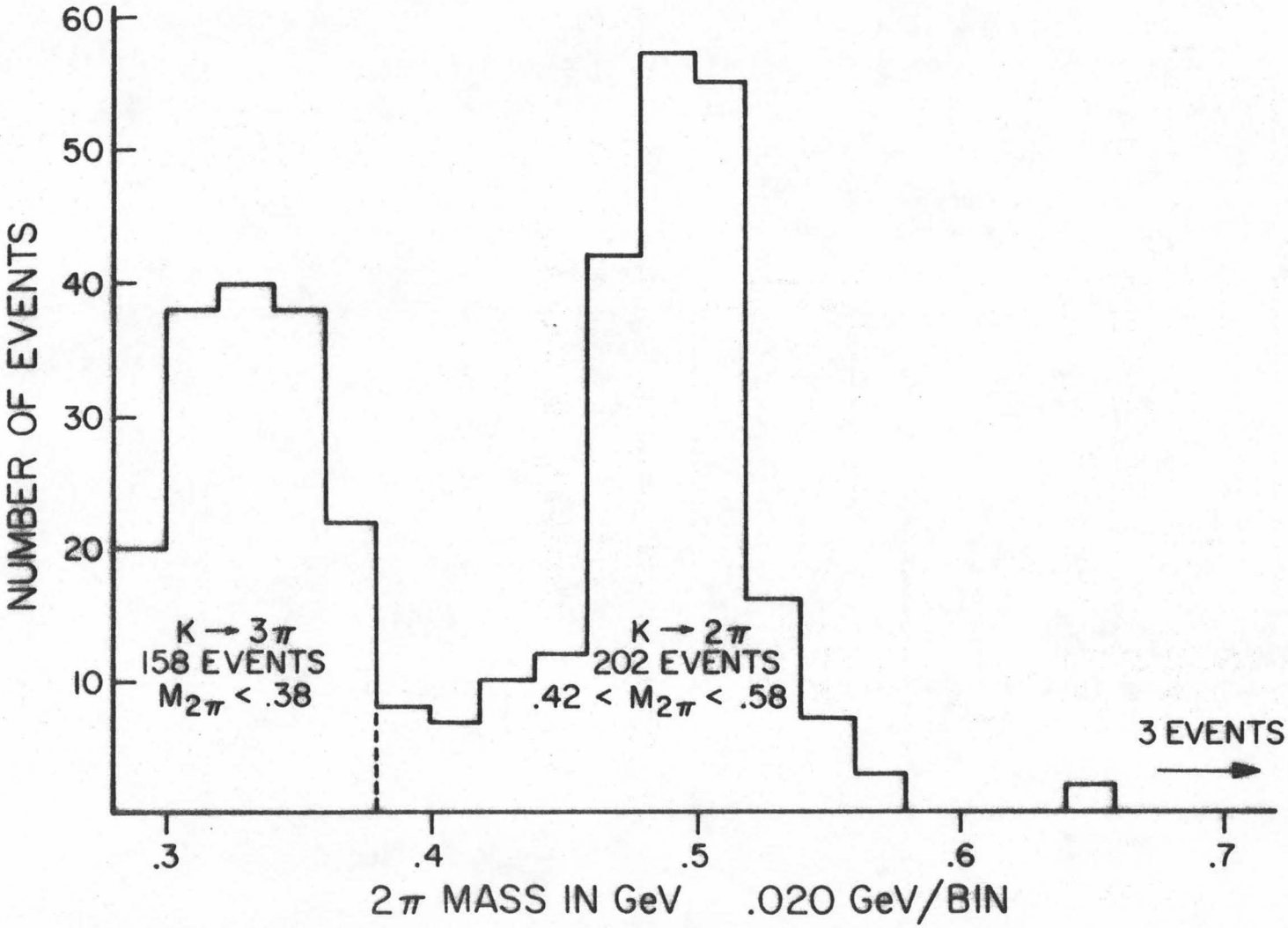

Figure 6 - 2π mass distribution of the data events with the Λ's removed.

VIII. Remnant Backgrounds

The principle technique for estimating the remnant backgrounds in the $K \rightarrow \pi^+\pi^-\pi^o$ data is to compare the mass distribution for these data (Figures 5 and 6) with similar distributions (Figures 7 and 8) for $K \rightarrow \pi^+\pi^-$ data (calibration runs). The calibration runs that were used for this purpose were analyzed in much the same way as the $K \rightarrow \pi^+\pi^-\pi^o$ data. The major difference is that there was no bias towards events with associated γ-rays in the calibration run data. The largest effect of this difference was to alter the ratio of Λ decays to K_S decays by a factor of 3. Λ decays are favored relative to K_S decays in the $K \rightarrow \pi^+\pi^-\pi^o$ data because reaction (3.4) produces more γ-rays with higher energy than reaction (3.3). Because of this ratio difference the Λ-decay background (reaction 3.4) and the K_S decay background (reaction 3.3) have to be estimated separately.

The sources of background from reactions (3.3), (3.4) and (3.5) produce events at early times. These backgrounds therefore alter the ratio of events at early times to those at late times. The value of W (ReW in particular) is sensitive to this ratio. Other sources of background are listed below.

$$\pi^o \rightarrow 2\gamma \qquad \gamma + Z_{Sp.Ch.} \rightarrow e^+ + e^- + Z_{Sp.Ch.} \tag{3.6}$$

$$N + Z_{Sp.Ch.} \rightarrow \text{STAR} + \gamma\text{'s} \tag{3.7}$$

$$\bar{K}^o \rightarrow \pi^+ \pi^- \pi^o \hookrightarrow 2\gamma \tag{3.8}$$

$$K^o \rightarrow \pi^{\pm} u^{\mp} r \qquad \Lambda \rightarrow N\pi^o \hookrightarrow 2\gamma \tag{3.9}$$

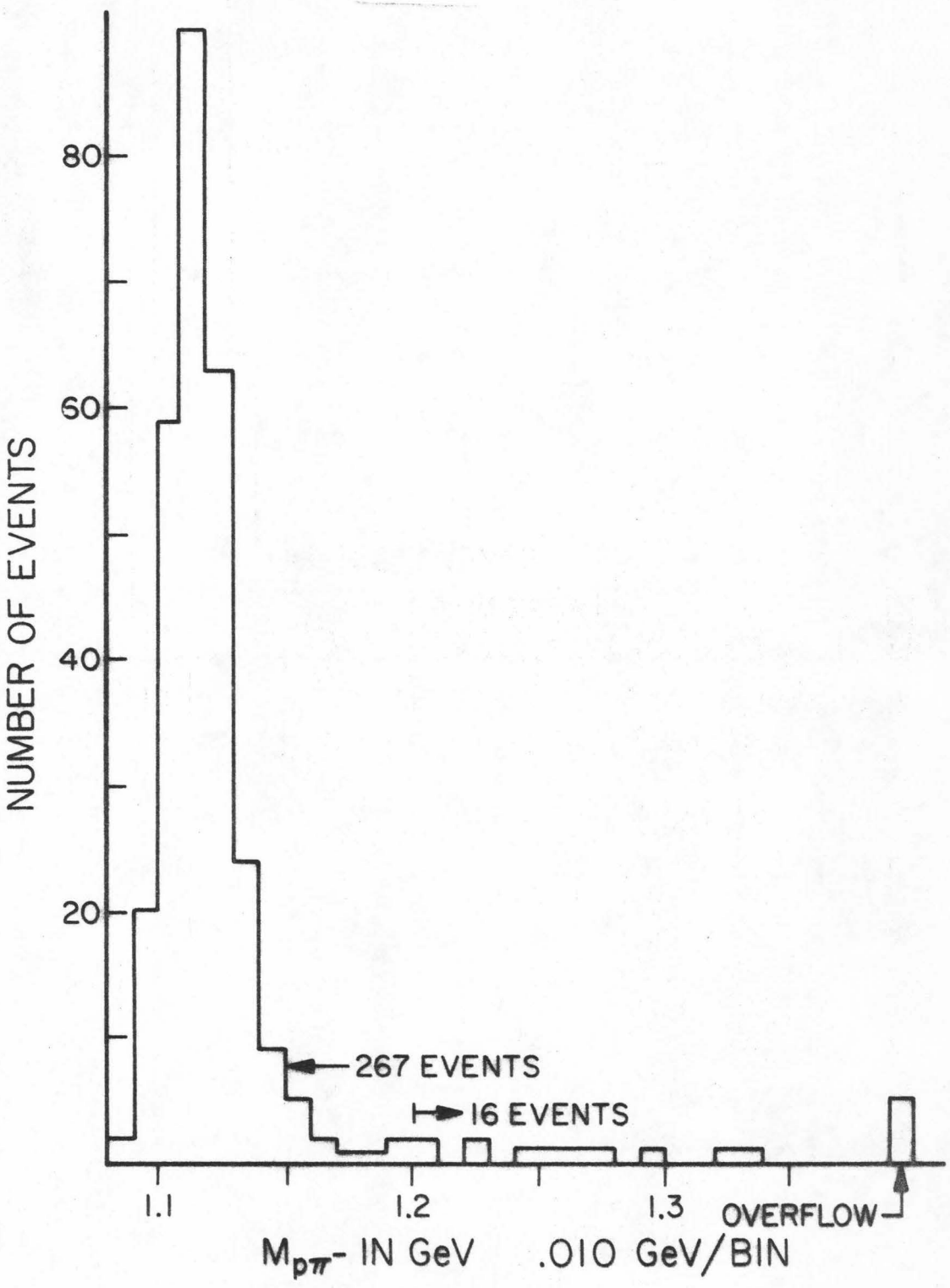

Figure 7 - Λ-mass distribution for the calibration runs with $K \rightarrow 2\pi$ events removed.

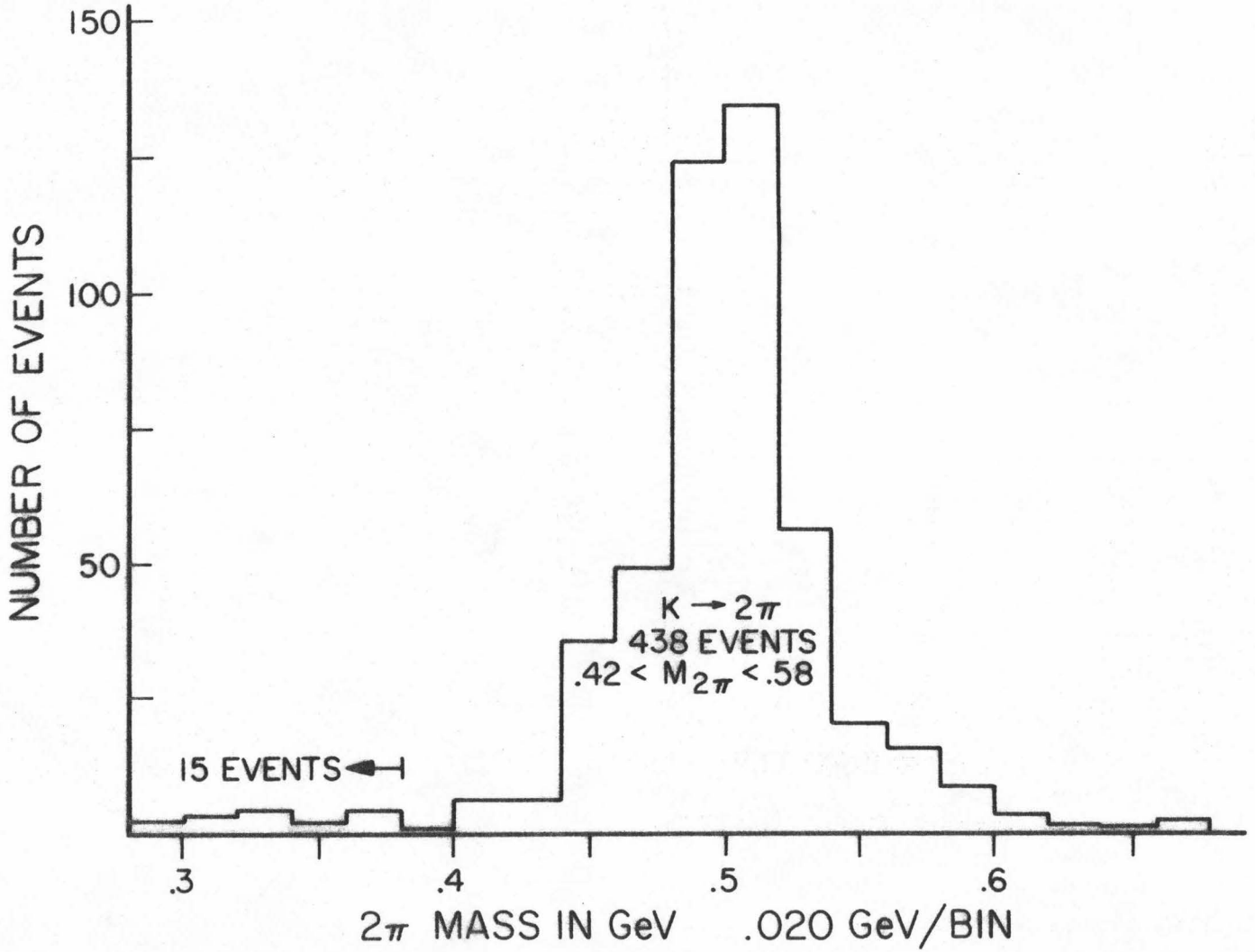

Figure 8 - 2π mass distribution for the calibration runs with Λ's removed.

These backgrounds are expected to produce events uniformly in time (space). Assuming that they have approximately the same efficiency function as the $K^o \rightarrow \pi^+\pi^-\pi^o$ events, the fit of W should be relatively unaffected by them.

The remnant backgrounds for the processes (3.3) to (3.9) are discussed below. The number in parentheses next to the section title is the best estimate of the size of the particular background in the final data sample.

Λ-tail (.2 ± 3.3 events)

Though the Λ peak is narrow, it has a broad tail which extends beyond 1.15 GeV. The distribution is smeared because the typical track must traverse 12% of a radiation length before entering the Shower Region. In order to estimate the Λ contamination above 1.15 GeV, a comparison is made in Table 6 of the Λ mass distribution (+ track has proton mass) with the $\bar{\Lambda}$ mass distribution (- track has proton mass) for the data and the calibration runs. Only events in the first half (closest to the target) of the fiducial volume are used. This retains 85% of the Λ's. Both the Λ mass and the $\bar{\Lambda}$ mass must be above 1.15 GeV. In the calibration run the 2π mass is cut below .42 GeV. This retains 80% of the Λ's. In the data the 2π mass is cut between .38 and .42 GeV. This retains 20% of the Λ's. This cut excludes $K \rightarrow \pi^+\pi^-\pi^o$ events because they would wash out any effects.

To estimate the Λ contamination in the final data sample we assume that this contamination would lie in the mass bin 1.20-1.25 GeV (everything below 1.20 GeV is removed). The excess of Λ events over $\bar{\Lambda}$ events in this mass bin (see Table 6) is (-1 ± 3.5) in the calibration runs

M_Λ mass bins in GeV		1.15-1.2	1.2-1.25	1.25-1.3	> 1.3	Cuts
Calibration runs	Λ	10	5	1	9	$M_\Lambda > 1.15$, $M_{\bar{\Lambda}} > 1.15$ GeV
267 Λ's	$\bar{\Lambda}$	2	6	5	12	$M_K < .42$GeV, $t < 3K_S$ life
$M_\Lambda < 1.15$ GeV	Λ-$\bar{\Lambda}$	8±3.5	-1±3.3	-4±2.5	-3±4.5	Total Λ efficiency is 68%
Data 360Λ	Λ	2	2	0	7	$M_\Lambda > 1.15$, $M_{\bar{\Lambda}} > 1.15$ GeV
with $M_\Lambda < 1.15$ GeV	$\bar{\Lambda}$	0	1	3	7	$.38 < M_K < .42$ GeV, $t < 3\tau_{K_S}$
	Λ-$\bar{\Lambda}$	2±1.7	+1±1.7	-3±1.7	0±4	Total Λ efficiency is 17%

Note: The Λ contamination in a mass bin is estimated by subtracting the $\bar{\Lambda}$'s from the Λ's.

TABLE 6 - The Λ Tail

and (+1 ±1.7) in the data. By taking into account all the inefficiencies in the above process and normalizing the calibration runs to the data on the basis of the sizes of the Λ peaks, we can estimate the Λ contamination in the final data sample in two ways. The calibration run Λ tail gives an estimate of (-1.2 ± 4). The Λ tail for the data with $.38 \leq M_{\pi^+\pi^-} \leq .42$ GeV produces an estimate of (3.5 ± 6). If instead of assuming that this contamination is only in the bin $1.20 < M_\Lambda < 1.25$ GeV we assume that it is in the bin $1.20 < M_\Lambda < 1.3$ GeV then these numbers become (-6 ± 5) and (-7 ± 9) respectively. Applying this same technique to the bin $1.15 < M_\Lambda < 1.20$ GeV we find that a mass cut $M_\Lambda < 1.15$ GeV would have left (10 ± 4) Λ events in the data sample by the calibration run estimate and (7 ± 6) events by the data sample estimate. For the purposes of this experiment we will use the weighted average of the estimates obtained from the data and calibration run Λ tails with the assumption that the contamination lies in the bin $1.20 < M_\Lambda < 1.25$ GeV. That is, the number of Λ events in the final data sample is (.2 ± 3.3) events.

K_L Decays (2 ± 1.5) and the $K_S \rightarrow 2\pi$ Tail (4.5 ± 2)

In the calibration run there are 16 events with $M_{2\pi} < .38$ (see Figure 8). The previous section put an upper limit of 2.3 Λ's in this sample. An examination of the Production-Decay Region found only 1 out of 16 events which did not meet the data scanning criteria (there was a 10° bend in one arm of the vee). Therefore, the background in this region of the calibration run is probably very representative of that in the $K \rightarrow 3\pi$ region of the data. There are two differences, however. First, the number of $K \rightarrow 2\pi$ in the calibration run is twice as great as in the

data, so the background estimate must be normalized by a factor of 2. Second, because of the gamma ray enhancement in the data, we would expect to find $K_S \rightarrow \pi^+\pi^-\gamma$ events in this mass region and above.

If we examine the vertex distribution of these 15 events that meet the $K \rightarrow \pi^+\pi^-\pi^o$ criteria, we find 3 events in the last half of the chamber. This leads to an estimate of 5 ± 3 events caused by K_L decays (these would be from $K_L \rightarrow \pi^\pm u^\mp \nu$ and $K_L \rightarrow \pi^+\pi^-\pi^o$) which is reasonable for 430 $K_S \rightarrow 2\pi$ events, and the estimate 10 ± 3 caused by K_S decays (these would be tail events from $K_S \rightarrow \pi^+\pi^-$). The K_L decays are not as serious a background for this experiment because the time distribution of these events will be fairly flat. Normalizing this to the data $\frac{190 \text{ Data } K\rightarrow 2\pi}{430 \text{ C.R. } K\rightarrow 2\pi}$ we get an estimate of (2 ± 1.5) K_L decays (reaction 3.9) and (4.5 ± 2) K_S decays (reaction 3.3) in the $K \rightarrow 3\pi$ mass region.

<u>$K \rightarrow \pi^+\pi^-\gamma$ (3 ± 2)</u>

Next we examine the region of the 2π mass between .38 and .42 GeV. Again in order to remove K_L decays we subtract 75% of the events with vertices in the last half of the Production-Decay Region from those in the first half. (Only 5% of the K_S decays occur beyond the halfway point and the relative efficiency for K_L decays is approximately 75% in this 2π mass region.) This gives 3.5 ± 2.5 events in this region in the calibration run and 8 ± 4 events in the data. Subtracting the weighted calibration run $(\frac{190}{430})$ from the data events we get an excess of 6.5 ± 4 events in the data as compared with the calibration run.

Assuming that this excess is caused by $K \rightarrow \pi^+\pi^-\gamma$ and assuming that the acceptance of the apparatus is roughly the same (for this type of event) in the region $.35 < M_{2\pi} < .38$ GeV as for $.38 < M_{2\pi} < .42$ GeV, then this excess leads to an estimate of 3 ± 2 $K_S \rightarrow \pi^+\pi^-\gamma$ events in the region $M_{2\pi} < .38$ GeV.

$\bar{K}^o$ Production (1.5%)

The presence of $\bar{K}^o$'s at $t = 0$ in the data would tend to wash out an interference term in this experiment. To wash it out completely would require that the number of $\bar{K}^o$'s equal the number of K^o's so a small number of $\bar{K}^o$'s is not a problem.

The production reaction for $\bar{K}^o$'s, from a 3 GeV π^- beam is reaction (2.3). From reference (11) this reaction on hydrogen has 1/10 the cross-section of the production reactions (2.1) and (2.2). The acceptance for events from reaction (2.3) was calculated to be down by at least another factor of 10 due to the wide angular distribution and the relatively low momentum of the $\bar{K}^o$'s and the K^o's from this reaction. Therefore (2.3) could be expected to contribute less than 1% to the data.

The production cross-section of the reaction

$$K^- + p \rightarrow N + \bar{K}^o \qquad (3.10)$$

is 5 times greater than for (2.1). However, the K^- contamination in the π^- beam was found to be only .1% by a careful study of the pulse height distribution in a beam gas counter and time of flight measurements. Therefore this source of $\bar{K}^o$'s would contribute only 1/2% to the data.

The combined result from reactions (2.3) and (3.10) is 1.5% $\overline{K}^o$ contamination. This is in good agreement with a fit made with the Ke3 data* which gave a result of ($0.6\% \pm \frac{1.9}{0.6}\%$) for the K^o to $\overline{K}^o$ ratio.

Neutron Stars (4 ± 2 events)

These events are produced (reaction 3.7) when neutrons, produced in the target, interact with the aluminum in the spark chamber plates of the Production-Decay Region. In the final data sample there were only two stars with three or more prongs (secondaries). Assuming that the number of stars with two prongs is comparable to the number with more than two prongs we get (4 ± 2) stars in the final data sample. These have a uniform spatial distribution.

Electron Pairs and Pion Electron Events (< 3)

The conversion of γ-rays in the aluminum plates of the Production-Decay Region (reaction 3.6) could have been a serious source of background in this experiment. However, there were two means by which this was reduced. First the gas counter in the center of the mass spectrometer rejected electrons with 97% efficiency. Backing this up were the lead plate Shower Chambers. Here electrons can be distinguished from pions with 97% reliability.

Events with electrons in them were not strongly reduced (75% reduction) during the initial Shower Scan. During the Shower Rescan (done by a physicist) 30 $e^+e^-\gamma$ events and 5$\pi^{\pm}e^{\mp}\gamma$ events were found in the shower chambers with masses in the final data sample region. Given

---

*Ph.D. Thesis, John Gallivan, C.I.T. (1970), p.69.

a 30 to 1 rejection of electrons, there should be no ee events ($\frac{1}{30} \times \frac{1}{30} = \frac{1}{900}$) and 1/6 of a πe event after the Shower Rescan. In the final data sample events with a gas counter pulse greater than one were removed. This reduces the electron background by another factor of 30.

Looking at the e^+e^- mass distribution there are only 3 events in the region where e-pairs are found. Therefore an upper limit of 3 e-pair events is conservative. In any case these events are flat in the spatial distribution and would not produce a serious bias.

IX. Background Summary

Adding up the results of the previous analysis it is expected that there are ($8 \pm \frac{4.5}{3.0}$) background events that have a flat spatial distribution and (8 ± 5) events which are related to Λ decays or K_S decays, thus having an exponential distribution (which more closely resembles an interference term). When the data is fit to a flat distribution plus an exponential term, the one standard deviation point in the likelihood function occurs at a value corresponding to 9 exponential events. This agrees well with the above estimate of Λ and K_S decay backgrounds.

CHAPTER IV - EFFICIENCY CALCULATION AND MAXIMUM LIKELIHOOD FIT

Measuring the time distribution of $K^o \rightarrow \pi^+\pi^-\pi^o$ decays requires a knowledge of the proper time of each event and the probability that the event has of being accepted. The proper time for each event was determined from the decay length (the distance from the production point to the decay point) and the mean inverse momentum of the accepted events. The mean inverse momentum of the accepted events was determined by the Monte Carlo calculation discussed below. The smearing effect of the width of the momentum distribution on the time distribution of the decays is discussed in Appendix X . There it is determined that this smearing effect changes the time distribution by less than 2%. The kinematic reconstruction of the individual events, to determine the proper time, was therefore unnecessary.

The probability that an event would be accepted by the apparatus and the data reduction procedure was determined with the aid of a Monte Carlo calculation. This acceptance was determined as a function of the decay length only and was averaged over all other relevant parameters. This Monte Carlo calculation required the momentum and angular distributions of K^o's as inputs. These distributions were determined by analyzing calibration runs in which the apparatus trigger and the data reduction process were designed to isolate $K_S \rightarrow 2\pi$ events. With these events the kinematics could be completely reconstructed.

The calibration run events were combined with a Monte Carlo calculated acceptance function ($\epsilon_{K2\pi}(p_K, \theta_K)$) to produce the K^o momentum

and angular distributions. Because the angles involved are small ($< 15^{o}$) these two distributions were taken to be independent of each other. The momentum distribution (f(p)) was fit to the following empirically chosen function:

$$f(p) = e^{-1/2(\frac{p-A}{B})^2} \cdot R(p;C,D); \quad 4 \text{ parameters} \quad ,$$

where R(p;C,D) is a function designed to cut off the spectrum at the high momentum end, and

$$R = 1; \quad p < C$$

$$R = (D-p)/(D-C); \quad C \leq p \leq D$$

$$R = 0; \quad p > D \quad .$$

The angular distribution ($g(\theta)$) was fit at the same time to:

$$g(\theta) = \theta \cdot e^{-1/2(\frac{\theta-S}{T})^2}; \quad 2 \text{ parameters} \quad .$$

A Gaussian momentum resolution function was included in this fit to account for the measurement error in the momentum, as

$$S(p-p') = e^{-1/2\frac{(p-p')^2}{\sigma^2}}$$

where σ = .16 GeV/C for T1 events and σ = .30 GeV/C for T2 events when the K^{o} momentum is 2.4 GeV. The combination of these distributions,

$$\zeta(p_K,\theta_K) = \int dp' S(p_K-p') \; f\,(p') \; g(\theta_K) \; \epsilon_{K2\pi}(p',\theta_K) \quad ,$$

was then fit to the calibration run data ($K \rightarrow \pi^{+}\pi^{-}$). The best fit to the six parameters gave the following values:

$$A = 2.48 \; {}^{+\,.03}_{-\,.08} \qquad D = 2.86 \; {}^{+\,.01}_{-\,.00}$$

$$B = .82 \; {}^{+\,.13}_{-\,.03} \qquad S = -1.0 \; {}^{+\,.9}_{-1.4}$$

$$C = 2.68 \; {}^{+\,.04}_{-\,.07} \qquad T = 9.0 \; \pm .6 \quad .$$

Sketches of the resulting f(p) and g(θ) distributions are given in Figure 9.

As a check on the above procedure for determining f(p) and g(θ) a Monte Carlo calculation was made using these distributions as inputs. The resulting momentum and angular distributions of the Monte Carlo accepted events are compared directly with the calibration run data in Figure 10. The vertex positions (distance from the target) of the Monte Carlo events and the data events are compared in Figure 11. For both T1 and T2 these distributions compare quite well.

$K \rightarrow 3\pi$ Efficiency

The momentum and angular distributions of the K^o's (f(p) and g(θ)), which were determined in the above procedure, were then used as inputs to a Monte Carlo calculation of the $K \rightarrow 3\pi$ acceptance ($\epsilon_{K3\pi}(\ell)$) as a function of the decay position (L). Four values of L were chosen (10" apart) at which decays were generated. After suitable cuts were made in the sample of successful Monte Carlo events the acceptance at these points was fitted to a straight line. This fit is shown in Figure 12 for the two values of the magnetic field setting in which the pions were constrained to be on opposite sides of the shower chambers and at the one field setting where they were constrained to be on the same side of the shower chambers.

The Monte Carlo events were initially generated with a uniform distribution on the Dalitz plot and no γ-ray energy bias. Both the charged and neutral secondaries were run through a program which was essentially the same as the one used in the $K \rightarrow 2\pi$ Monte Carlo calculation. (However, provision had to be made for tracing the γ-rays

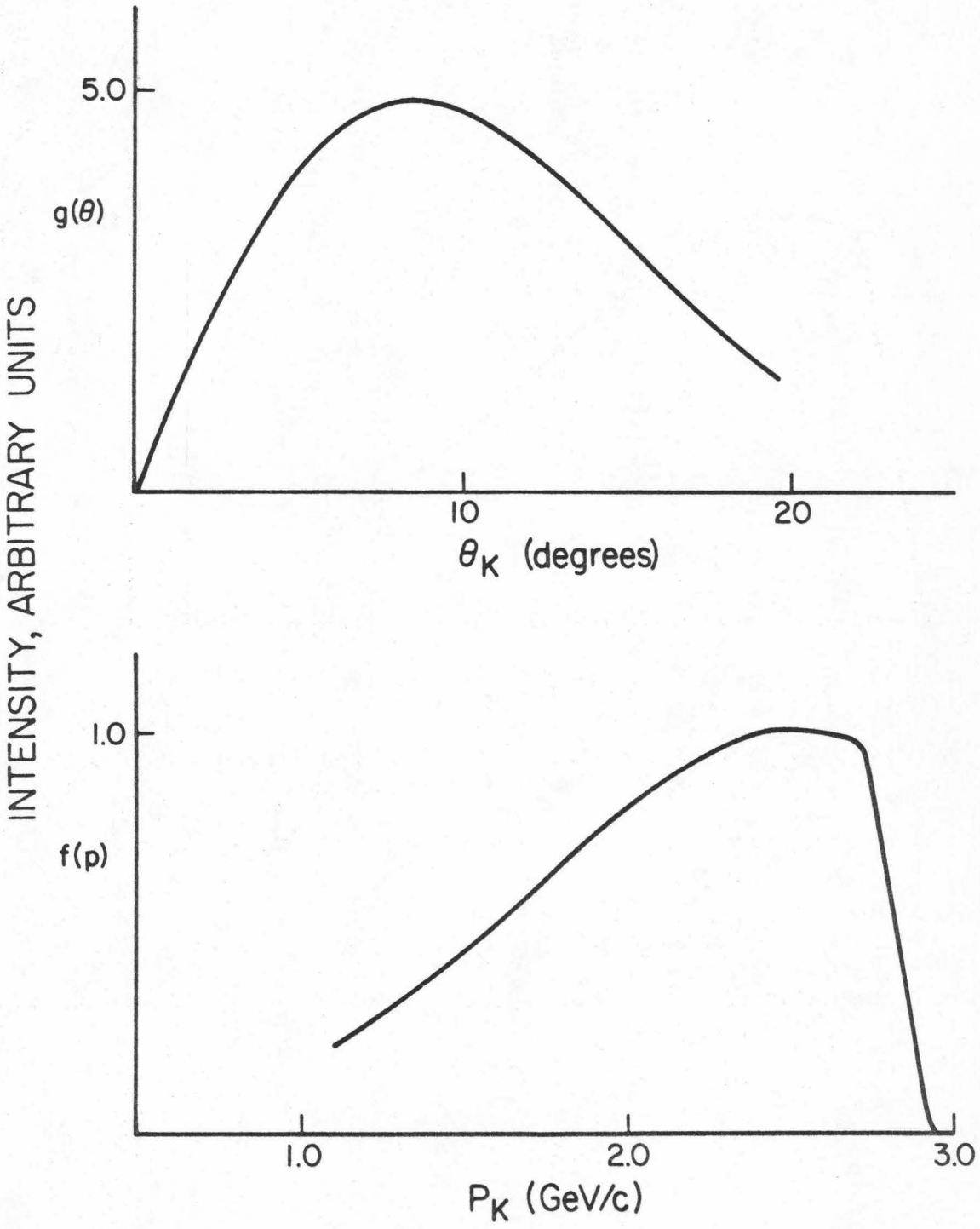

Figure 9 - Angular and momentum distribution of K^0's from brass with 2.85 GeV/c incident negative pions.

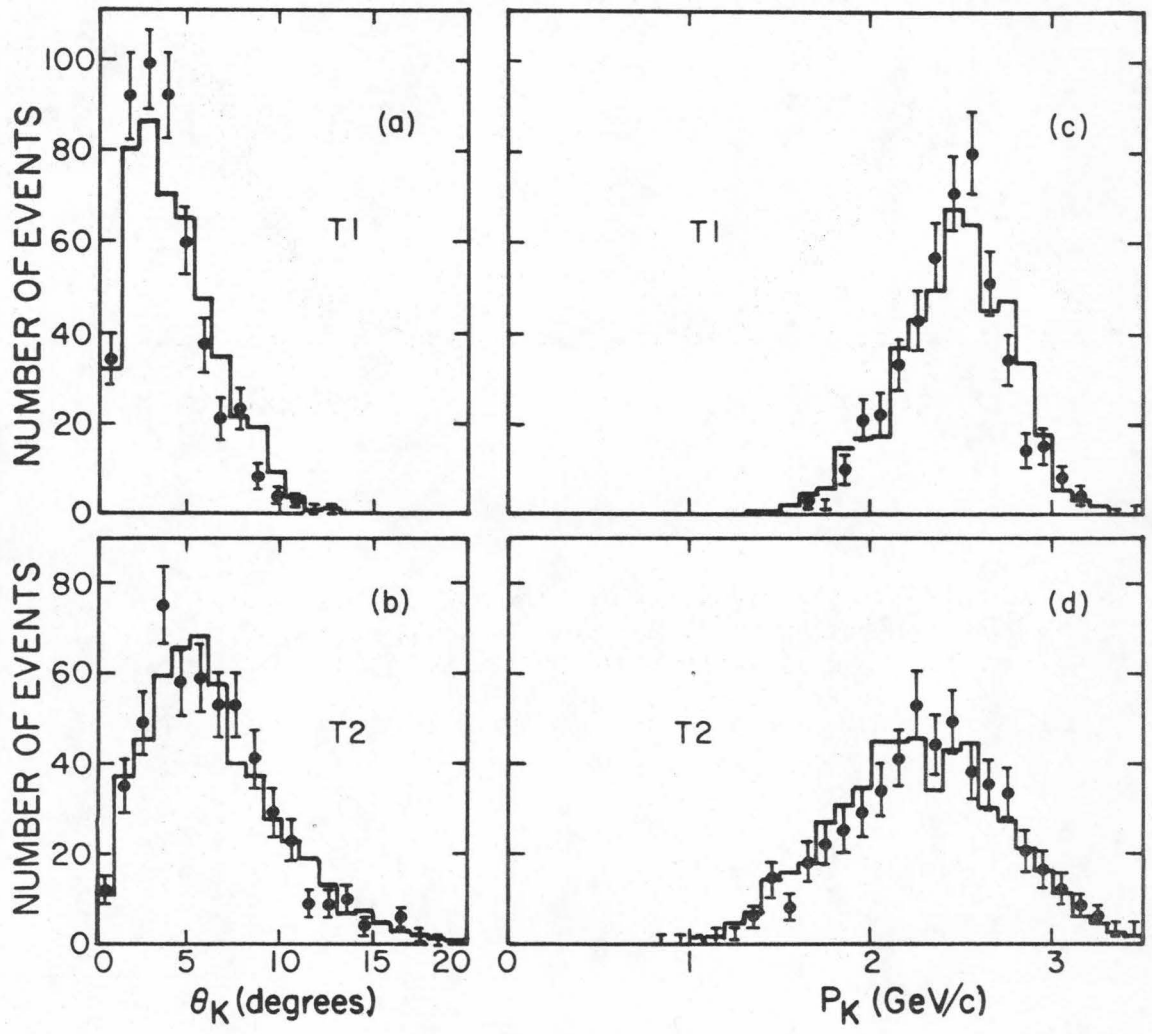

Figure 10 - Comparison of Monte Carlo (histograms) events to calibration run events (data points) for K^o angular distribution ((a) and (b)) and K^o momentum distributions ((c) and (d)).

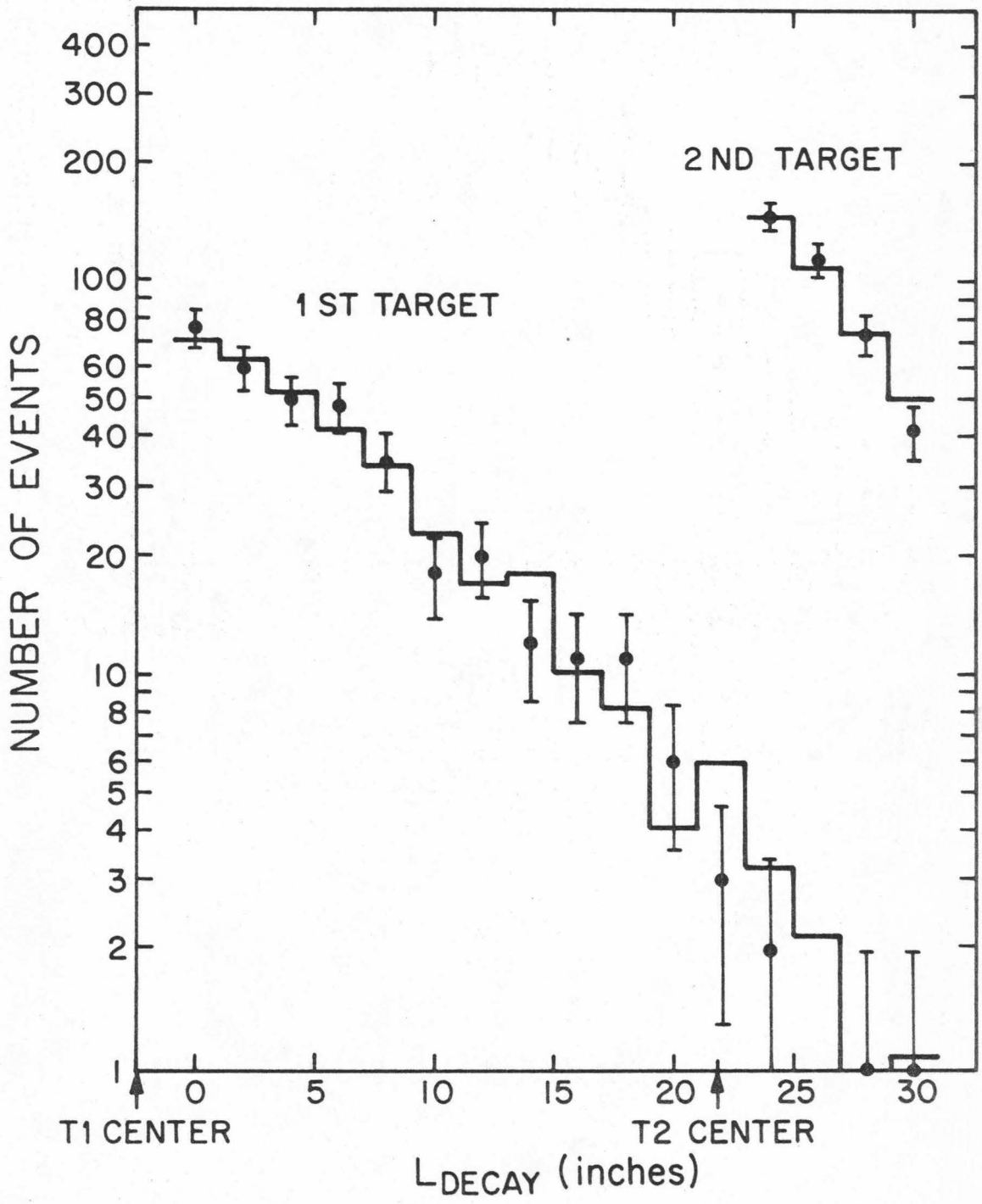

Figure 11 - Comparison of Monte Carlo (histograms) event position distributions with those for calibration run events (data points).

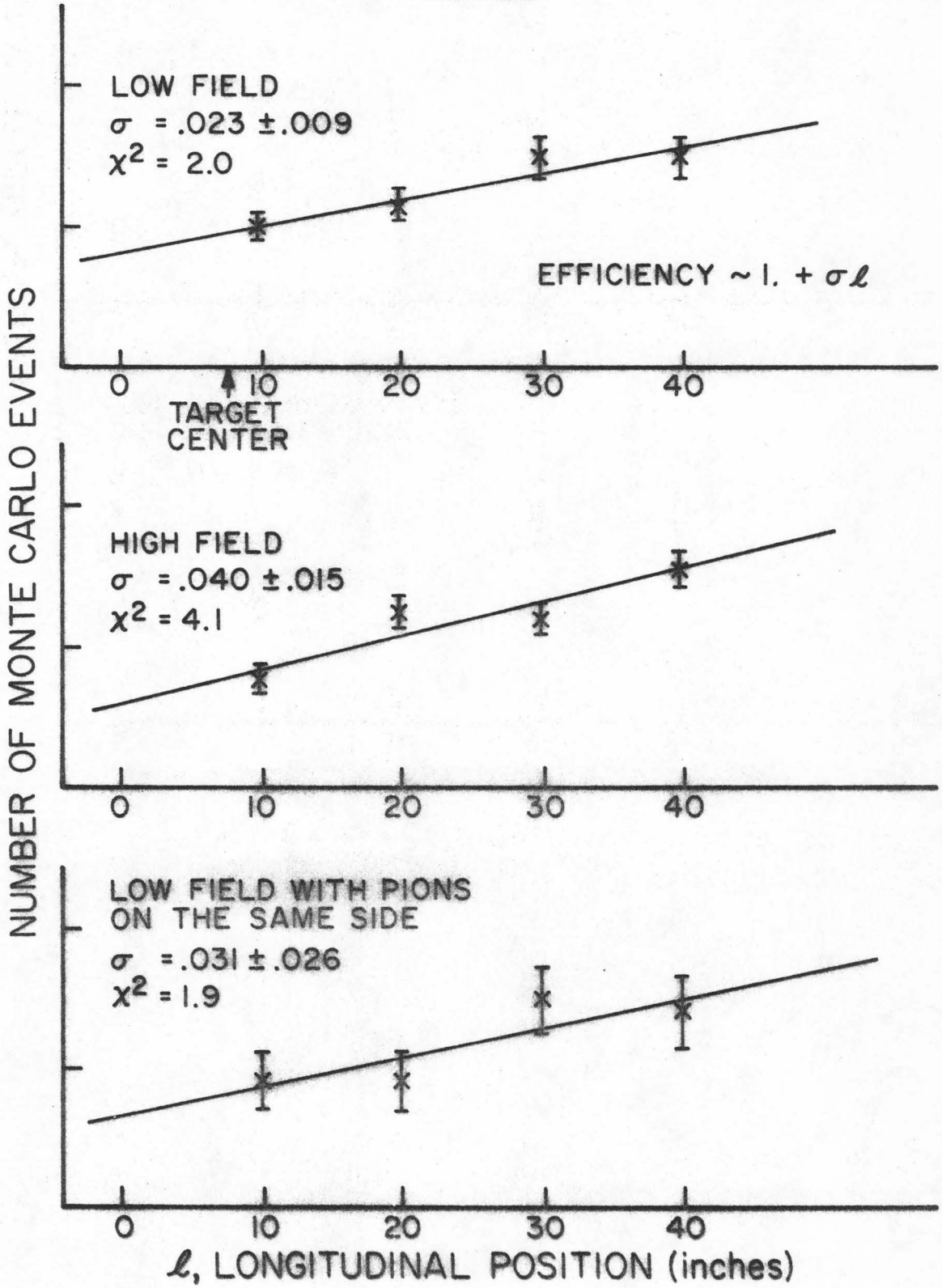

Figure 12 - $K \rightarrow 3\pi$ Monte Carlo efficiency as a function of decay position (ℓ).

through the apparatus.) The events that were successful were then weighted to take into account:

(1) The $M^2_{\pi^+\pi^-}$ dependence in the Dalitz plot.

(2) The energy bias imposed on the γ-rays by the shower counter triggering scheme.

(3) The computer scan of the data.

(4) The Λ mass cut on the data.

The dependence of the $K \rightarrow \pi^+\pi^-\pi^o$ transition rate on the kinetic energy of the π^o in the center of mass is given by the following formula:

$$|F|^2 \sim 1 + \frac{2 \cdot S \cdot M_K}{M_\pi^2} (2T_{\pi o} - T_{max}) \qquad (4.1)$$

$T_{\pi o}$ = π^o kinetic energy in C.M.

T_{max} = .053 GeV = maximum value of $T_{\pi o}$

S = Dalitz plot slope.

From the latest experiments on $K_L \rightarrow \pi^+\pi^-\pi^o$[12] we have taken S = -.30. When the data in this experiment is analyzed for the Dalitz plot slope (see Figure 13) we get S = -.28 $\pm$ .05. The slope of the efficiency function (σ in Figure 12) was not very dependent on S. Between S = 0 and S = S_{min} = -.35, σ changes by .015.

The next most important effect on the data is the dependence of the shower counter acceptance on the energy of the γ-ray that triggered the apparatus. The apparatus trigger was set to fire on a pulse of greater than 3 times minimum ionizing on either side of the Shower Hodoscope (dividing it down the center). Assuming that the pion which passes through the same side as the γ-ray leaves a minimum ionizing pulse, then the γ-ray must leave a 2 times minimum ionizing pulse to

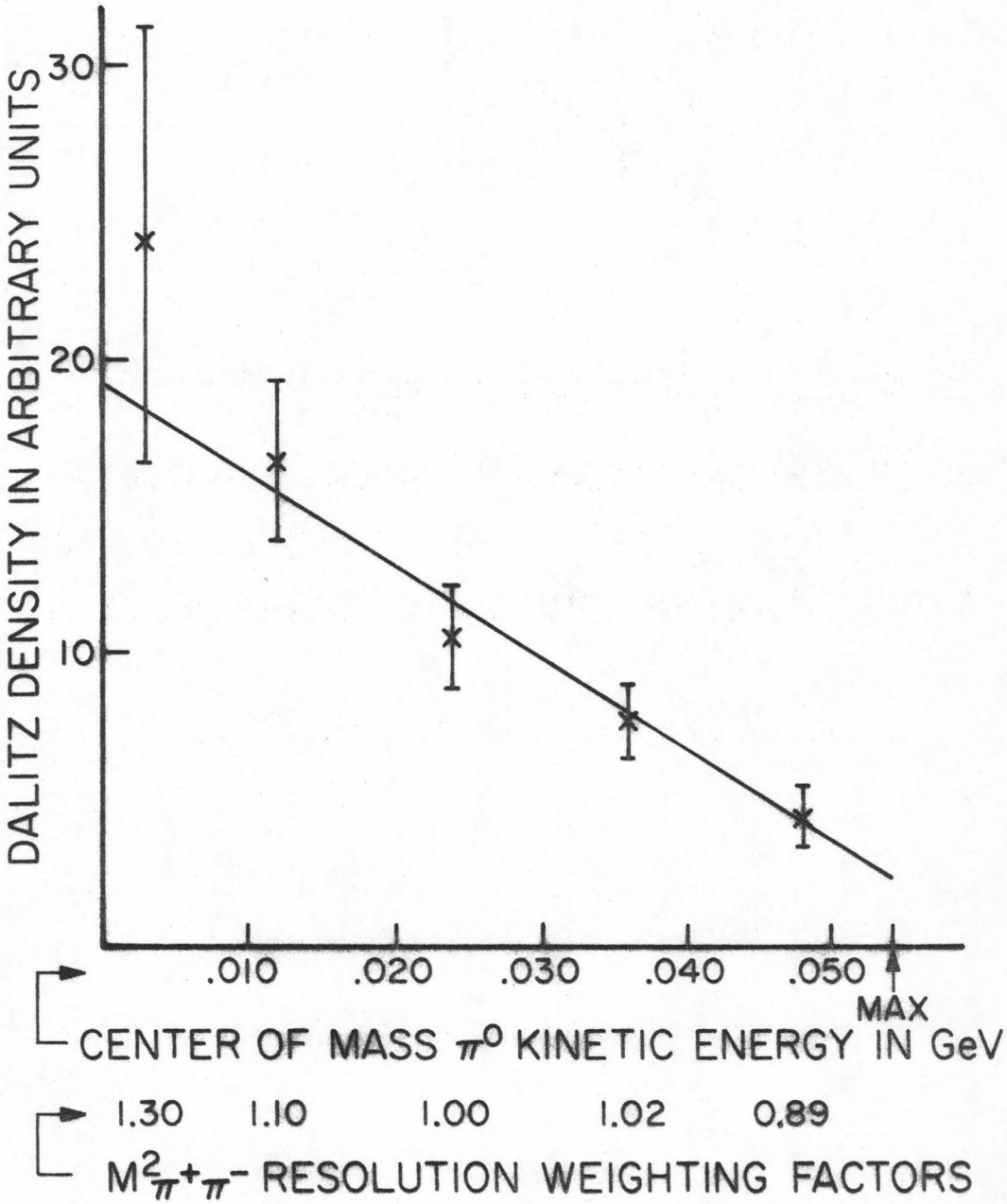

Figure 13 - Dalitz plot density of the $K \rightarrow 3\pi$ data.

trigger the apparatus. The pulse heights for accepted gamma rays and calibration run pions are distributed in Figure 14.

The γ-ray shower is sampled at 3 and 5 radiation lengths. Figure 15 contains the calculated acceptance of the shower counters as a function of energy when the sum of the pulses at these 2 depths is required to be greater than 2 times the minimum ionizing* (twice what a pion would produce). Figure 16 contains the measured acceptance for electrons when the pulse height requirement was 1.7 minimum ionizing. The two graphs are very close in their general features. The acceptance shown in Figure 15 was used to weight the Monte Carlo events.**

The effect of the computer scan was imposed on the Monte Carlo events by requiring that the γ-ray not go through the shower counters that would be reserved (in the computer scan) for the pions. This is a small geometric effect.

The Λ-mass cut was made on the Monte Carlo events in the same way as on the data. The Λ-mass was constructed by assigning the proton mass to one of the pions and calculating the invariant mass. Events with a mass less than 1.2 GeV were then removed.

The above effects were taken into account in order to make the Monte Carlo event sample correspond as closely as possible to the data events. Of primary concern was the effect of these cuts on the

---

* This calculation was made using the results of Heusch and Prescott, reference 13.

**This graph was made with the data from the Ke3 electrons, JDG Thesis, p.150.

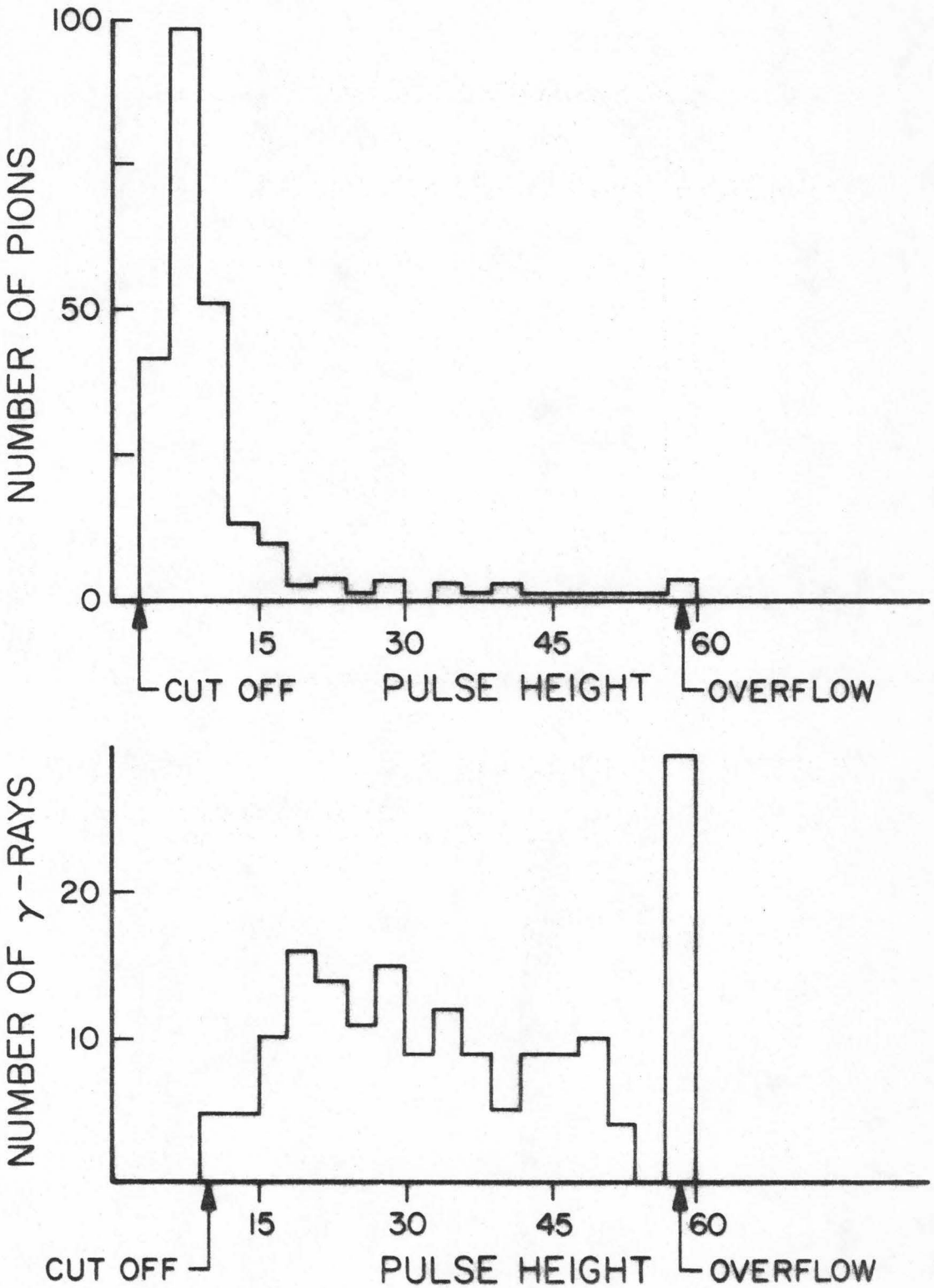

Figure 14 - Shower counter pulse height distributions for pions (calibration run data) and accepted γ-rays ($K \rightarrow 3\pi$ data).

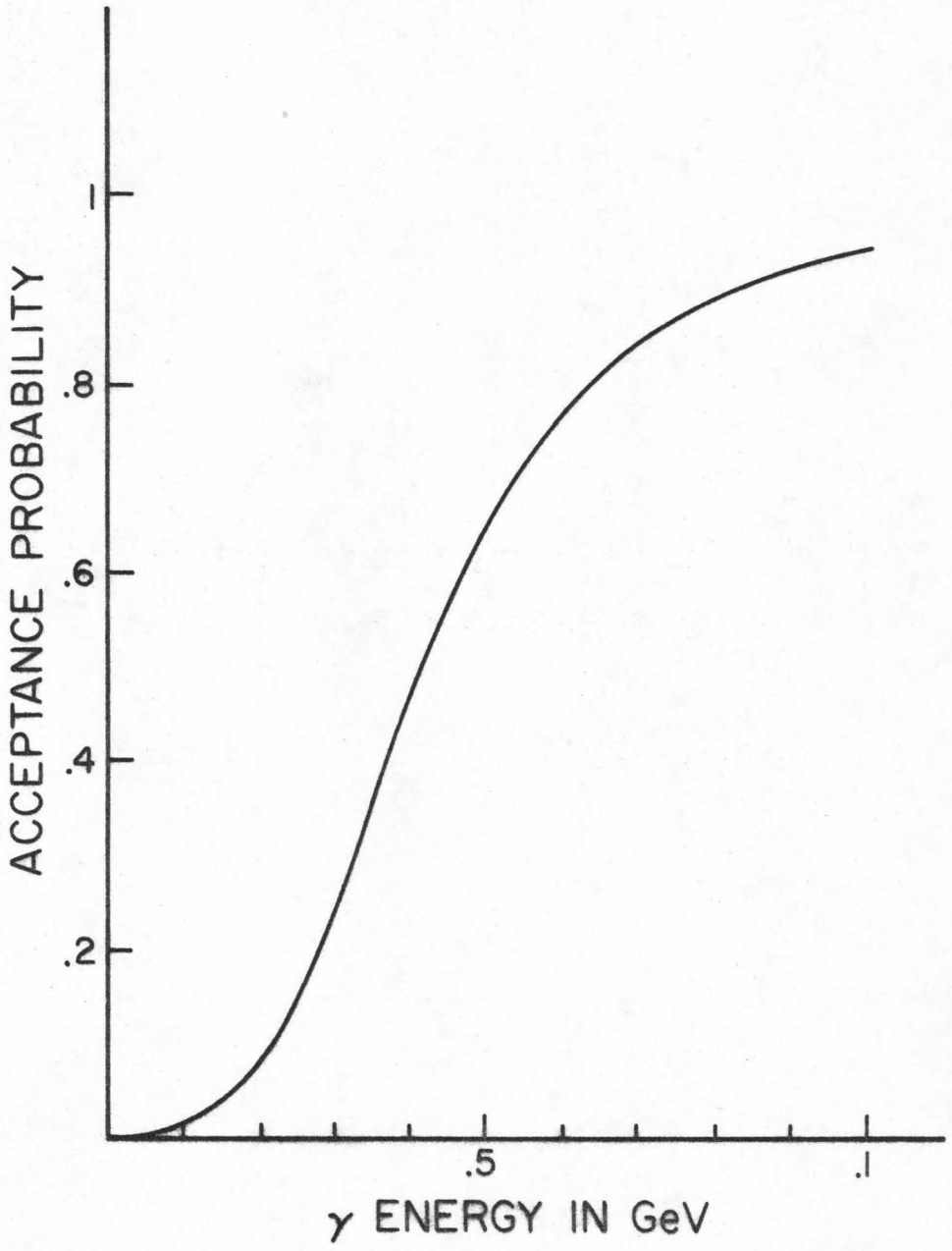

Figure 15 - Calculated γ-ray shower counter acceptance with a 2-times minimum ionizing pulse height requirement.

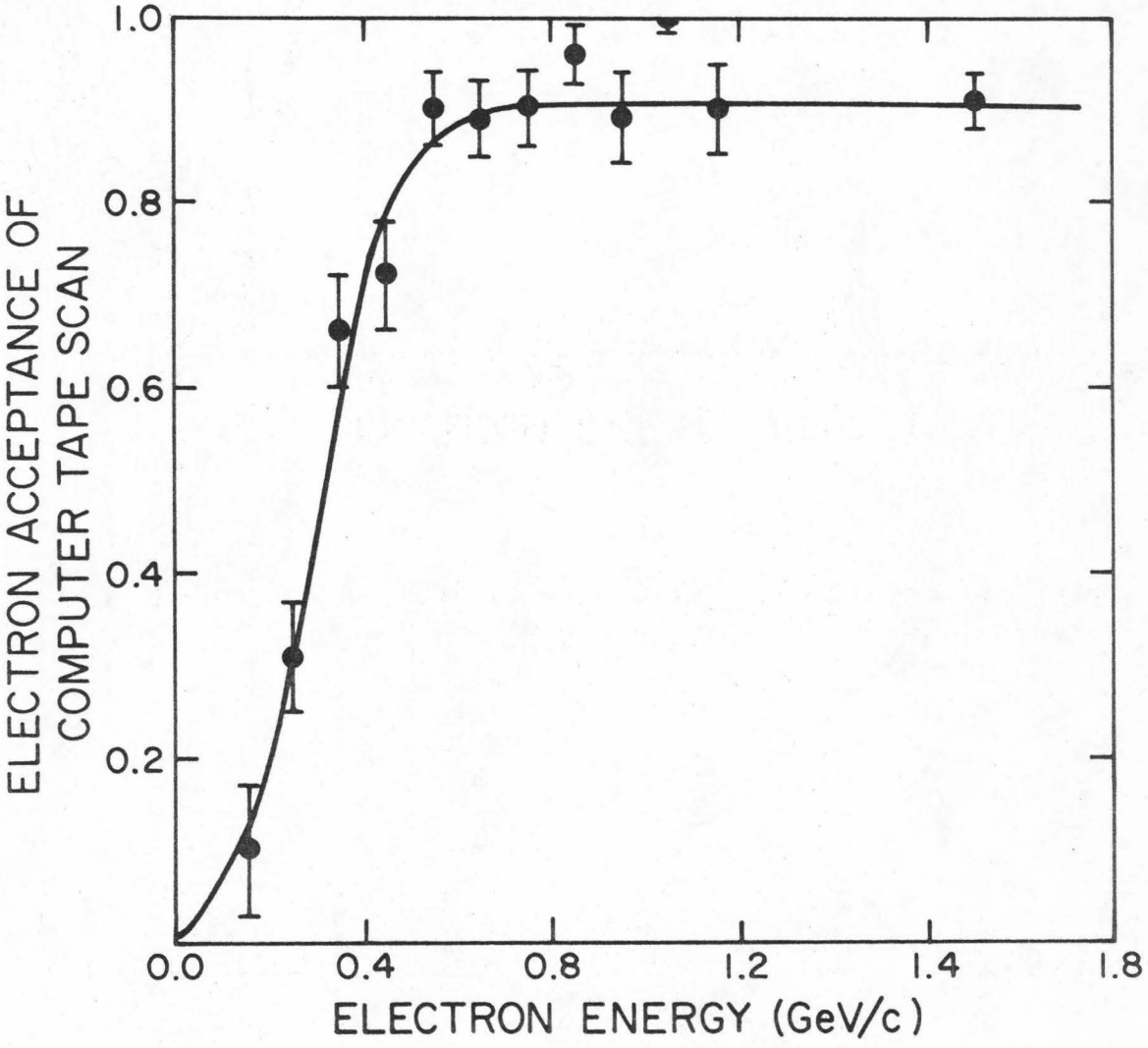

Figure 16 - Measured electron shower counter acceptance with a 1.7-times minimum ionizing pulse height requirement.

slope of the efficiency function as a function of the decay position. Table 7 contains this slope for various configurations of these cuts. When the fit of the time distribution of the data is discussed later in this chapter it is shown that a variation in the slope of $\pm.02$ does not produce a sizable variation (1/3 standard deviation) in the fitted parameters of the time distribution.

In order to check the Monte Carlo calculation, various distributions were made and compared with the data. Appendix XI contains the distribution of the track positions at the various apertures. Here the agreement between the data and the Monte Carlo calculation is good. Figures 17 and 18 contain the comparison for the individual pion momentum and the sum of the momentum of the two charged pions. The agreement is good thus providing an additional check that the K^o momentum distribution used in the Monte Carlo calculation is correct.

Figure 19 contains the comparison distributions of the opening angle between the two charged secondaries. The agreement between the data and the Monte Carlo events is good. The chi-square is 6.9 for 7 degrees of freedom. The slight excess of events at large opening angles could reflect the presence of backgrounds ($\Lambda \rightarrow p\pi^-$, $K_S \rightarrow \pi^+\pi^-$ and $K_S \rightarrow \pi^+\pi^-\gamma$ have larger opening angles than $K \rightarrow \pi^+\pi^-\pi^o$).

Figure 20 compares the $M^2_{\pi^+\pi^-}$ invariant mass distributions for the data and the Monte Carlo events. The Monte Carlo distribution includes the effect of the momentum resolution of the apparatus. The resolution function that was used for this purpose was a Gaussian distribution. The width (full) of this function varied linearly with $M^2_{\pi^+\pi^-}$.

Definitions:

Efficiency $\sim 1 + \sigma \cdot L$

σ = slope/intercept of the efficiency function.
L = the decay position ($9.5" < L < 41.0"$, $L_{TARG} = 8.0"$).
S = Dalitz plot slope (see equation 4.1).
E_γ = γ-ray energy.
M_Λ = Proton-pion invariant mass of the charged secondaries.
θ_{op} = Laboratory frame opening angle.

VARY - M_Λ:

M_Λ cut in GeV	$M_\Lambda > 0$	$M_\Lambda < 1.15$	$M_\Lambda > 1.15$	$M_\Lambda > 1.2$	$M_\Lambda > 1.3$
σ	$.029 \pm .005$	$.002 \pm .005$	$.040 \pm .008$	$.036 \pm .008$	$.024 \pm .007$
Number of Monte Carlo events	2458	330	2028	1670	1044
Fixed Cuts:	$S = -.2$, $E_\gamma > 0$				

VARY - S

S	0.	-.2	-.35
σ	$.032 \pm .007$	$.044 \pm .012$	$.044 \pm .015$
Number of Events	1913	1065	798
Fixed Cuts:	$M_\Lambda > 1.2$ GeV , E_γ weighted ($E_\gamma > .4$GeV approximately)		

VARY - E_γ

E_γ in GeV	$E_\gamma > 0.$	$E_\gamma > .5$
σ	$.036 \pm .008$	$.044 \pm .011$
Number of Events	1670	1143
Fixed Cuts:	$M_\Lambda > 1.2$ GeV, $S = -.2$	

VARY - θ_{op}

Cos (θ_{op})	$> 0.$	$> .95$	$> .99$
σ	$.036 \pm .008$	$.035 \pm .008$	$.002 \pm .005$
Number of Events	1670	1604	473
Fixed Cuts:	$M_\Lambda > 1.2$ GeV, $E_\gamma > 0.$, $S = -.2$		

TABLE 7 - Efficiency Dependences

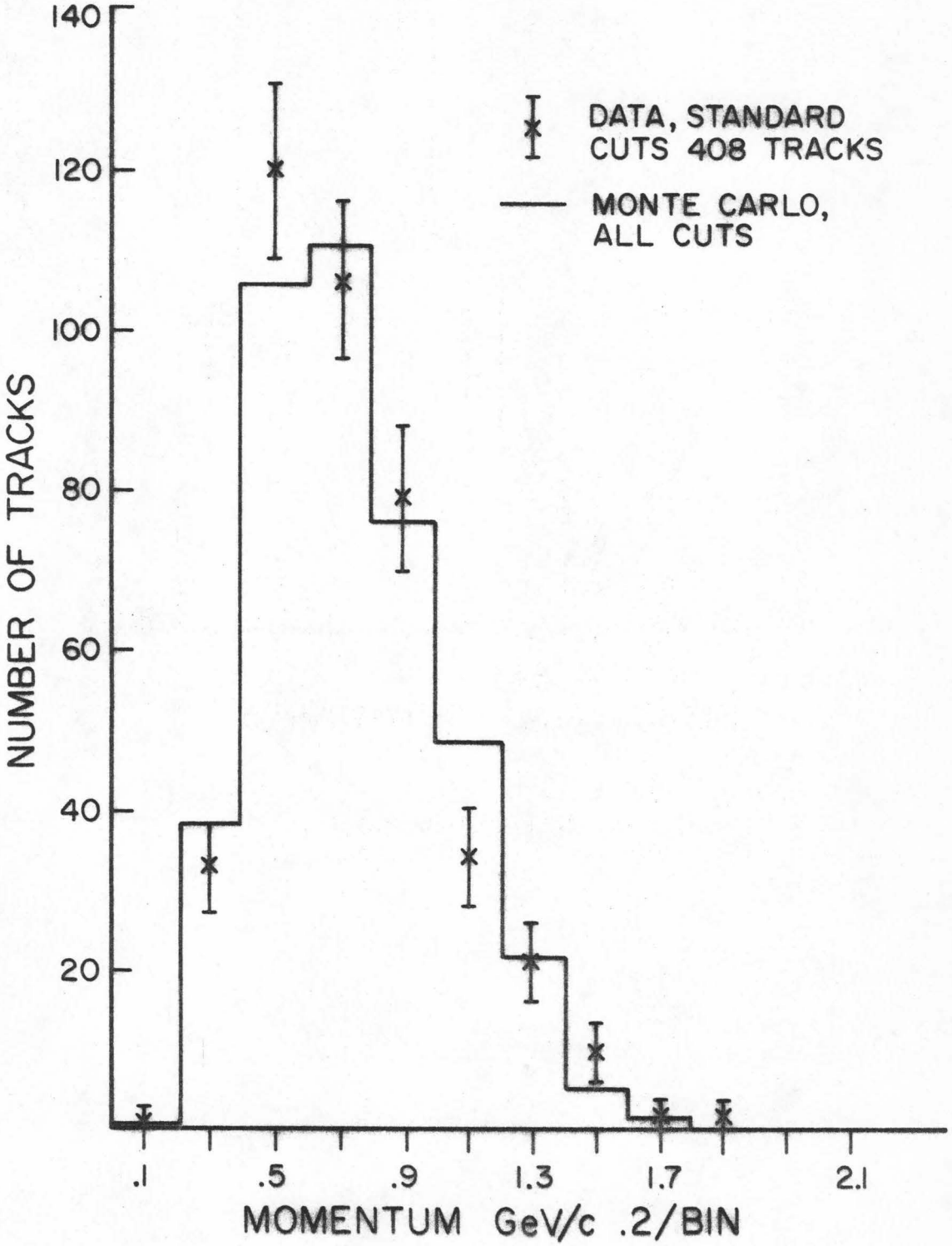

Figure 17 - Data to Monte Carlo comparison of the charged pion momentum distributions ($K \rightarrow 3\pi$ data).

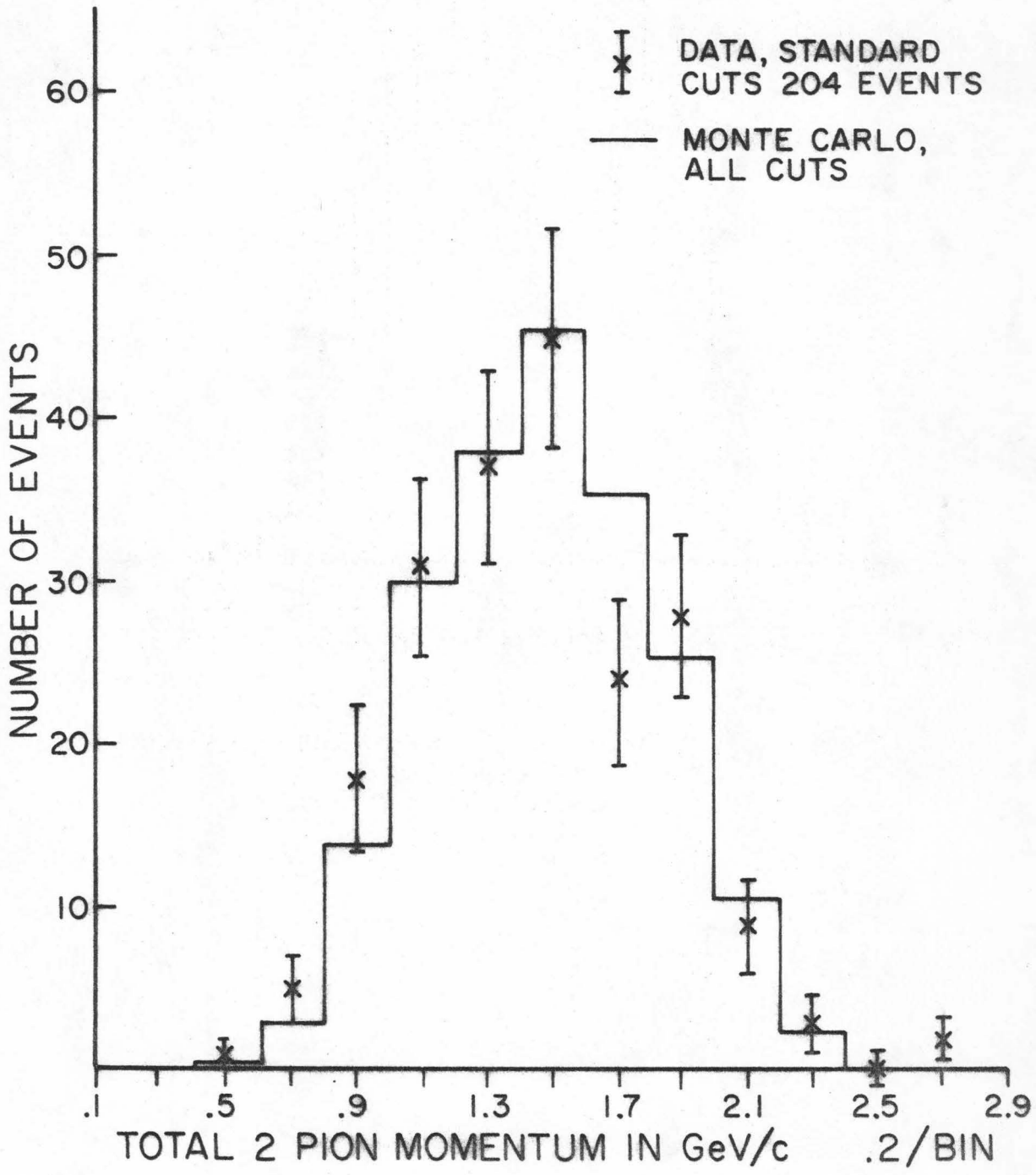

Figure 18 - Data to Monte Carlo comparison of the distributions of the sum (vector) of the two charged pion momenta ($K \rightarrow 3\pi$ data).

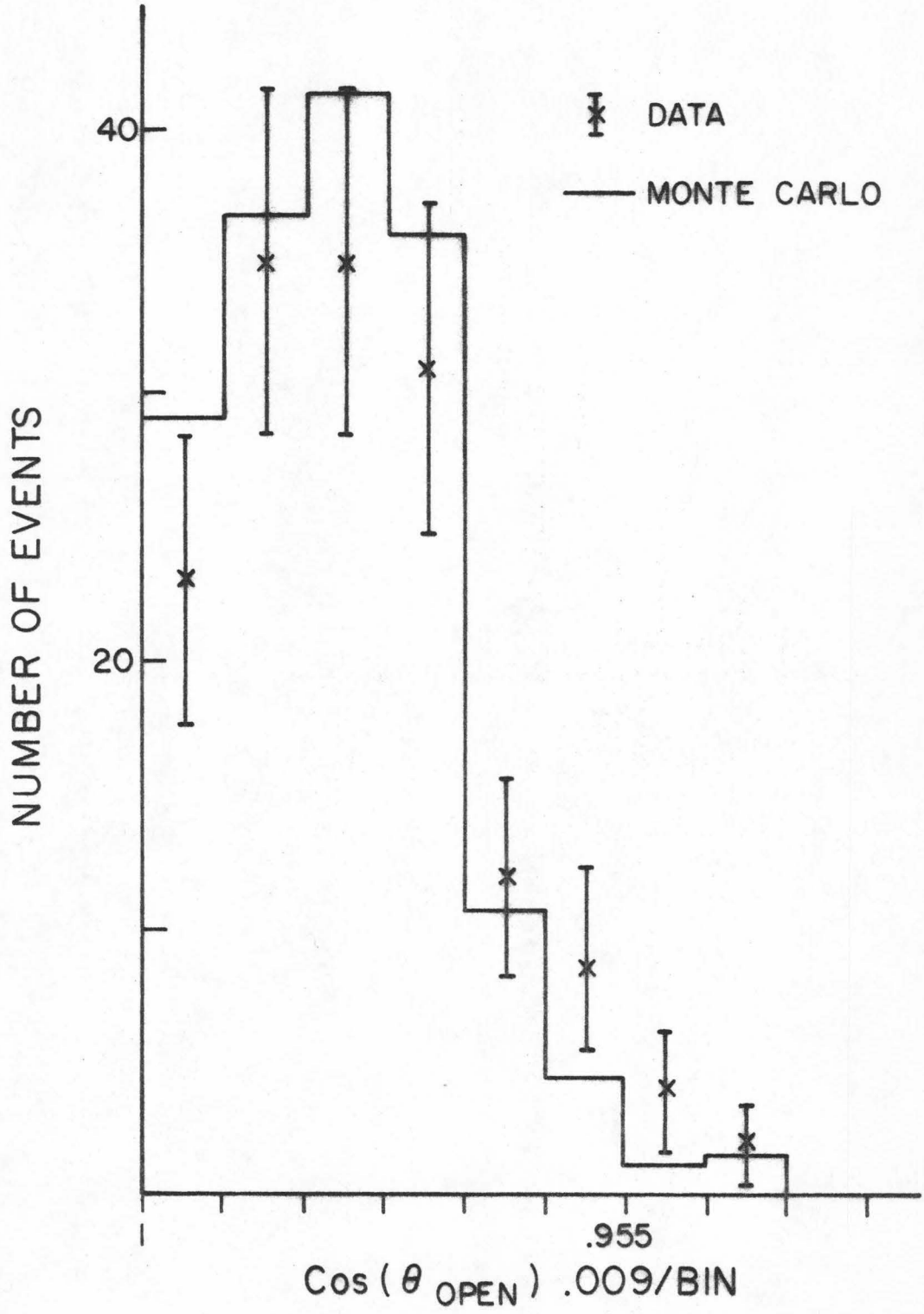

Figure 19 - Data to Monte Carlo comparison of the laboratory opening angle distributions of the charged pions ($K \rightarrow 3\pi$ data).

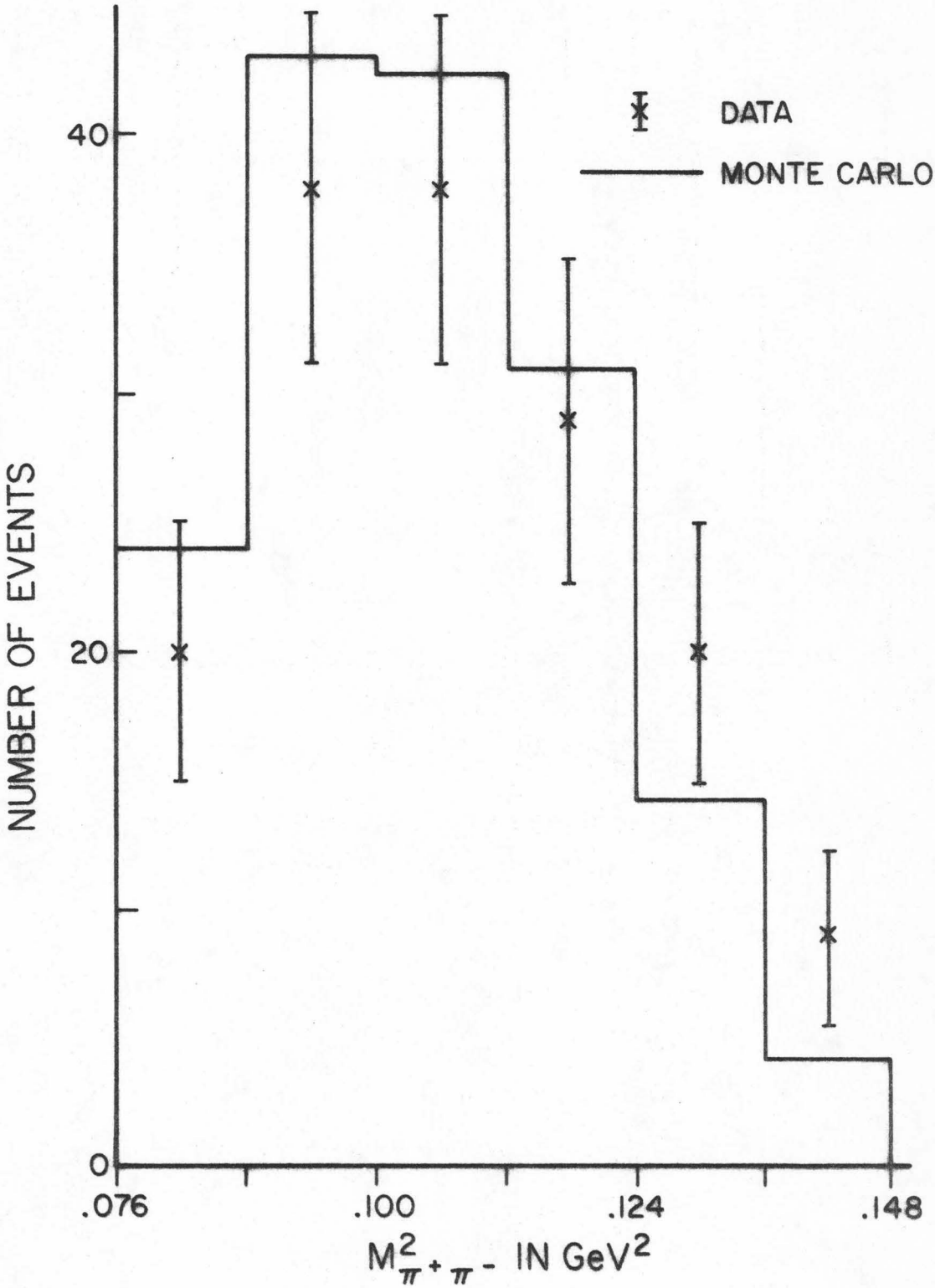

Figure 20 - Data to Monte Carlo comparisons of the $M^2_{\pi^+\pi^-}$ distributions for $K \rightarrow 3\pi$ events (mass resolution included).

As $M_{\pi^+\pi^-}$ went from .076 to .148 Gev^2 the full width went from .002 to .028 GeV^2 (the mass sq. resolution is one half the full width). The slight excess of events at large mass squared can be accounted for by either the presence of backgrounds ($K_S \rightarrow \pi^+\pi^-\gamma$, etc., see Chapter III) or an inadequate handling of the mass resolution. The fit in Figure 20 in general is good. The chi-square is 5.2 for 5 degrees of freedom.

To conclude this section, the efficiency function, $\epsilon_{3\pi}(L)$, slopes are correctly shown in Figure 12. Remnant systematic effects are not expected to alter these results beyond the statistical errors which are indicated. (The Monte Carlo calculation had more then four times as many events as the data sample.) The various comparison distributions show good agreement between the Monte Carlo calculation and the data.

Likelihood Fits to the Decay Distribution

The likelihood function that was used to fit the position distribution of decays in the Production-Decay Region is given in the following formula:

$$\mathcal{L}(W) = \frac{\prod_i \epsilon_i(L_i) N(L_i, W) dL_i}{\prod_i \int_{L_{min}}^{L_{max}} \epsilon_i(L_i) N(L_i', W) dL_i} \qquad (4.2)$$

where ReW = CPT violating parameter discussed in Chapter I.

ImW = CP violating parameter.

L_i = the decay position of event i.

$\epsilon_i(L)$ = the efficiency of event i at position L (see Fig.12).

L_{min} and L_{max} define the limits of the fiducial volume.

$N(L,W) = D(\bar{t},W)$.

$D(\bar{t}, W)$ is the time distribution discussed in Chapter I. The time ($\bar{t}$)

is taken to be the average time for events at that decay length, which is:

$\bar{t} = LM_K(\overline{\frac{1}{p_K}})/C$; see Appendix X.

M_K = The mass of the K_o(.498 Gev).

$(\overline{\frac{1}{p_K}})$ = The average value of the inverse of the K^o momentum.

C = The velocity of light.

Therefore, from equations (1.4), (4.2) and (4.3):

$$N(L,W) = 1 + (|W|^2)\, e^{-g\cdot L} + 2(\mathrm{ReW}\cos M\cdot L - \mathrm{ImW}\sin M\cdot L)e^{-g\cdot L/2} \tag{4.4}$$

$$M = M_K(\overline{\frac{1}{p_K}})(M_{K_L}-M_{K_S})/C$$

$$g = M_K(\overline{\frac{1}{p_K}})\cdot\gamma_S/C \; ; \quad \text{this formula makes the approximation } \frac{\gamma_L}{\gamma_S} \approx 0 .$$

where[14]:

$(M_{K_L}-M_{K_S})$ = .469 γ_S and is K_S, K_L mass difference.

γ_S = 1.16×10^{10}/sec = K_S decay rate.

$(\frac{1}{p_K})$ = .46/GeV/C

Using the above formulae a maximum likelihood fit was made to the parameters ReW and ImW. The best values of these parameters obtained are:

$$\mathrm{ReW} = -.05\ {}^{+.17}_{-.17} \qquad \mathrm{ImW} = +.38\ {}^{+.35}_{-.38} \tag{4.5}$$

Figure 21 contains the two-dimensional likelihood contours for variations of ReW and ImW. Figure 22 shows the data position distribution as

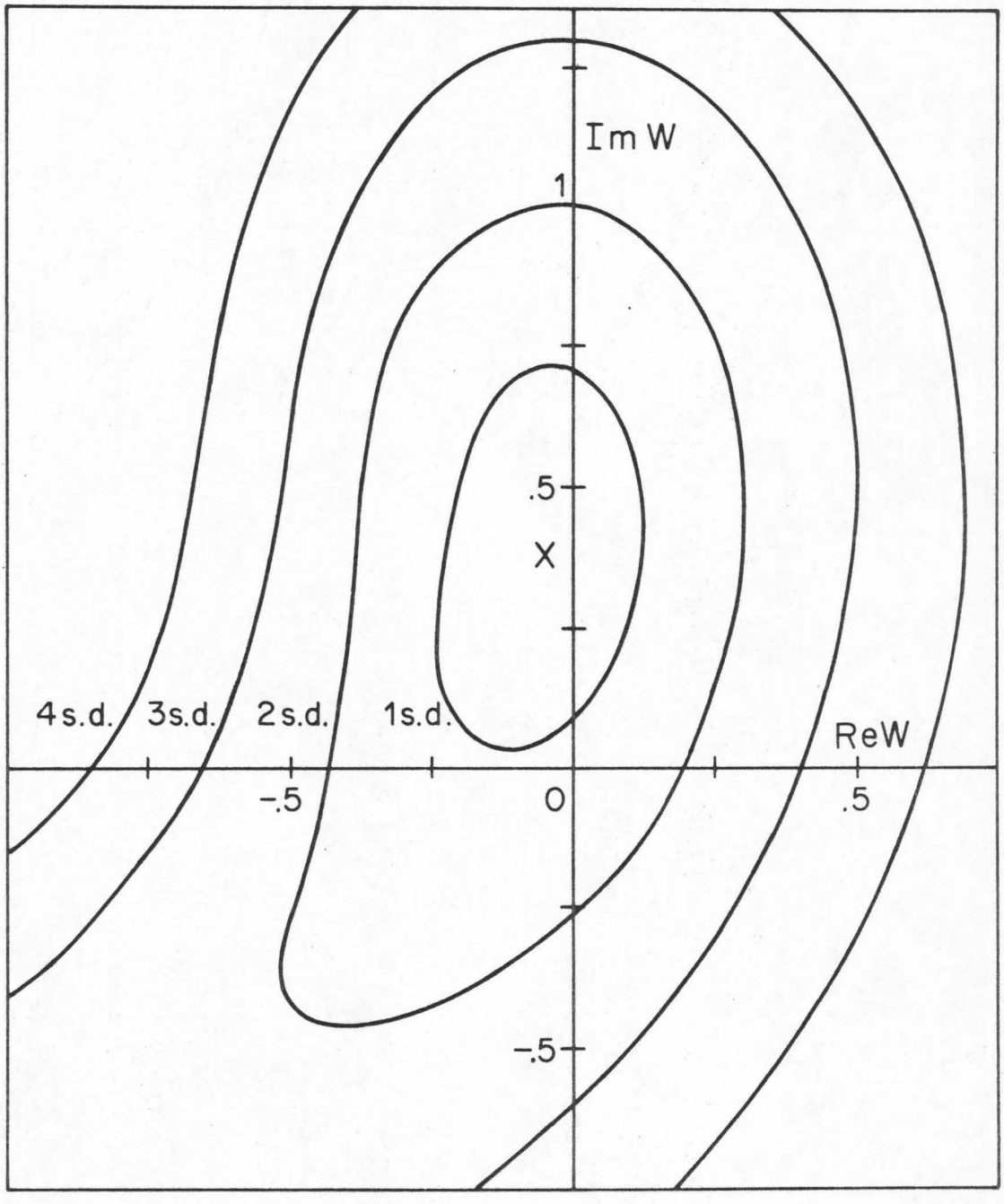

Figure 21 - Likelihood contours from fitting the $K \rightarrow 3\pi$ decay position distribution.

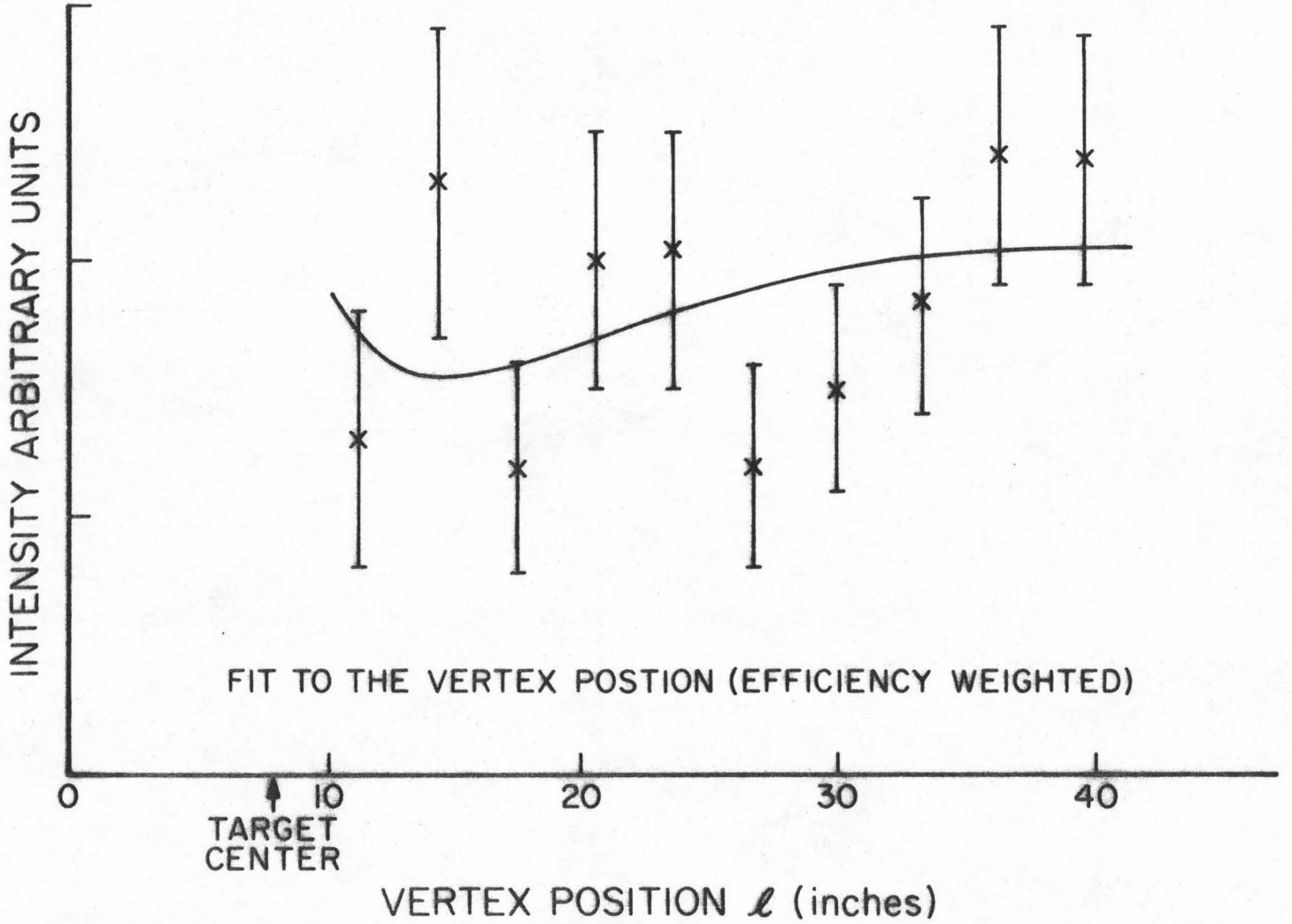

Figure 22 - Efficiency weighted $K \rightarrow 3\pi$ position distribution. Solid line is the best fit to W (result 4.5).

compared with the fitted curve (the efficiency has been taken out), with 7 degrees of freedom.

When the data is not efficiency weighted and is fit to a straight line, the slope/intercept is $\sigma = .10 \pm .11$ with a chi-square of 7.4 (with 8 d.f.) which corresponds to a probability of 48% (see Figure 23). When a straight line with a slope determined from the Monte Carlo calculation ($\sigma = .03 \pm .01$) normalized to the data, the chi-square is 9.47 (with 9 d.f.) corresponding to a probability of 40%. Thus W = 0 is very consistent with the results of this experiment.

In order to check the sensitivity of this fit to the various input parameters these parameters were varied and new fits were made. The results of these checks are listed in Table 8. The first column contains the changed parameter (only one parameter at a time is changed from the normal value). The subsequent columns contain the number of events in the fit, the chi-square of the fit, and the resultant fitted parameters (ReW, ImW).

The first row in Table 8 contains the results for the normal setting of all the parameters. These normal settings are:

$M_\Lambda > 1.2$ GeV

$M_K < .38$ GeV

$\langle \overline{\frac{1}{p_K}} \rangle = .46$ (GeV/C)$^{-1}$

$M_{K_L} - M_{K_S} = .544 \times 10^{10}$ sec^{-1}

$\gamma_S = 1.16 \times 10^{10}$ sec^{-1}

Low Field Efficiency = $1 + .025\,\ell = 1 + \sigma \cdot \ell$

High Field Efficiency = $1 + .040\,\ell$

π on Same Side Efficiency = $1 + .031\,\ell$

ℓ of Target Center = 8.0"

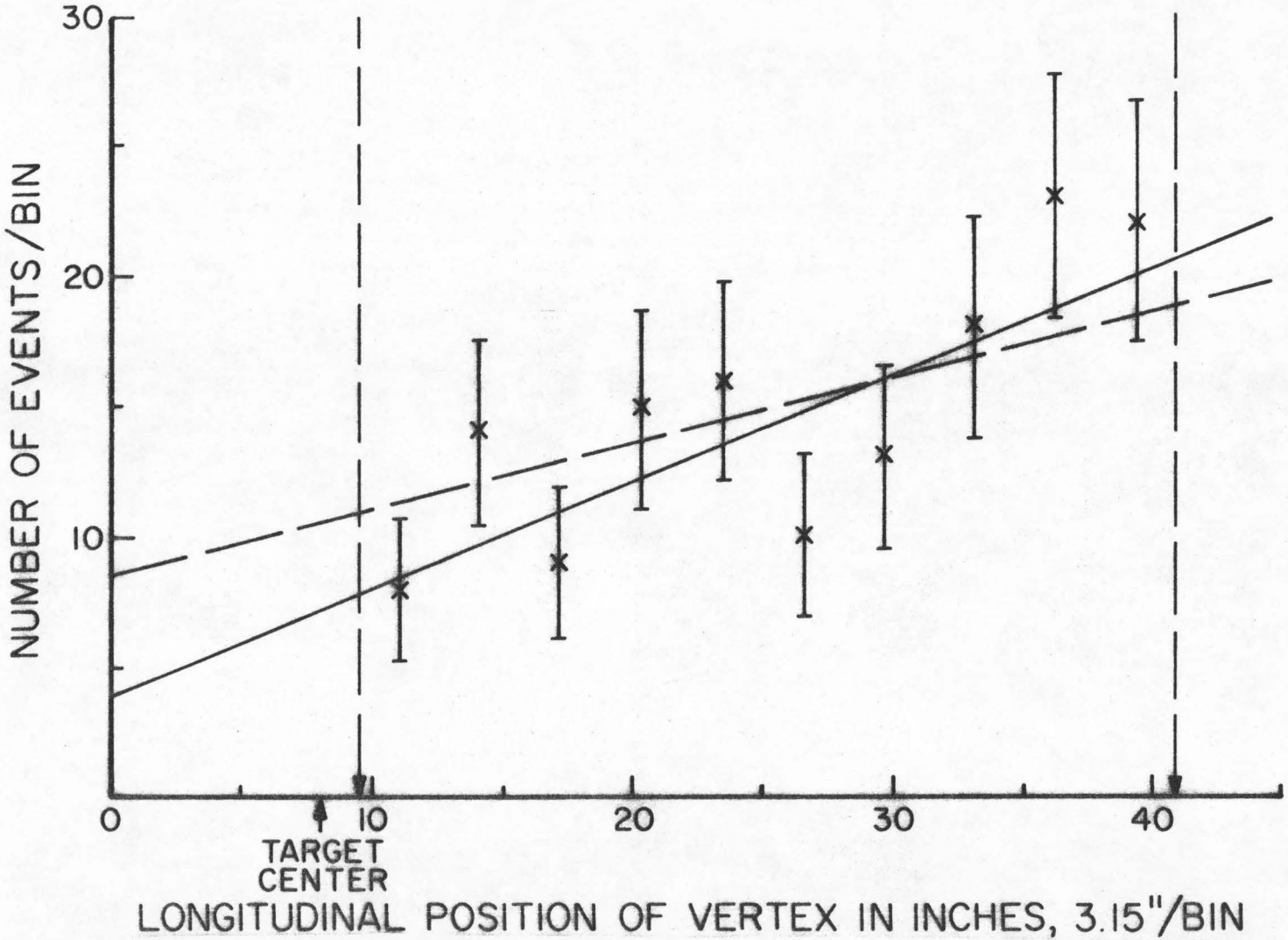

Figure 23 - Raw $K \rightarrow 3\pi$ position distribution. Dashed diagonal line is the efficiency function normalized to the total number of events and corresponds to a fit with W=0. Solid diagonal line is the least squares fit of the data to a straight line. Vertical dashed lines define the limits of the fiducial volume.

	Number of Events	χ^2	ImW	ReW
Normal	148	9.0	$-.05^{+.17}_{-.17}$	$+.39^{+.35}_{-.38}$
ℓTarget = 8.5"	151	9.0	$-.09^{+.18}_{-.13}$	$+.39^{+.30}_{-.37}$
ℓ of Target = 7.5"	151	9.0	$-.04^{+.19}_{-.19}$	$+.39^{+.35}_{-.35}$
ℓ Minimum = 9.2"	149	6.4	$-.06^{+.17}_{-.17}$	$+.39^{+.32}_{-.35}$
ℓ Minimum = 10.1"	145	6.8	$-.13^{+.20}_{-.17}$	$+.28^{+.33}_{-.30}$
ℓ Maximum = 38"	128	10.4	$-.06^{+.19}_{-.19}$	$+.25^{+.40}_{-.40}$
ℓ Maximum = 42"	152	5.6	$-.08^{+.20}_{-.14}$	$+.30^{+.35}_{-.40}$
$\frac{1}{\left\langle\frac{1}{p_K}\right\rangle} \rightarrow \frac{1}{\left\langle\frac{1}{p_K}\right\rangle} + .1$ GeV	151	8.8	$-.06^{+.20}_{-.16}$	$+.39^{+.33}_{-.34}$
$\frac{1}{\left\langle\frac{1}{p_K}\right\rangle} \rightarrow \frac{1}{\left\langle\frac{1}{p_K}\right\rangle} - .1$ GeV	151	9.0	$-.04^{+.16}_{-.18}$	$+.39^{+.33}_{-.34}$
Eff slope $\rightarrow$ Eff slope $-.02$	151	10.0	$-.17^{+.15}_{-.17}$	$+.50^{+.30}_{-.30}$
Eff slope $\rightarrow$ Eff slope $+.02$	151	8.6	$-.01^{+.20}_{-.17}$	$+.30^{+.35}_{-.37}$
$M_K < .36$	129	10.6	$-.01^{+.20}_{-.18}$	$+.25^{+.40}_{-.35}$
$M_K < .40$	157	11.2	$+.03^{+.20}_{-.16}$	$+.35^{+.36}_{-.32}$
$M_K < .42$	162	10.0	$+.08^{+.19}_{-.16}$	$+.30^{+.35}_{-.35}$
$M_\Delta > 1.175$	170	11.0	$+.04^{+.17}_{-.16}$	$+.43^{+.37}_{-.37}$
$M_\Delta > 1.225$	133	7.4	$0.^{+.20}_{-.19}$	$+.30^{+.37}_{-.37}$
$M_\Delta > 1.25$	116	10.0	$-.02^{+.21}_{-.21}$	$+.15^{+.35}_{-.45}$
$M_\Delta > 1.3$	85	4.8	$-.01^{+.23}_{-.23}$	$+.53^{+.40}_{-.45}$

TABLE 8 - Fits with Varied Inputs

$\ell_{min} = 9.5"$

$\ell_{max} = 41.0"$

where ℓ is the longitudinal position in the Production-Decay Region ($\ell - \ell_{target} = L$).

The next two rows contain the results for varying the position of the center of the brass target by $\pm.5"$. The next four rows test the dependence of the fit on the lower and upper limits of the fiducial volume. The next two rows result from subtracting and adding .02 to σ the slope/intercept of the efficiency function (e.g. $1 + .025\ell \rightarrow 1 + .045\ell$). (This variation is twice as great as the expected statistical and systematic errors in the Monte Carlo calculation.) The next three rows vary the K mass cut from .36 GeV to .42 GeV. The last five rows vary the position of the Λ-mass cut from 1.175 GeV to 1.3 GeV.

In all the above cases the fitted values of the parameters (ReW, ImW) deviate from the normal ones (first row) by less than 2/3 a standard deviation. The largest effects are found in the variation of the Λ-mass which adds or removes sizable fractions of the events. Therefore, the variations in the fitted parameters is probably just statistical in nature.

In all the above cases, when a background term was fit as well the result was that there were less than 10 background events of a short-lived nature (K_S's and Λ's, see Chapter III). Usually the presence of background makes itself felt in the ReW parameter. This can be seen in the row where $M_K < .42$ GeV and in the row where $M_\Lambda > 1.175$ GeV. In both cases ReW is shifted in a positive direction by the added short-lived background. On the other hand, ImW tends to be less affected by

this background because it is most sensitive to what happens at $t > 1.5\ \tau_{shorts}$ where the $e^{-\gamma t/2}\sin \Delta m t$ term reaches a maximum.

To conclude this chapter, the results of this experiment are consistent with W = 0 at the 40% confidence level. The systematic effects which have been investigated should not alter the results by more than 1/2 a standard deviation. The best values obtained for ReW and ImW were:

$$\mathrm{ReW} = -.05 \pm .17$$

$$\mathrm{ImW} = +.38\ ^{+\ .35}_{-\ .38} \ .$$

CHAPTER V - THE PHASE OF ε

The measurement of the CP violating transition matrix elements in all the decay modes of the K^o allows a determination of the phase ε (the CP violating parameter defined in equation 1.7). First order (in ε) perturbation theory gives (assuming CPT invariance) ε as[9]

$$\varepsilon = \frac{i(M_{K\bar{K}}-M^*_{K\bar{K}})+(\Gamma_{K\bar{K}}-\Gamma^*_{K\bar{K}})}{(\gamma_S-\gamma_L)+2i(m_S-m_L)} \tag{5.1}$$

where M and Γ are the hermitian mass and decay matrices of the Hamiltonian ($H = M+i\Gamma$) using the $|K\rangle$ and $|\bar{K}\rangle$ base states. The mass matrix M is a sum over transitions through off the mass shell intermediate states. The decay matrix Γ is a sum of transitions through on the mass shell intermediate states (see equation 1.6). Therefore Γ is experimentally accessible and M is not. If experiments show that $Im\Gamma_{K\bar{K}} \ll ImM_{K\bar{K}} \approx 2\varepsilon\left[(\gamma_S-\gamma_L)+2i(m_S-m_L)\right]$ the phase of ε is determined by the phase of the denominator in equation (5.1).

To determine $Im\Gamma_{K\bar{K}}$ we proceed as Lee and Wu[9]. The Γ matrix is defined in equation (1.6) in terms of the amplitudes, $\langle F|H_w|K\rangle$ and $\langle F|H_w|\bar{K}\rangle$, for transitions to on the mass shell intermediate states F. Invariance under CPT gives

$$A_F = \langle F|H_w|K\rangle = \langle \bar{K}|H_w|F\rangle = \langle F|H_w|\bar{K}\rangle^* \tag{5.2}$$

(The decay amplitude is obtained from A_F by multiplication by $e^{i\delta_F}$ where δ_F is the final state interaction phase shift.) From equation (1.6) we

get the contribution to $Im\Gamma_{K\bar{K}}$ from each intermediate state F (decay mode) as

$$(Im\Gamma_{K\bar{K}})_F = \frac{\pi\rho_F}{2}(A_F^{2*}-A_F^2) = 2\pi\rho_F(ReA_F)(-iImA_F) \tag{5.3}$$

where $2\pi\rho_F$ is the phase space of the decay mode F.

The decay modes which could give substantial contributions to $Im\Gamma_{K\bar{K}}$ are the 2π I=0 mode, the 2π I=2 mode, the 3π I=1 modes, the pion lepton modes, the 2π γ modes and the $\gamma\gamma$ mode. For convenience the contribution to $Im\Gamma_{K\bar{K}}$ from each mode will be expressed in terms of the K_L decay rate γ_L.

To begin there is one set of K^o, $\bar{K}^o$ decay amplitudes which can be defined to be real. (The relative phase of the K^o and $\bar{K}^o$ states is arbitrary.) If we choose this set to be the amplitudes into the I=0 2π state, then the contribution to $Im\Gamma_{K\bar{K}}$ comes from the I=2 mode entirely ($ImA_{2\pi,I=0} = 0$). The contribution from the I=2 mode is then $2\pi\rho_{2\pi}(ReA_2)\cdot(iImA_2)$. This term is expressed by a factor of 1/20 from the $\Delta I = 1/2$ rule ($\frac{ReA_{2\pi,I=2}}{A_{2\pi,I=0}} = .045$). The value of $ImA_{2\pi,I=2}$ can be extracted from measurements of the CP violating parameters η^{+-} and η^{oo} together with a knowledge of the final state interaction phase shifts for the I=0 and I=2 2π final states (δ_o and δ_2). Neglecting terms of order $\epsilon ReA_{2\pi,I=2}$ and assuming CPT invariance, we get for η^{+-} and η^{oo} ($A_o=A_{2\pi,I=0}$ and $A_2=A_{2\pi,I=2}$),

$$\eta^{+-} = \frac{\langle\pi^+\pi^-|H_w|K_L\rangle}{\langle\pi\ \pi\ |H\ |K_S\rangle} = \frac{e^{i\delta_2}(\epsilon ReA_2+iImA_2)+\epsilon\sqrt{2}A_o e^{i\delta_o}}{e^{i\delta_2}(ReA_2+i\epsilon ImA_2)+\sqrt{2}A_o e^{i\delta_o}} \approx \frac{\epsilon\sqrt{2}A_o+(iImA_2)^{i(\delta_2-\delta_o)}}{\sqrt{2}\,A_o} \tag{5.4a}$$

$$\eta^{oo} = \frac{\langle\pi^o\pi^o|H_w|K_L\rangle}{\langle\pi^+\pi^-|H_w|K_S\rangle} = \frac{\sqrt{2}e^{i\delta_2}(\epsilon ReA_2+iImA_2)-\epsilon A_o e^{i\delta_o}}{\sqrt{2}e^{i\delta_2}(ReA_2+i\epsilon ImA_2)-A_o e^{i\delta_o}} \approx \frac{\epsilon A_o-(\sqrt{2}iImA_2)e^{i(\delta_2-\delta_o)}}{A_o} \tag{5.4b}$$

so that $$\eta^{+-}-\eta^{oo} \approx \frac{3i(\mathrm{Im}A_2)}{\sqrt{2}\,A_o}\, e^{i(\delta_2-\delta_o)} \tag{5.5}$$

The final state interaction phase shift is found to be[9] $(\delta_o-\delta_2)=66^o\pm13^o$ by comparing the rates for $K^+ \to \pi^+\pi^o$, $K_S \to \pi^+\pi^-$ and $K_S \to \pi^o\pi^o$. The experimental measurements of $|\eta^{oo}|$ are inconsistent and the error in the phase is so large that it is best to put an upper limit on this mode. The data[2] is consistent with $|\eta^{oo}|< 2\ |\eta^{+-}|$ and the $\varphi^{oo} \approx \varphi^{+-} \pm 30^o$ (φ is the phase). Then the upper limit on $|\eta^{+-}-\eta^{oo}|$ is $< 2\times10^{-3}$. So

$$(i\mathrm{Im}\Gamma_{K\bar{K}})_{2\pi} = 2\pi\rho_{2\pi}(\mathrm{Re}A_2)(-i\mathrm{Im}A_2)=2\pi\rho_{2\pi}(\mathrm{Re}A_2)\left(\tfrac{\sqrt{2}}{3}A_o(\eta^{+-}-\eta^{oo})e^{i(\delta_o-\delta_2)}\right) \tag{5.6}$$

$$|(i\mathrm{Im}\Gamma_{K\bar{K}})_{2\pi}| \le (4\times10^{-5})2\pi\rho_{2\pi}A_o^{\,2} = .01\ \gamma_L$$

This error will be seen to be small compared to the errors in the other modes.

The contribution from the pion-electron modes comes from the imaginary part of the $\Delta S = \Delta Q$ violating parameter X:

$$X = \frac{\langle\pi^-e^+\nu|H_w|\bar{K}\rangle}{\langle\pi^-e^+\nu|H_w|K\rangle} = \frac{\langle\pi^+e^-\bar{\nu}|H_w|K\rangle^*}{\langle\pi^+e^-\bar{\nu}|H_w|\bar{K}\rangle^*}$$

where $X = 0$ implies $\Delta S = \Delta Q$. From equation (1.6):

$$2i\mathrm{Im}(\Gamma_{K\bar{K}})_{\pi^-e^+\nu} = \pi\rho_{\pi e\nu}\langle K|H_w|\pi^-e^+\nu\rangle\langle\pi^-e^+\nu|H_w|\bar{K}\rangle - \text{C.C.}$$
$$= 2\pi\rho_{\pi e\nu}|\langle K|H_w|\pi^-e^+\nu\rangle|^2\mathrm{Im}X$$

and similarly

$$2i\mathrm{Im}\ (\Gamma_{K\bar{K}})_{\pi^+e^-\bar{\nu}} = 2\pi\rho_{\pi e\nu}|\langle K|H_w|\pi^+e^-\nu\rangle|^2\mathrm{Im}X.$$

So neglecting the lepton asymmetry (of order ϵ) we get:

$$i(Im\Gamma_{K\bar{K}})_{\pi e\nu} = iImX\ \gamma_{K_L\to\pi e\nu} \tag{5.7}$$

The $K \to \pi u\nu$ mode is more complicated because of the presence of an additional form factor. Measurements of the $K_{\pi u\nu}$ time distribution yield the parameter X' (see Appendix XV equation AXV.3 for definition of X'). There are two experiments that have measured X'. These results are:

$$ReX' = -.05 \pm .09 \qquad ImX' = +.05 \pm .13 \text{ (reference 19)}$$

$$ReX' = .19\ {}^{+.13}_{-.18} \qquad ImX' = -.12\ {}^{+.20}_{-.17} \text{ (reference 25)}$$

giving the average:

$$ReX' = -.00 \pm .08 \qquad ImX' = .00 \pm .11 \tag{5.8}$$

Combining equations (XV.3) and (XV.11) we get:

$$(iIm\Gamma_{K\bar{K}})_{\pi u\nu} = i\left(Im\left\{X\left[(1.07)-(.077)\left(\frac{M_K}{m_u} - \xi\right)\right]\right\} + .077\frac{M_K}{m_u}ImX'\right)\gamma_{K_L\to\pi u\nu} \tag{5.9}$$

Combining (5.9) with (5.7), taking the branching ratio for Ku_3 and Ke_3 from reference (14), and assuming $\xi = -1$ and is real (see references 26 and 27) for measurements and note that results are insensitive to this assumption), we get:

$$(iIm\Gamma_{K\bar{K}})_{\text{all leptons}} = i(ImX(.84)+.15\ ImX')(\gamma_{K_L\to\text{all leptons}}) \tag{5.10}$$

Then using the value of ImX from the average in Table 9 and the value of ImX' from the average in result (5.8) we get the contribution to $Im\Gamma_{K\bar{K}}$ from the leptons to be:

$$i(\mathrm{Im}\Gamma_{K\bar{K}})_{\text{all leptons}} = i(-.007 \pm .015)\gamma_{K_L} \tag{5.11}$$

The contribution from the 3π mode comes from ImW. Starting with the definition of W in equation (1.3) we get (neglecting ε):

$$W = \frac{\langle 3\pi|H_w|K_S\rangle}{\langle 3\pi|H_w|K_L\rangle} = \frac{\langle K_L|H_w|3\pi\rangle\langle 3\pi|H_w|K_S\rangle}{|\langle 3\pi|H_w|K_L\rangle|^2}$$

where 3π is assumed to be the I=1 symmetric state.

So:

$$2|\langle 3\pi|H_w|K_L\rangle|^2 W = |\langle 3\pi|H_w|K\rangle|^2 - |\langle 3\pi|H_w|\bar{K}\rangle|^2 - \langle K|H_w|3\pi\rangle\langle 3\pi|H_w|\bar{K}\rangle$$

$$-\langle \bar{K}|H_w|3\pi\rangle\langle 3\pi|H_w|K\rangle$$

Taking just the imaginary part (implicitly assuming CPT) and using equation (1.6) we get:

$$2\pi\rho_{3\pi}|\langle 3\pi|H_w|K_L\rangle|^2 \; i\mathrm{Im}W = \pi\rho_{3\pi}\left[2i\mathrm{Im}\langle K|H_w|3\pi\rangle\langle 3\pi|H_w|\bar{K}\rangle\right]$$

$$\text{so: } i(\mathrm{Im}\Gamma_{K\bar{K}})_{3\pi} = \frac{i\mathrm{Im}W}{2}\,\gamma_{K_L\to 3\pi\ (\text{all } 3\pi)} \tag{5.12}$$

Using the compilation of this experiment and other recent experiments from Table 10 we have the 3π contribution to be:

$$i(\mathrm{Im}\Gamma_{K\bar{K}})_{3\pi} = (.041 \pm .028)\gamma_L \tag{5.13}$$

Finally taking the calculations of K.R. Schubert et al.[8] for the upper limit of .006 γ_L on the contributions from the $\pi\pi\gamma$ and the $\gamma\gamma$

Group	Method	Number of $K \to \pi \ell \nu$ Events	ReX	ImX	Ref.
Paris (1965)	FREON/Prop. B.C. $K^+N \to K^oP$	315	$.035^{+.11}_{-.13}$	$-.21^{+.11}_{-.15}$	(15)
Padua (1965)	Heavy Liquid B.C. $K^+N \to K^o$	152	$.06^{+.18}_{-.44}$	$-.44^{+.32}_{-.19}$	(16)
Columbia/ Rutgers (1965)	H_2 B.C. $\bar{p}$-p	109	$.08^{+.16}_{-.28}$	$.24^{+.40}_{-.30}$	(17)
Penn. (1966)	Sp.Chamber $\pi^-p \to K^o\Lambda$	116	$.17^{+.16}_{-.35}$	$.00 \pm .25$	(18)
Brookhaven/ Carnegie (1970)	D_2 B.C. $K^+N \to K^oP$	215	$.12 \pm .09$	$-.08 \pm .07$	(19)
Berkeley (1968)	D_2 B.C. $K^-p \to \bar{K}^oN$	252	$.25^{+.07}_{-.09}$	$.00 \pm .08$	(20)
CERN/Paris (1968)	H_2 B.C. $\bar{p}$-p	121	$.09^{+.13}_{-.11}$	$.22^{+.29}_{-.37}$	(21)
San Diego (1969)	Sp.Chamber $K^+Cu \to K^o$	686	$.09^{+.14}_{-.16}$	$-.11^{+.10}_{-.11}$	(22)
Caltech (1970)	Sp.Chamber $\pi^-Cu \to K^o$	1079	$-.070 \pm .036$	$.107^{+.092}_{-.075}$	(23)
Illinois/ Northeastern (1971)	$\pi^-C \to K^o\Lambda$	342	$-.13 \pm .11$	$-.04 \pm .16$	(24)
CERN/Orsay/ Vienna (1971)	$K^+p \to K^op\pi^+$	5800	$.05^{+.021}_{-.035}$	$-.01 \pm .02$	(25)
AVERAGE		9187	$.016 \pm .021$	$-.013 \pm .018$	
			$\chi^2 = 17.3$ with 10 d.f.	$\chi^2 = 10.7$ with 10 d.f.	

TABLE 9 - Ke_3 Compilation

Method	Number of $K \to 3\pi$ Events	ReW	ImW	Ref.
B.C. $K^+d \to K^o pp$	99	$.47\ ^{+.30}_{-.24}$	$-.12\ ^{+.44}_{-.45}$	(29)
B.C. $K^-p \to \bar{K}^o n$	50	$2.75\ ^{+.65}_{-.60}$ ReW=0 at 2 s.d.	$+.5\ ^{+.7}_{-.55}$	(30)
Heavy Liquid B.C. $K^+n \to K^o$	190		$+.34\ ^{+.19}_{-.59}$ Assumes ReW=0	(31)
Compilation of Results of Ref.(34) and (35) by Ref.(35).	71	$.05 \pm .30$	$-.15 \pm .45$	(32) (33)
B.C. $K^+p \to K^o+p+\pi^+$	98	$.01\ ^{+.22}_{-.20}$	$+.33\ ^{+.42}_{-.50}$	(34)
Wire Chamber $K^+p \to K^o+p+\pi^+$	400	$.45 \pm .35$	$.05 \pm .35$	(35)
Spark Chambers $\pi^-p \to \Lambda + K^o$	99	$-.09 \pm .19$	$+.56 \pm .43$	(36)
$\pi^-Cu \to K^o$	148	$-.05 \pm .17$	$+.39\ ^{+.35}_{-.37}$	This Exp.
Average	1155	$+.08 \pm .09$ $\chi^2=8.3$ with 6 d.f.	$.24 \pm .16$ $\chi^2=2.7$ widh 7 d.f.	

TABLE 10 - $K \to 3\pi$ Compilation

modes we combine the above subtotals (results 5.6, 5.11, and 5.13) to get:

$$i(\mathrm{Im}\Gamma_{K\bar{K}})_{all} = i(.034 \pm .034)\gamma_L \qquad (5.14)$$

This result is consistent with the super weak theory which would have $\mathrm{Im}\Gamma_{K\bar{K}} = 0$.

Using experimental values for γ_L, γ_S, m_L and m_S[14], the phase of the denominator in equation (5.1) is $43^o \pm .4^o$ and the magnitude is $1.37\gamma_S$. Taking a value for $\mathrm{Re}\epsilon = (1.49 \pm .14)\times10^{-3}$ from the electron charge asymmetry experiments of J. Steinberger et al;[3] and the "natural phase" of the denominator of equation (5.1) as the phase of ϵ then the magnitude of ϵ is $(2.04 \pm .20)\times10^{-3}$. The correction to the natural phase is then

$$\Delta\varphi^{\epsilon} = \left(\frac{180}{\pi}\right)\left(\frac{1}{1.37\gamma_S}\right)\frac{2\mathrm{Im}\Gamma_{K\bar{K}}}{|\epsilon|} = 2.3^o \pm 2.3^o$$

so the corrected phase of ϵ is:

$$\varphi^{\epsilon} = 45.3^o \pm 2.3^o \qquad (5.15)$$

and the corrected value of $|\epsilon|$ is:

$$|\epsilon| = (2.12 \pm .20)\times10^{-3} \ . \qquad (5.16)$$

The result (5.15) can now be used to place limits on other CP violation parameters in the K^o system. By adding two times equation (5.4a) to equation (5.4b) we get:

$$2\eta^{+-} + \eta^{oo} = 3\epsilon \qquad (5.17)$$

Using (5.15), (5.16), (5.17) and η^{+-} from ref. (2), we obtain for η^{oo}:

$$|\eta^{oo}| = (2.46 \pm .61)\times10^{-3} \qquad (5.18)$$

and $$\varphi^{oo} = 48.0^o \pm 7.9^o \qquad (5.19)$$

where φ^{oo} is the phase of η^{oo}.

The above value of φ^{ϵ} (result 5.15) together with the most recent data on $\mathrm{Re}\epsilon$[3], η^{+-} and η^{oo}[2] constitute an over constrained set of data. The CP violating parameter

$$\epsilon' = \frac{i\,\mathrm{Im}A_2}{\sqrt{2}\,A_o}\, e^{i(\delta_2-\delta_o)} \tag{5.20}$$

in the $K^o \to 2\pi$ transition amplitude can be determined with these results. First we decompose ϵ' into

$$\epsilon' = \epsilon'_{\|} + \epsilon'_{\perp} \tag{5.21}$$

where $\epsilon'_{\|}$ is parallel to η^{+-} and $\epsilon'_{\perp}$ is perpendicular to η^{+-} pointing towards the upper left-hand quadrant (see Figure 24). From equations (5.4a) and (5.20), the values for η^{+-} and our results for ϵ (5.15) and (5.16) we get (see Figure 24a):

$$\begin{aligned} \epsilon'_{\perp} &= (-.05 \pm .14)\times 10^{-3} \\ \epsilon'_{\|} &= (-.25 \pm .22)\times 10^{-3} \end{aligned} \tag{5.22}$$

Using the latest data on η^{oo} and η^{+-} with equations (5.5) and (5.20) we get (see Figure 24b):

$$\begin{aligned} \epsilon'_{\perp} &= (-.07 \pm .33)\times 10^{-3} \\ \epsilon'_{\|} &= (-.01 \pm .04)\times 10^{-3} \end{aligned} \tag{5.23}$$

Average the results (5.17) and (5.18):

$$\begin{aligned} \epsilon'_{\perp} &= (-.05 \pm .13)\times 10^{-3} \\ \epsilon'_{\|} &= (-.02 \pm .04)\times 10^{-3} \end{aligned} \tag{5.24}$$

We find therefore that

$$|\epsilon'| \lesssim .1\ |\epsilon| \ , \tag{5.25}$$

and that the $K \to 2\pi$ CP violation lies principally in the K^o eigenstates.

To summarize the analysis of this chapter, the compilation of Ke_3 and $K_{3\pi}$ data in Tables 9 and 10 have been used with upper limits on

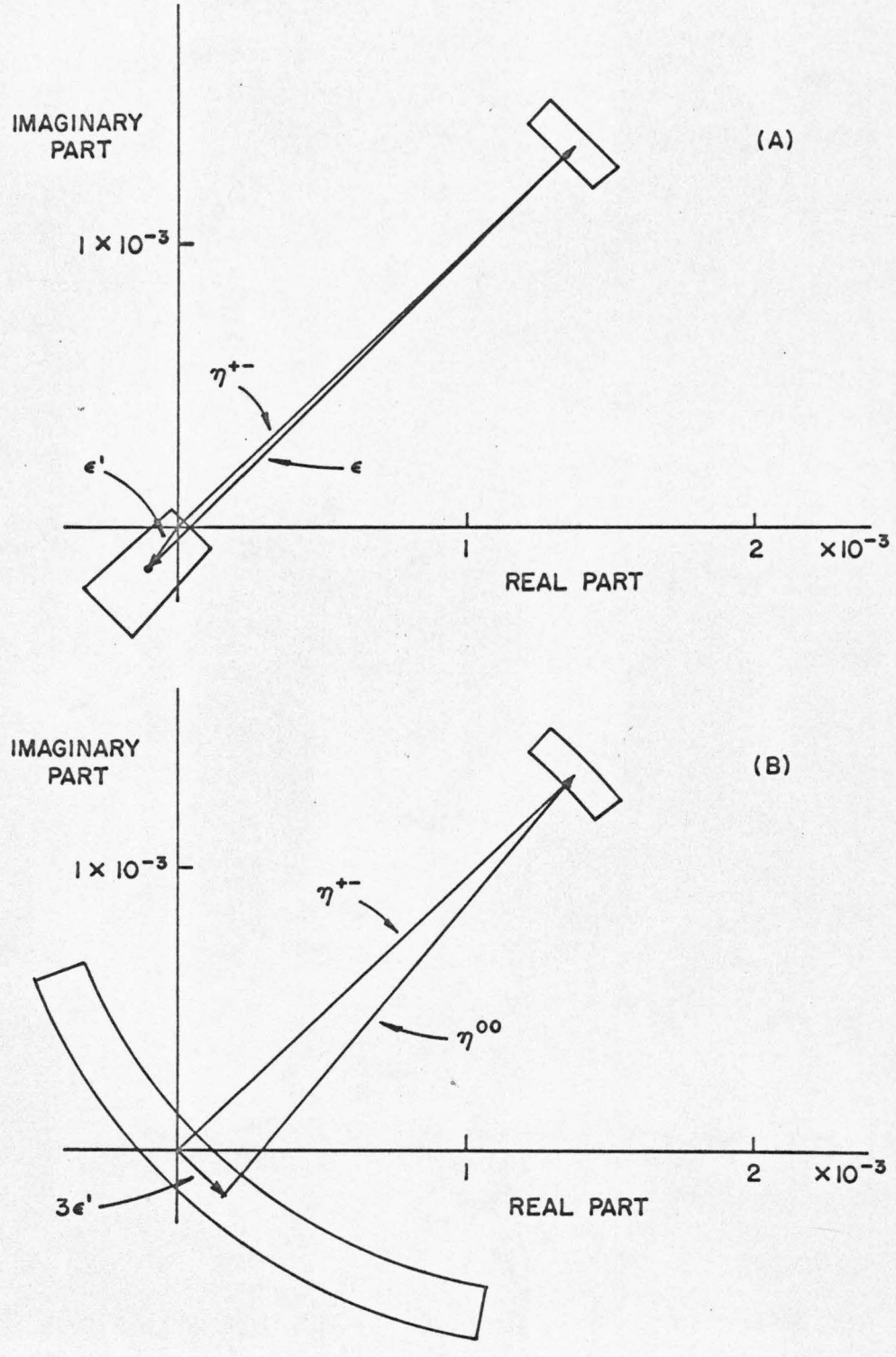

Figure 24 - A) ε' from ε and η^{+-}.
B) ε' from η^{+-} and η^{00}.

CP violation in other modes to obtain the phase of ϵ (result 5.15). The assumptions used for this purpose were CPT invariance, lepton universality and the dominance of the I=1 symmetric states in $K \to 3\pi$. Result (5.15) was then combined with the phase of η^{+-} to obtain the phase of η^{oo} (result 5.19); with the value of $Re\epsilon$ to obtain $|\epsilon|$ (result 5.16); with the values of η^{+-} and $Re\epsilon$ to obtain $|\eta^{oo}|$ (result 5.18); and with the values of η^{+-}, $Re\epsilon$ and η^{oo} to obtain limits on $|\epsilon'|$ (result 5.25). All the above results are consistent with the super weak theories which would place the observed CP violation in the K_S and K_L states. Partial justification for the assumption of CPT invariance in this analysis can be obtained from the analysis of K. R. Schubert et al.[8] who have found that the K_S and K_L states conserve CPT to $\pm$ .07%.

CHAPTER VI - CONCLUSIONS

The best fit to the final data sample of 148 $K^o \rightarrow \pi^+\pi^-\pi^o$ events in this experiment gives:

$$\begin{aligned} \mathrm{ReW} &= -.05 \pm .17 \\ \mathrm{ImW} &= +.39 \begin{matrix} + .35 \\ - .38 \end{matrix} \end{aligned} \tag{6.1}$$

Systematic effects from the Monte Carlo calculation and the experimental procedures are expected to produce errors which are small compared to the statistical error quoted above. The data is consistent with W = 0 at the 40% confidence level. Thus the results of this experiment are consistent with CP and CPT invariance in the transition amplitudes for K^o and $\overline{K}^o$ into three pions. The result for this experiment, however, does not rule out the possibility of a "maximal" CP violation ($\mathrm{ImW} \approx 1$) as described by Glashow.

A somewhat better value for W has been obtained by combining the results of this experiment with those of similar experiments. This has been done in Table 10 of Chapter V. The weighted average of these quoted experiments is:

$$\begin{aligned} \mathrm{ReW} &= (.08 \pm .09) \\ \mathrm{ImW} &= (.24 \pm .16) \end{aligned} \tag{6.2}$$

Again the results are consistent both with CP and CPT invariance but do not rule out the possibility of a large CP violation. Experiments with greater than several thousand events are needed to rule out this possibility. An alternative to high statistics experiments with mixed $K_S K_L$ states is to

look at the decay of a pure K_S state for the 3π mode. Such a state is obtainable from reactions such as:

$$\bar{p} + p \rightarrow K_S + K_L$$

$$\varphi \rightarrow K_S + K_L \quad .$$

These experiments would not determine the phase of W but could put clean upper limits on $|W|$.

Though the world average (result 6.2) still cannot rule out a maximal CP violation in this decay, it can be used with the results of experiments in other decay modes to obtain a useful determination of the phase of ϵ. This was done in Chapter V with the result (equation 5.10):

$$\varphi^{\epsilon} = 45.3 \pm 2.3 \text{ degrees.} \qquad (6.3)$$

This in turn leads to a determination of the phase of η^{oo} (equation 5.14):

$$\varphi^{oo} = 48.0 \pm 7.9 \text{ degrees.} \qquad (6.4)$$

This result has 1/4 the error of present measurements of φ^{oo}. The error in φ^{ϵ} arises mainly from the errors in the $K \rightarrow 3\pi$ measurement. The error in φ^{oo} comes equally from the error in φ^{ϵ} and φ^{+-} (the phase of η^{+-}). Therefore a new generation of experiments (order of magnitude greater statistics) will have to be done to reduce these errors substantially.

Further results of the analysis in Chapter V are:

$$|\epsilon| = (2.12 \pm .20)\times 10^{-3} \qquad (6.4)$$

$$|\eta^{oo}| = (2.46 \pm .61)\times 10^{-3} \qquad (6.5)$$

$$|\epsilon'| < .1\,|\epsilon| \qquad (6.6)$$

Results (6.4) and (6.5) are sensitive primarily to Reϵ and $|\eta^{+-}|$ and are insensitive to φ^{ϵ}. Result (6.6) is most sensitive to $|\eta^{+-}|$, $|\eta^{oo}|$, φ^{ϵ}, and φ^{+-}. It implies that the observed CP violation in $K \to 2\pi$ is primarily in the K_S K_L states. Thus the analysis of Chapter V is consistent with no CP violating amplitudes in $K_{2\pi}$, Ke_3, $K\mu_3$, and $K_{3\pi}$ decays and is therefore consistent with the superweak theories. The possibility of such CP violating amplitudes with magnitudes (relative to the CP conserving amplitudes) greater than $|\epsilon|$ still exists, however, for the Ke_3, $K\mu_3$, and $K_{3\pi}$ modes and will not be ruled out by experiment for some time.

APPENDIX I - CP AND THE TWO PION STATE

The pion is an isospin one-object and is therefore represented by a three-component vector

$$\psi_\pi = |i\rangle \quad , \qquad i = -1,\ 0,\ 1 \quad .$$

The operation of charge conjugation (C) reverses the third component of isotropic spin (i).

$$C\psi_\pi = C|i\rangle = |-i\rangle \quad .$$

The pion is pseudo scalar and therefore the parity operation (P) changes the sign of the state

$$P\psi_\pi = -\psi_\pi$$

Because the pion is spin zero it's possible states are subject to the restrictions of Bose statistics. Therefore the multi-pion state must be symmetric under the interchange of any two pions

$$\psi_{ijk} = \psi_{jik} = \psi_{ikj} = \psi_{kji} \quad .$$

In the above expansion ψ is the product of the spatial wave functions, the spin wave functions, and the isospin wave functions of the multi-pion state. The pion is spin zero so the spin wave function is automatically symmetric. Therefore the symmetry of the space function must combine with the symmetry of the isospin function to produce a symmetric state.

The states of total isotropic spin for the two pion state are shown below.

$I_{total} = 2$	$I_3 = 2$	$(1,1)$
	$I_3 = 1$	$\left[(1,0) + (0,1)\right]/\sqrt{2}$
	$I_3 = 0$	$\left[(1,-1) + 2(0,0) + (-1,1)\right]/\sqrt{6}$
	$I_3 = -1$	$\left[(-1,0) + (0,-1)\right]/\sqrt{2}$
	$I_3 = -2$	$(-1,-1)$
$I_{total} = 1$	$I_3 = 1$	$\left[(1,0) - (0,1)\right]/\sqrt{2}$
	$I_3 = 0$	$\left[(1,-1) - (-1,1)\right]/\sqrt{2}$
	$I_3 = -1$	$\left[(0,-1) - (-1,0)\right]/\sqrt{2}$
$I_{total} = 0$	$I_3 = 0$	$\left[(1,-1) + (-1,1) - (0,0)\right]/\sqrt{3}$

The symbol (i,j) represents the two-pion state where i is the third component of isospin of the first pion (the order "labels" the pions) and j is the same for the second pion.

We note that interchanging the order (labels) of the two pions leaves the I = 0 and I = 2 states unaffected and changes the sign of the I = 1 state. Therefore the states of total isotropic spin zero and two of the two pions are symmetric under interchange and the state of total isospin one is anti-symmetric.

The symmetry of the two particle spatial wave function is given by $(-1)^{\ell}$ where ℓ is the orbital angular momentum. Therefore the I = 0,2 states must have <u>even</u> orbital angular momentum and the I = 1 state <u>odd</u> orbital angular momentum in order for the total wave function to be symmetric.

Next, we note that the I = 0,2; $I_3 = 0$ states are <u>even</u> under C and the I = 1; $I_3 = 0$ states are <u>odd</u> where C is defined by:

$$C(i,j) = (-i,-j)$$

The operation of P on the spatial function is given by:

$$P\psi_{space}(\ell) = (-1)^{\ell}\,\psi_{space}(\ell)$$

Therefore the combined operation of CP on the neutral two-pion Bose allowed state is always even. The symmetry of the C operation always balances that of the P operation. This comes about through the Bose requirement that matches even total isotropic spin with even orbital angular momentum (and odd with odd).

Because the 2π state is CP even by Bose statistics then the observation of both K_S and K_L decay into two pions is evidence that either CP is violated in the decay, or the K_S and K_L are not eigenstates of CP, or Bose statistics is violated.

APPENDIX II - K^o-DECAY INTO THREE PIONS

There are 27 isospin states (3x3x3) that can be formed with three pions. Seven of these states are electrically neutral (I_3=0). Extending the formalism of Appendix I they are listed below.

Totally symmetric:

$$I=3 \quad \frac{1}{\sqrt{10}}\Big[2(0,0,0)+(1,0,-1)+(1,-1,0)+(0,1,-1)+(0,-1,1)+(-1,0,1)+(-1,1,0)\Big]$$

Anti-symmetric under 1 and 3 exchange only:

$$I=2 \quad \frac{1}{\sqrt{12}}\Big[2\big\langle(-1,0,1)-(1,0,-1)\big\rangle+(0,-1,1)-(0,1,-1)+(-1,1,0)-(1,-1,0)\Big]$$

Symmetric under 1 and 3 exchange only:

$$I=2 \quad \frac{1}{2}\Big[(-1,1,0)+(0,1,-1)-(0,-1,1)-(1,-1,0)\Big]$$

Anti-symmetric under 1 and 3 only:

$$I=1 \quad \frac{1}{2}\Big[(0,-1,1)+(0,1,-1)-(-1,1,0)-(1,-1,0)\Big]$$

Symmetric under 1 and 3 only:

$$I=1 \quad \frac{1}{\sqrt{12}}\Big[-2\big\langle(-1,0,1)+(1,0,-1)\big\rangle+(0,1,-1)+(0,-1,1)+(1,-1,0)+(-1,1,0)\Big]$$

Totally symmetric:

$$I=1 \quad \frac{1}{\sqrt{15}}\Big[3(0,0,0)-(1,0,-1)-(1,-1,0)-(0,1,-1)-(0,-1,1)-(-1,0,1)-(-1,1,0)\Big]$$

Totally anti-symmetric:

$$I=0 \quad \frac{1}{\sqrt{6}}\Big[-(0,1,-1)+(0,-1,1)-(1,-1,0)+(1,0,-1)-(-1,0,1,)+(-1,1,0)\Big]$$

The I=3 state and the I=0 state are uniquely specified. On the other hand, the three I=1 states and the two I=2 states are specified by a

convention which brings out their symmetry properties (any linear combination within the isospin multiplet is a valid eigenstate of isospin). The symmetry properties of the states are described above them. The states that possess symmetry only under the interchange of pions 1 and 3 mix among themselves (in their isospin multiplet) under the interchange of 1 and 2 or 2 and 3. These states possess "mixed" symmetry and must be handled carefully to obtain states allowed by Bose statistics.

Defining the operation of charge conjugation (C) by:

$$C(i,j,k) = (-i,-j,-k)$$

i,j,k are the third components of isotopic spin for the individual pions. Then it is easily verified that

$$C\psi_{\text{isospin}}(I) = (-1)^{I+1}\,\psi_{\text{isospin}}(I)$$

for the $I_3=0$ three pion states.

The total angular momentum of the K^o is zero and so we are only interested in pion states of zero total angular momentum. Therefore parity (P) operating on these three pion states is negative (the product of the 3 negative intrinsic parities of the pions). Therefore the value of CP for these states is given by:

$$CP\left[\psi_{\text{space}}\psi_{\text{isospin}}(I)\right] = (-1)^{I}\left[\psi_{\text{space}}\psi_{\text{isospin}}(I)\right]$$

$$CP = (-1)^{I}$$

We return now to the question of forming totally symmetric states (Bose allowed) by combining the isospin function with a suitable space function. The I=3 and I=1 totally symmetric isospin functions meet the Bose requirement with a totally symmetric space state. This is simply the $\ell=0$ state

with no internal angular momentum. Expressed in momentum space, ψ is:

$$\psi_{space}(P_1,P_2,P_3) = 1$$

where $P_1P_2P_3$ are the four momenta of the individual pions.

The I=0 totally antisymmetric state must be combined with a totally antisymmetric momentum space wave function to yield an allowed Bose state. The lowest order (in internal angular momentum) function that meets this requirement is

$$\psi_{\substack{space \\ anti\text{-}sym.}}(P_1,P_2,P_3) = \frac{(P_1\cdot P_2-P_2\cdot P_3)(P_1\cdot P_3-P_2\cdot P_3)(P_1\cdot P_2-P_1\cdot P_3)}{\text{normalization}}$$

This wave function is a function of the relativistic dot products $(P_i\cdot P_j)$ in order for it to be invariant under relativistic transformations. The products $P_i\cdot P_i$ are not included because they just yield a constant ($P_i\cdot P_i = M_\pi^2$). At this point it should be noted that each momentum factor produces a centrifugal barrier factor of $(KR) \approx 1/3$ in the transition amplitude. (K is the wave number of the pion and R is the interaction radius.) Therefore, the I=0 state is suppressed by a factor of $(KR)^6$ because the momentum space wave function is a function of the sixth power of the momenta.

For the states of mixed symmetry the situation is somewhat more complicated. It turns out that from these states only one I=2 state and one I=1 state can be formed that satisfies Bose statistics. The I=2 state, apart from normalization, is:

$$\begin{aligned}
&(P_1\cdot P_2)\big[+(0,1,-1)-(0,-1,1)+(1,0,-1)-(-1,0,1)\big] \\
&+(P_2\cdot P_3)\big[-(1,-1,0)+(-1,1,0)-(1,0,-1)+(-1,0,1)\big] \\
&+(P_3\cdot P_1)\big[+(1,-1,0)-(-1,1,0)-(0,1,-1)+(0,-1,1)\big]
\end{aligned}$$

The I=1 state is:

$$(P_1 \cdot P_2)\left[2(1,-1,0)+2(-1,1,0)-(0,1,-1)-(0,-1,1)-(1,0,-1)-(-1,0,1)\right]$$
$$+(P_2 \cdot P_3)\left[-(1,-1,0)-(-1,1,0)+2(0,1,-1)+2(0,-1,1)-(1,0,-1)-(-1,0,1)\right]$$
$$+(P_3 \cdot P_1)\left[-(1,-1,0)-(-1,1,0)-(0,1,-1)-(0,-1,1)+2(1,0,-1)+2(-1,0,1)\right]$$

It is straightforward to verify that these states are symmetric under the interchange of any two pions (interchange the indices in the space part and the order in the isospin part). Two powers of the momenta are involved in the space part so the centrifugal barrier factor for these states is $(KR)^2$.

Besides the centrifugal barrier effects, suppression factors arise for two other reasons. First, the I=3 and I=1 totally symmetric states are reduced by factors of $\sqrt{3/5}$ and $\sqrt{2/5}$ respectively because we are only looking at the $\pi^+\pi^-\pi^o$ pieces of these states and ignoring (not measuring) the $\pi^+\pi^-\pi^o$ piece. The second reason for reduction of the transition amplitude is the $\Delta I=1/2$ rule. K^o's are I=1/2 objects so transition to any state except the I=1 and I=0 states are suppressed by a factor of $A_{3/2}$ for the I=2 state and $A_{5/2}$ for the I=3 state. Experiments on the charged and neutral $K \to 3\pi$ transition indicate that $A_{3/2} \approx 1/20$ and $A_{5/2} < A_{3/2}$.

The results of the preceding discussion are summarized in Table 11. From this table we see that transitions to CP even states are suppressed by factors in excess of 100 in comparison to CP odd states. Furthermore the I=1 states are dominant over all others by at least a factor of 20. Given the statistical accuracy of this experiment (±30%) the I=1, CP=-1 states are completely dominant and any detectable interference terms must arise from a CP violating $K_S \to 3\pi_{I=1}$ amplitude. It should also be remarked that if the

I	CP	Exchange Symmetry	Centrifugal Barrier	ΔI	ΔI=1/2 Rule	Isospin Factor	Total Reduction Factor
3	-	Totally symmetric	1	5/2,7/2	$5/2 < \frac{1}{20}$	$\sqrt{3/5}$	$< \frac{1}{20}\sqrt{3/5}$
2	+	Mixed symmetry	~1/10	3/2,5/2	$3/2 \approx \frac{1}{20}$	1	$\approx 1/200$
1	-	Mixed symmetry	~1/10	1/2,3/2	1	1	$\approx 1/10$
1	-	Totally symmetric	1	1/2,3/2	1	$\sqrt{2/5}$	$\sqrt{2/5}$
0	+	Totally anti-symmetric	~1/1000	1/2	1	1	$\approx 1/1000$

TABLE 11 - $K^o \rightarrow \pi^+\pi^-\pi^o$ Bose Allowed Transitions

experimental procedure does not (this experiment does because of the Λ cut) induce any asymmetry in the Dalitz plot, then the CP even states cannot interfere with the CP odd states. They would simply produce a term in the time distribution of the form

$$\text{Rate(CPallowed } K_S \to 3\pi_{I=2}) \approx (\frac{1}{4\times10^4})e^{-t/\gamma_S}$$

Therefore with high enough statistics ($\approx 10^6$ events) it would be possible to observe a CP violating $K_S \to 3\pi$ amplitude of the same order as that which has been observed in $K_L \to 2\pi$ (2×10^{-3}).

APPENDIX III - CP AND CPT VIOLATION IN $K \to 3\pi$

This appendix discusses the nature of possible CP and CPT violations in K^o decay into 3π. To begin we define the amplitudes for reactions (1.1a) and (1.1b) as in Chapter I:

$$\langle \pi^+\pi^-\pi^o | H_w | K^o \rangle = Ye^{i\varphi}$$

$$\langle \pi^+\pi^-\pi^o | H_w | \bar{K}^o \rangle = -\bar{Y}e^{i\bar{\varphi}}$$

Further we define the operation of charge conjugation (C) by:

$$C|K^o\rangle = -|\bar{K}^o\rangle \qquad (\therefore CP|K^o\rangle = |\bar{K}^o\rangle)$$

and note that CP invariance is defined by $(CP)H_w(CP)^{-1} = H_w$. Then assuming that the I = 1 three pion states are dominant (see Appendix II),

$$\langle \pi^+\pi^-\pi^o | H_w | K^o \rangle = Ye^{i\varphi}$$

$$\langle \pi^+\pi^-\pi^o | (CP)^{-1}(CP)H_w(CP)^{-1}(CP) | K^o \rangle = Ye^{i\varphi}$$

$$-\langle \pi^+\pi^-\pi^o | H_w | \bar{K}^o \rangle = Ye^{i\varphi}$$

$$+\bar{Y}e^{i\bar{\varphi}} = Ye^{i\varphi} \ .$$

Therefore CP invariance implies: $\varphi = \bar{\varphi}$ and $Y = \bar{Y}$. To see the consequences of CPT invariance we assume that only the I = 1 symmetric three pion state is dominant and note that

$$T|3\pi_{in}\rangle = \langle 3\pi_{out}|$$

and $$|3\pi_{in}\rangle = e^{2i\delta}|3\pi_{out}\rangle$$

where δ is the final state interaction phase shift. Then CPT invariance gives

$$CPT\ H_w(CPT)^{-1} = H_w$$

and

$$\langle 3\pi_{out}|H_w|K^o\rangle = Ye^{i\varphi}$$

$$\langle 3\pi_{out}|(CPT)^{-1}H_w(CPT)^{-1}(CPT)|K^o\rangle = Ye^{i\varphi}$$

$$-\langle \bar{K}^o|H_w|3\pi_{in}\rangle = Ye^{i\varphi}$$

$$-\langle 3\pi_{in}|H_w|\bar{K}^o\rangle = Ye^{-i\varphi}$$

$$-e^{-2i\delta}\langle 3\pi_{out}|H_w|\bar{K}^o\rangle = Ye^{-i\varphi}$$

$$+\bar{Y}e^{i\bar{\varphi}-2i\delta} = Ye^{-i\varphi}$$

Therefore CPT invariance implies:

$$Y = \bar{Y}$$

and

$$\varphi + \bar{\varphi} = 2\delta + N\pi \qquad (N = 0,2,4,\ldots)$$

CP and CPT invariance together imply:

$$\varphi = \bar{\varphi} = \delta + M\pi \quad (M = 0,1,2,\ldots)$$

and

$$Y = \bar{Y} \ .$$

To see the relationship of the above discussion to W (see equation 1.3) we neglect terms of order ε (see Chapter I) and define:

$$|K_S\rangle = \frac{1}{\sqrt{2}}\left(|K^o\rangle + |\bar{K}^o\rangle\right)$$

$$|K_L\rangle = \frac{1}{\sqrt{2}}\left(|K^o\rangle - |\bar{K}^o\rangle\right)$$

and note that by the above definition of CP we get:

$$CP|K_S\rangle = |K_S\rangle$$

and

$$CP|K_L\rangle = -|K_L\rangle$$

Assuming the I = 1 3π states are dominant then

$$\langle 3\pi|(CP)^{-1}(CP)H_w(CP)^{-1}(CP)|K_S\rangle = -\langle 3\pi|H_w|K_S\rangle$$

so that CP invariance implies:

$$\langle 3\pi|H_w|K_S\rangle = 0$$

and from equation (1.3):

$$W = \frac{\langle 3\pi|H_w|K_S\rangle}{\langle 3\pi|H_w|K_L\rangle} = 0 \quad .$$

Also:

$$W = \frac{\langle 3\pi|H_w|K^o\rangle+\langle 3\pi|H_w|K^o\rangle}{\langle 3\pi|H_w|K^o\rangle-\langle 3\pi|H_w|K^o\rangle}$$

$$W = \frac{Ye^{i\varphi}-\bar{Y}e^{i\bar{\varphi}}}{Ye^{i\varphi}+\bar{Y}e^{i\bar{\varphi}}}$$

$$W = \frac{(|Y|^2-|\bar{Y}|^2)+2iY\bar{Y}\sin(\varphi-\bar{\varphi})}{|Ye^{i\varphi}+\bar{Y}e^{i\bar{\varphi}}|^2}$$

Then if $\varphi \neq \bar{\varphi}$ or $|Y| \neq |\bar{Y}|$ (CP violation) then $W \neq 0$. If $|Y| \neq |\bar{Y}|$ (CPT violation) then $\mathrm{Re}W \neq 0$.

APPENDIX IV - THE NEGATIVE PION BEAM

The K^{o}'s used in this experiment were produced by the interaction of a negative pion beam with the brass targets in the Production-Decay Region. The negative pion beam was produced at zero degrees by the interaction of the circulating Bevatron proton beam with an internal target. After the pi-minus beam was bent out of the Bevatron by the Bevatron magnetic field, the pions passed through the first quadrupole focusing magnet set Q1A and Q1B (see Figure 25). This set produced a focus at the collimator. The bending magnet, M1 in front of the collimator, distributed the pions horizontally according to their momenta. The slits of the collimator were set to pass pions with a momenta of $2.85 \pm .03$ GeV/c. Next the pions passed through the bending magnet M2 and the quadrupole focusing magnets Q2A and Q2B which were designed in such a way as to undo the horizontal momentum spread caused by M1 and create a focus in the Production-Decay Region half way between the two targets. The combined bend of M1 and M2 was 17^{o}. The quadrupole magnet Q3 was designed to compensate for the verticle focusing effects of the Bevatron fringe field.

Distributed along the pion beam were various scintillation counters (S1, S2, S3, S4 and S4V) for monitoring the beam. S1 and S2 were 3"x1-1/2" scintillations set directly in back of the collimator and overlapped in such a way as to define an "electronic aperture" for the beam. These counters were used as a beam monitor by the Bevatron operators. S3 was a 3"x3"x1/4" counter that helped remove beam particles that scattered off the walls of the beam tube and Q3. The combination of

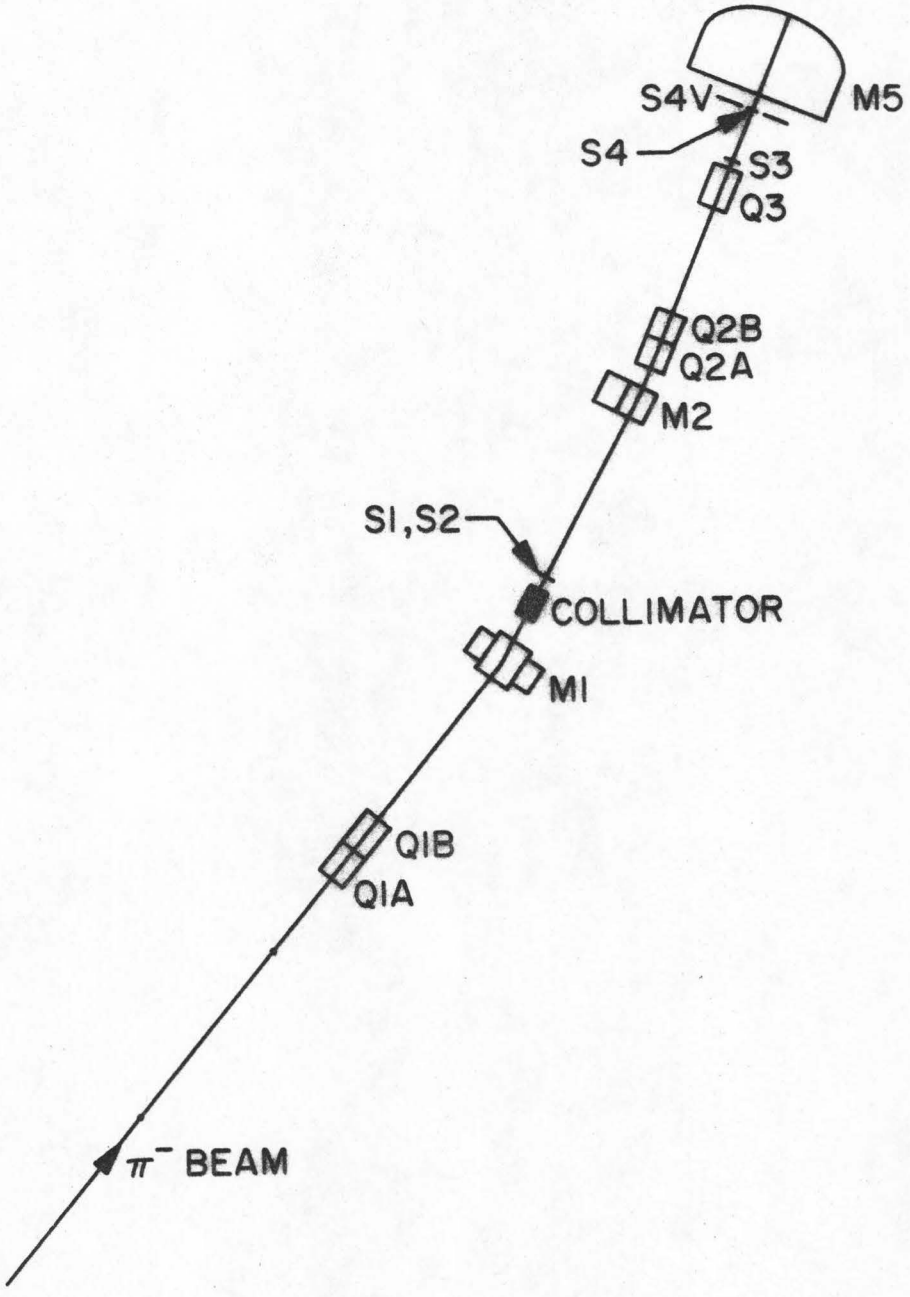

Figure 25 - The Pion Beam.

S4 and S4V narrowed the beam diameter to .8" at the front of the Production-Decay Region. S4 was a .8" diameter scintillator 1/4" thick which was positioned directly in front of a .9" diameter hole in S4V. Except for the .9" diameter hole, S4V covered the entire front of the Production-Decay Region thus vetoing stray beam pions (S4V was .4" thick). Thus an acceptable beam pion had to strike S1, S2, S3, and S4 and fail to hit S4V.

The electronics for monitoring these counters started with RCA 7850 phototubes. The last few dynodes of these tubes were connected to a capacitor bank to help them handle the high counting rates. The fast logic which these tubes were connected to is shown in Figure 26. The logic modules in this figure are described in Appendix VII.

This beam spectrometer produced 3×10^5 useful negative pions on the targets in the Production-Decay Region for every 10^{12} protons that struck the internal target during a typical Bevatron pulse. This beam intensity produced extra beam tracks in about 50% of the pictures that were taken by the apparatus. These extra beam tracks complicated the scanning of both the Production-Decay Region and the Shower Region. Therefore it was undesirable to run at beam rates in excess of 3×10^5 pions per pulse.

Because there was no electro-static separator in the beam, all negative semi-stable particles produced on the internal target at the right momentum could come down the beam tube. These include e^-, K^- and the desired π^-. The electrons are not a serious problem because they will necessarily produce a veto in the target veto counter. The K^- particles, however, can charge exchange in the brass target and

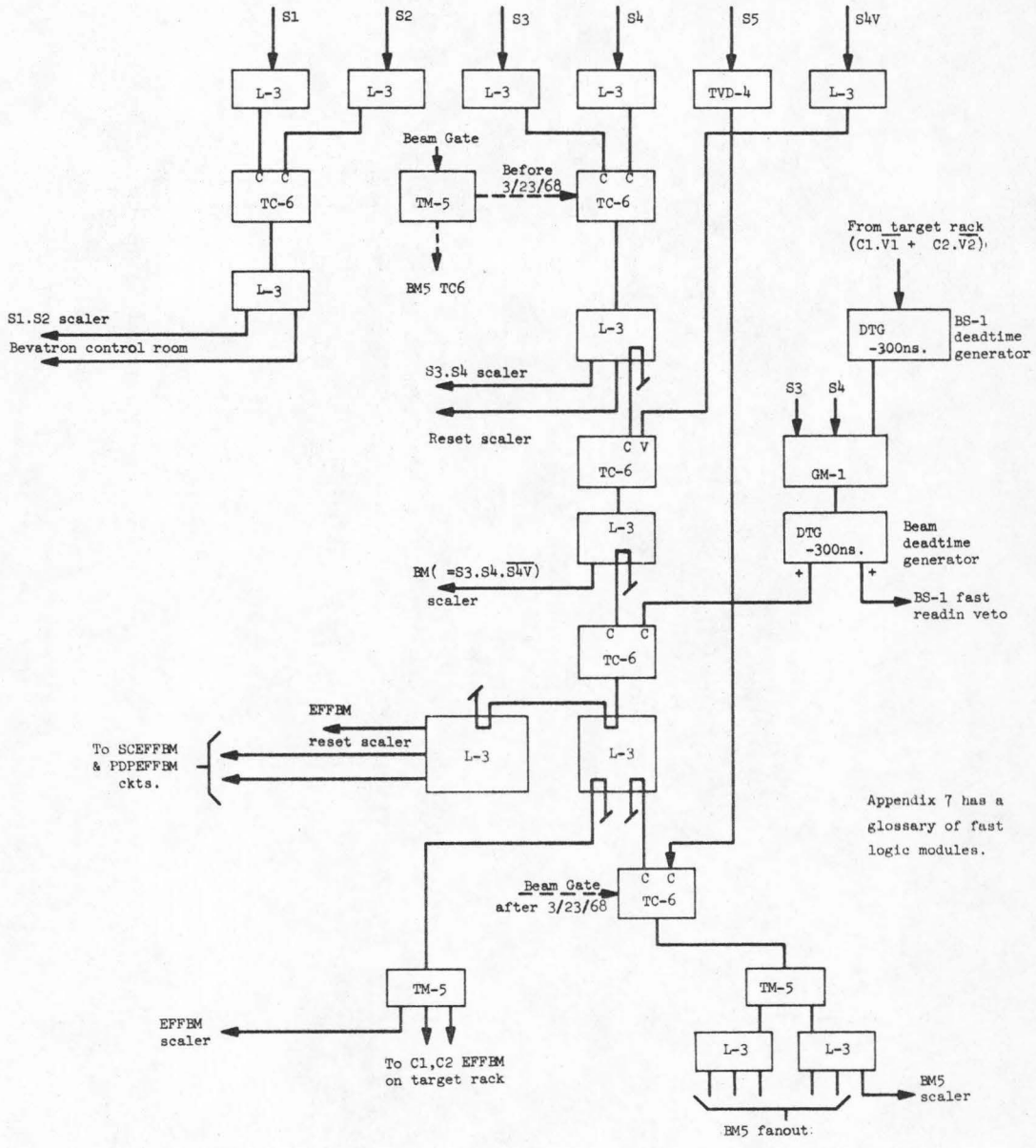

Figure 26 - Fast Beam Logic.

produce $\overline{K}^0$'s. For the Ke_3 experiment this could be a serious problem, but for this experiment the effect of the time distribution is not serious. In Chapter IV this background is dealt with in detail. In order to know how many K^-'s there were in the beam, a 10 atmosphere SF_6 Cerenkov counter was placed in the beam. Analysis of its pulses and time of flight information from the beam counters determined the K^- contamination to be $(.1 \pm .05)\%$.

APPENDIX V - TARGETS AND TARGET COUNTERS

In order to maximize K^o production the targets in this experiment were made of brass. If a hydrogen target had been used there would have been the possibility* of completely reconstructing the kinematics and thus knowing the proper time for each event. However, statistics have proved to be the most serious limit on the accuracy of this experiment** and the Ke_3 experiment so the choice of a heavy target material was best.

Before the experiment was run, various materials were tried as targets. The apparatus was set to trigger on two-pion events (calibration run trigger). The trigger rates and the number of vees appearing in the Production-Decay Region are graphed in Figure 27. Tungsten, brass, and aluminum produced equivalent numbers of vees. Tungsten was rejected because the multiple scattering of the beam in the first target seriously reduced its illumination of the second target. Aluminum was rejected because it didn't convert (and therefore veto) enough of its internally generated γ-rays. These γ-rays lead to an excessive Ke_3 trigger rate from their conversion in the spark chamber and counter (S5) material in the Production-Decay Region. Gamma rays escaping from the target (without converting and vetoing) also produce background for this experiment when they occur in coincidence with a vee. Therefore, in

---

*This would only be possible if the Λ were observed to decay as well, which would lower the overall efficiency.

**Error in the knowledge of the proper time of each event effects the decay distribution by less than 1%.

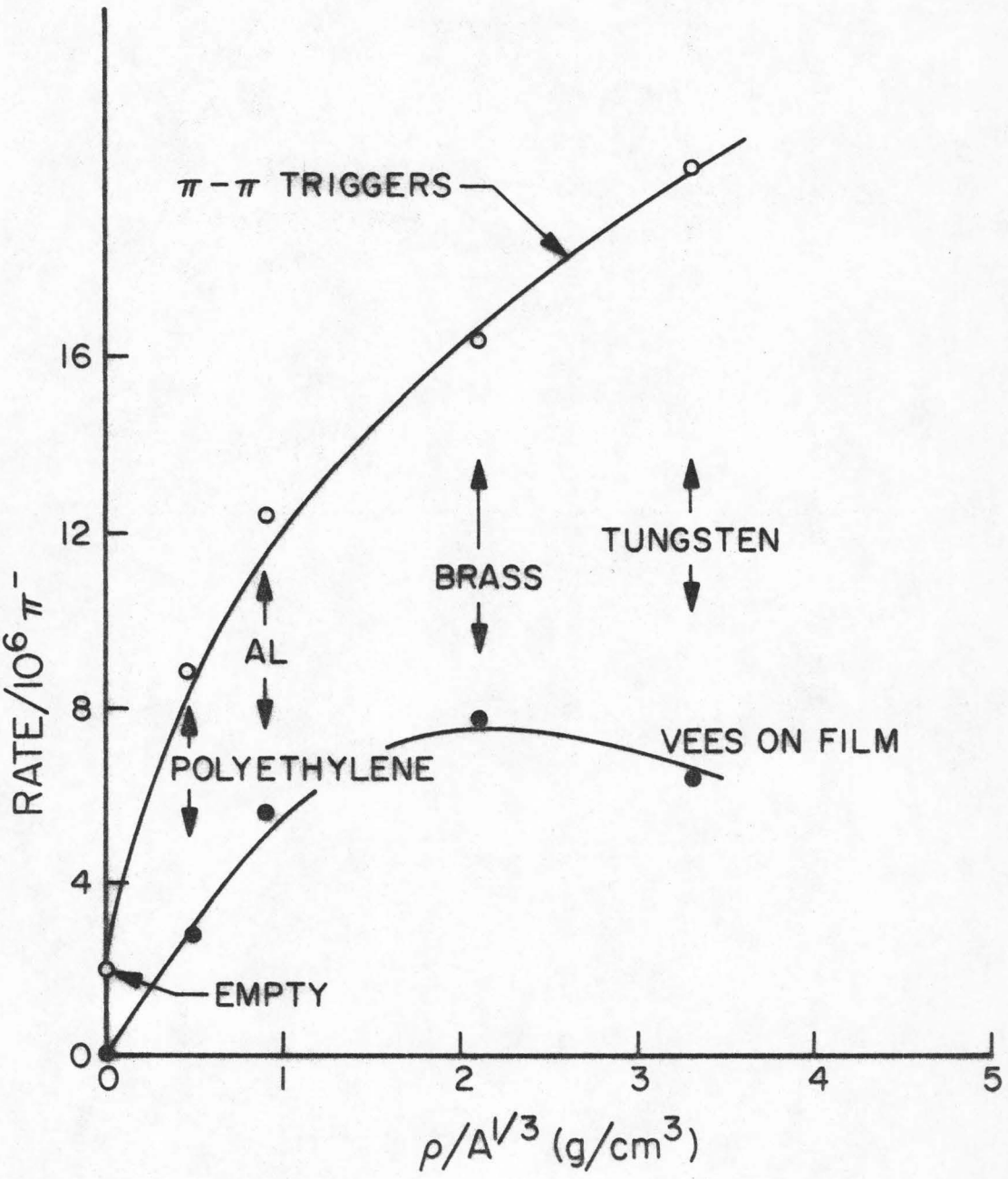

Figure 27 - Vee production with different target materials.

order to minimize the γ-ray induced background and to maximize the trigger rate from both targets, brass was chosen as the best material. However, to further reduce the γ-ray background a .1" (1/2 radiation length) thick lead disk was placed directly in back of each target.

The dimensions and locations of the two targets are shown in Figure 2. The brass cylinders were chosen to be 1.2" (3 cm) long. Because the longitudinal production point in the target is not known, an error in the proper time which is proportional to the length of the target is induced. With this target length the error induced on the proper time by the production point error is comparable to the error in the proper time caused by the K^o momentum error at 1/2 a K_S life time. Therefore, for proper times greater than 1/2 a K_S lifetime the effect of the production point error is small compared to the effect from the K^o momentum error (.38 GeV/c). It should also be remarked that the production point error (± .4") is somewhat less than the decay point error which for the $K \rightarrow 3\pi$ events is ± .5". Thus the target length was suitably chosen in light of the other errors in this experiment.

The diameters of the targets were important for other reasons. The first target was chosen to be larger than the beam (1.26" in diameter versus .8" for the beam) in order to guarantee that all the beams hit the target. The second target was chosen to be smaller (.75" in diameter) in order to minimize it's shadowing effect on events originating in the first target. Only a third of the beam hit the second target largely because of multiple scattering in the brass of the first target.

Directly in front of each target were the target coincidence counters (C_1,C_2). These counters detected the beam pion entering the

target. Directly in back of each target were veto counters (V_1,V_2). These vetoed the event if the beam pion did not interact or if it's interaction produced forward charged secondaries. These veto counters would also veto the event if a γ-ray converted in the brass or in the 1/2 radiation length of lead. The veto counters were centered on the brass targets by a pin which penetrated half way into the counter. This required that the veto pulse height requirement be set low in order to prevent veto failures.

Where the light pipes to these counters passed through the Production-Decay Region they were air light pipes. Outside this region, 1" diameter lucite light pipes completed the path to RCA 7850 photo tubes. These tubes were located as far as possible from the fringe field of the Momentum Spectrometer magnet (M5). The last few dynodes of these photo tubes were connected to capacitors to allow for a high counting rate. The efficiency of the counters was in excess of 99%.

The fast logic which monitored these counters is shown in Figure 28. If the coincidence counter (C) fired without the veto counter (V) firing in either target (1 or 2) then the trigger requirement "TARG" is generated. The exception to this is as follows. If an interaction occurs in the first target with more than one charged forward secondary then the second target cannot generate the "TARG" requirement. This occurs because V1 is connected to veto the C_2 signal through a pulse height discriminator (TVD-4) which fires if the signal from V1 exceeds 1 times minimum ionizing.

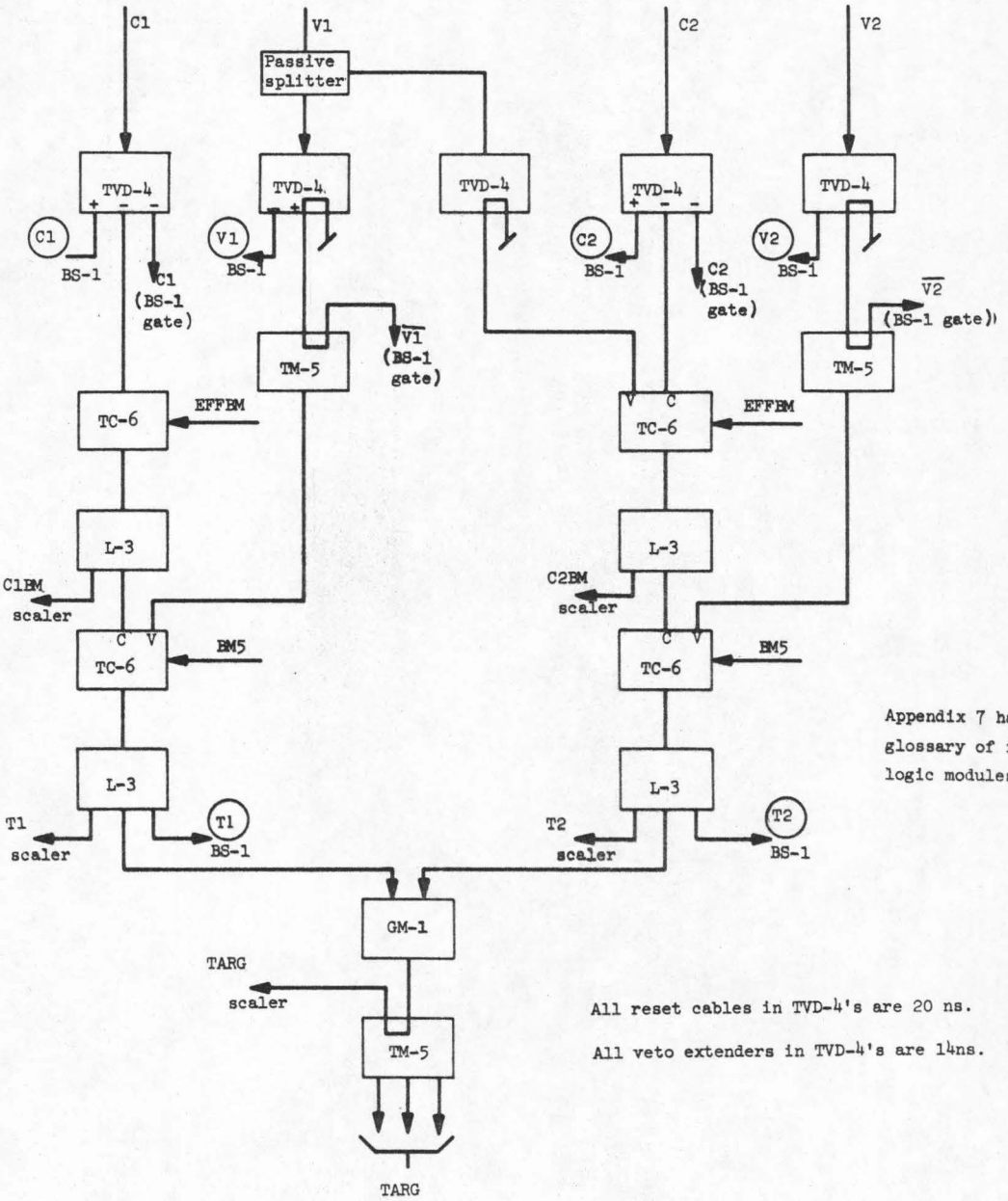

Figure 28 - Fast Target Logic.

APPENDIX VI - FREON CERENKOV COUNTER

For the purpose of detecting electrons, a 1-atmosphere, Freon 12, gas Cerenkov counter was located between counter S5 and the Multiples Hodoscope. At this Freon pressure the index of refraction is 1.00105 which corresponds to a threshold velocity of $B = 1/N = .99895$. This velocity corresponds to momenta of .011 GeV/c for electrons, 2.29 GeV/c for muons, and 3.02 GeV/c for pions. The cone angle for the Cerenkov radiation was $\theta_c = \sqrt{2(N-1)} = .046$ radians or about 3^o.

The Cerenkov counter is sketched in Figure 29. The front and rear walls (perpendicular to the beam line) were 3/4" aluminum and the other walls were 1/4" aluminum. The front wall had two holes for light pipes at the top left and right extremities and one hole for the free passage of the secondaries from the reactions in the Production-Decay Region. This window was geometrically the sum of a 7"x17" rectangle and two half circles 7" in diameter. Its extreme dimensions were then 7" high and 24" wide. The rear window had the same shape but with extreme dimensions of 16" high and 50" wide. The windows were covered with black Mylar .02" thick. The total box dimensions were 18" high, 60" wide, and 35" deep (parallel to the beam line).

There were two sets of optics and photo tubes in this counter. Each set covered one side of the counter and was symmetrically located about the beam line. The first step in the optics was an 1/8" thick plexiglass mirror which reflected the Cerenkov light into its light pipe. The mirrors in each set were parabolic and were mounted in such a way as to be adjustable from outside the box. The light pipes consisted of

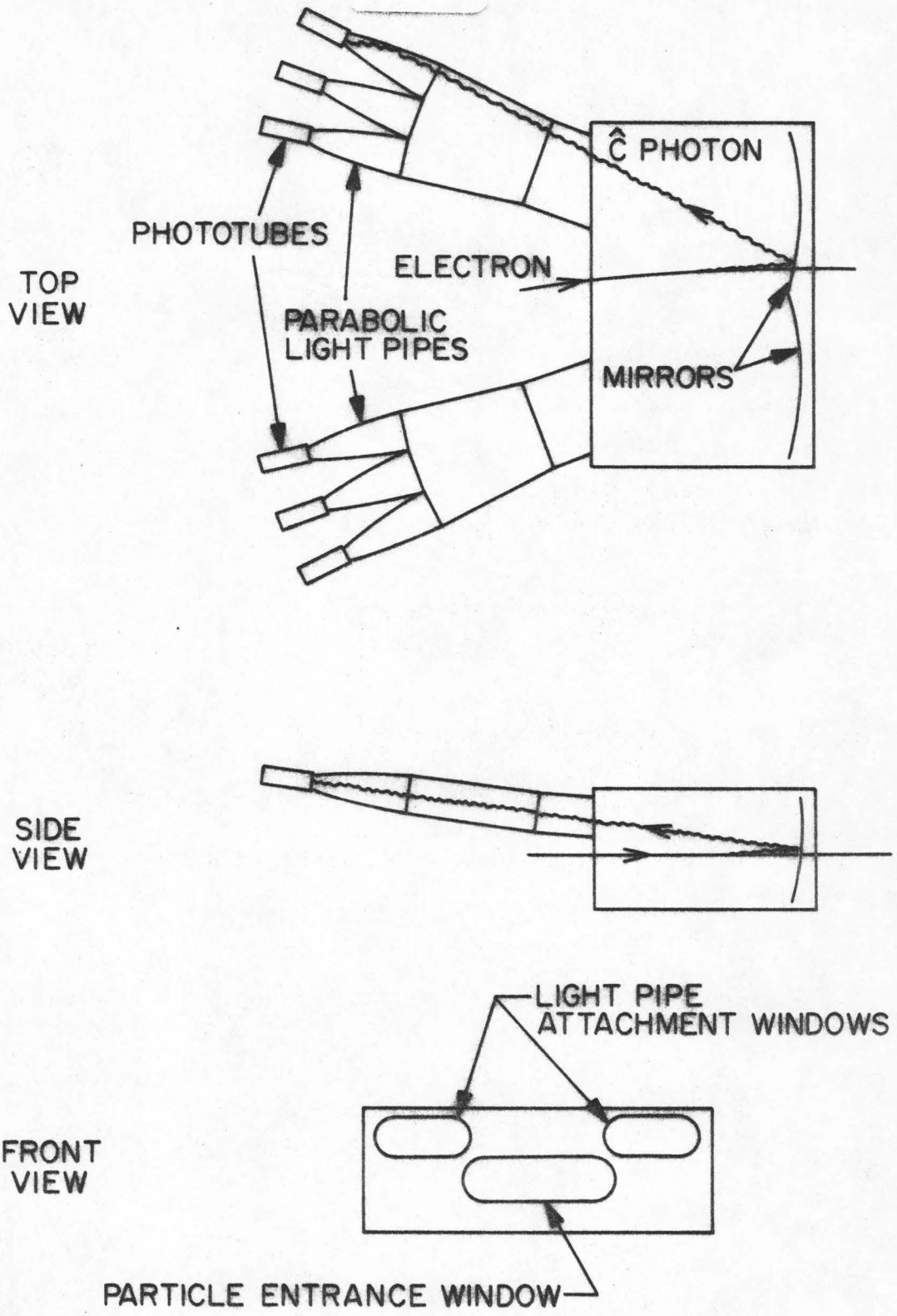

Figure 29 - Cerenkov Counter.

a non-converging section which branched into three parabolic sections. A photo tube was located at the focus of each parabola (6 tubes total). The parabolas were made by spinning a form (synthetic fibers and epoxy construction) of approximately the right shape at a determined velocity and then pouring epoxy into it. The epoxy then formed a parabola in balancing the centrifugal force against gravity. The parameters of the parabola were obtained by optimization in a light ray tracing computer program.

The 6 photo tubes in this counter were RCA 8575 tubes with a photo cathode efficiency of 28%. Each tube had a small piece of scintillator with a C_S 137 source glued on the side of the photo cathode. When the counter was tested in a 1 GeV electron beam from the Caltech Synchrotron, it was possible to get all the light from the electrons to shine on one tube at a time. The gains were adjusted so that the pulses from each were equal. The ratios of the pulses from the C_S 137 sources were then noted. By adjusting the dynode voltages during the experiment so as to maintain these source ratios the gains of the photo tubes were kept equal. These adjustments had to be made every time the M-5 magnetic field was reversed. This was despite the fact that the tubes were located as far from the magnet as possible and were shielded by 1/2" soft iron cylinders. The tests with the 1 GeV electrons also demonstrated that the pulse height distributions under optimal conditions corresponded to a Poisson distribution with M = 9 (9 photo electrons on the average). The detection efficiency for electrons is estimated to be 97%.

The electronics for the photo tubes is diagrammed in Figure 30. First the pulses from the three tubes on each side were added together

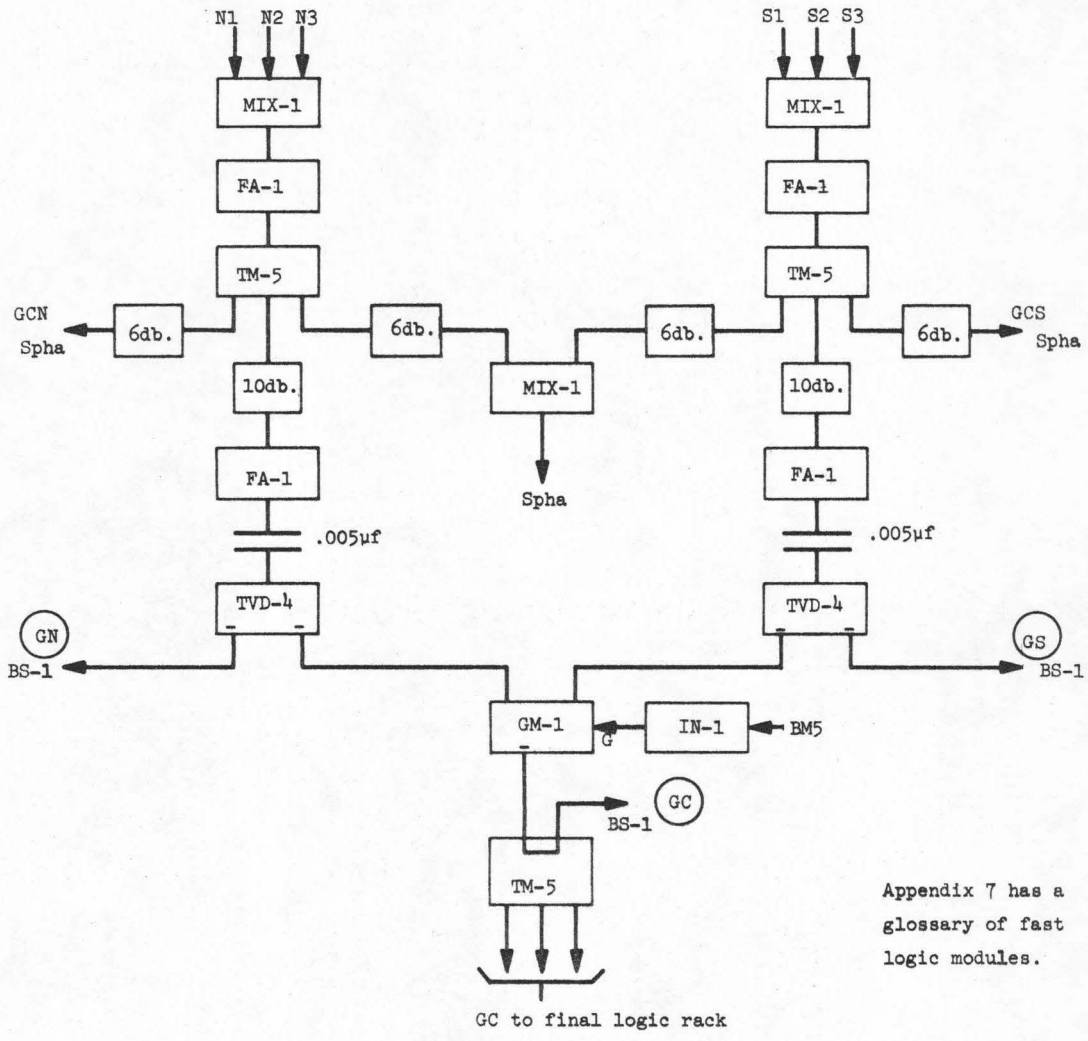

Figure 30 - Cerenkov Counter Fast Logic.

(MIX-1). Then these two sums (from each side) were amplified (FA-1). The amplified pulses were split and put to various uses. They were individually analyzed in the SPHA pulse height analyzers. They were summed and then the sum was fed to a SPHA for pulse height analysis. These three pulse heights (the sum and the two individual ones) were recorded for events fulfilling certain logic requirements. Finally these two signals were fed through a second amplifier into two discriminators (TVP-4) which were set at a very low bias (just above the noise). The outputs of the discriminators were recorded in the BS-1 buffer. They were also combined together with the beam signal (BM5) in the GM-1 so that if either discriminator produced a signal in coincidence with an incoming beam particle then the logic bit GC (gas counter) was produced. The GC signal was both recorded in the BS-1 and used in the fast logic as the signature of an electron in the gas counter.

APPENDIX VII- FAST ELECTRONICS AND TRIGGER LOGIC

The fast electronics used in this experiment consisted of modules which were built at Caltech and are described in CTSL Internal Report Number 31. Brief descriptions of the various types of modules are listed below:

FA-1 Fast DC coupled amplifier with a gain of 10 and a rise time of 2.3 NS.

TVD-4 Fast DC coupled discriminator with output rise and fall times of 2 NS. The input requirement could vary from -.05 to -1.0 volts.

L-3 DC coupled limiter with a rise time of 2 NS. It is often used to shape pulses for the TC-6 module.

TM-5 Fast DC coupled multiplexer for combining digital signals.

TC-6 Coincidence-anticoincidence circuit with four channels and a 2 NS time resolution.

GM-1 Gated mixer.

MIX-1 Mixer.

IN-1 Inverter.

DLPS-1 Delay line pulse shaper.

DTG-1 Dead time generator.

The counters in this experiment were organized into six groups. Each group had its own rack of electronics which generated a number of logic signals for use in the final trigger logic. These groups are listed below:

Group	Function	Appendix	Figure
Beam	Determines presence of π^- and S5 pulse and gates all the electronics.	IV	26
TARG	Biases for neutral production in the targets.	V	28
GC	Detects electrons.	VI	30
MH	Detects two particles through the MH.	XII	41
RH	Detects two particles through the RH.	XII	42
SH	Detects 3 times minimum pulse on either side of the SH counters.	XII	43

The "Beam" signal was necessary for all the other signals to be generated. The MH rack generated MH and $\overline{MH}^*$. The signal MH required the two triggered counters to be separated by one counter and the $\overline{MH}^*$ did not. The RH rack generated the RH signal when there were two triggered counters and produced the NS signal when these counters were on opposite sides of the apparatus. A detailed summary of the logic requirements of each signal is shown in Table 12. The bar above certain signals means that it is used in veto.

The various signals from the TARG, GC, MH, and RH (Beam implicit) racks were combined to form the various apparatus trigger signals. The block diagram of the trigger rack is shown in Figure 31. The input signals (from MH, RH, etc.) were 10 NS wide so with the beam rate less than 5×10^5/sec the accidental rate was negligible. The PIE and PPG trigger signals ($K \rightarrow \pi$ ev and $K \rightarrow 3\pi$ respectively) were used simultaneously to trigger data runs. Before February 2, 1968 VEE was used to trigger the TAPE writing and the calibration runs ($K \rightarrow 2\pi$), and after February 2, 1968 VEEM was used for this.

*Indicates that the signal was scaled and logged.

BEAM	*S1·S2	=	used for beam tuning and as a
	S3·S4		control room monitor.
	BM	=	$S3 \cdot S4 \cdot \overline{S4V}$
	BEAMDT	=	300 ns. generated by $(C_1 \cdot \overline{V_1} + C_2 \cdot \overline{V_2})$
	*EFFBM	=	$BM \cdot \overline{BEAMDT}$
	*BM5	=	EFFBM·S5
TARGET	*C_1BM	=	C_1·EFFBM
	*C_2BM	=	C_2·EFFBM
	*T1	=	$C_1 \cdot \overline{V_1} \cdot BM5$
	*T2	=	$C_2 \cdot \overline{V_2} \cdot BM5$
	TARG	=	T1 + T2
	*GC	=	GCN + GCS
MH	MHG1	=	> 1 counter from MH
	MHG2	=	> 2 counters from MH
	MHAC	=	Adjacent MH counters fired
	*MH	=	$MHG1 \cdot \overline{MHG2} \cdot \overline{MHAC} \cdot BM5$
	MH*	=	$MHG1 \cdot \overline{MHG2} \cdot BM5$ (also called MHWOS)
RH	RHN	=	signal in RH 1-16
	RHS	=	signal in RH 17-32
	RHG1	=	> 1 counter in RH
	RHG2	=	> 2 counters in RH
	*RH	=	$RHG1 \cdot \overline{RHG2} \cdot BM5$
	*NS	=	RHN·RHS
SH	SHN	=	sum of North above TVD-4 threshold
	SHS	=	sum of South above TVD-4 threshold
	*SH	=	(SHN + SHS)·BM5
	*VEEM	=	TARG·MH*·RH
	*PPG	=	$VEEM \cdot SH \cdot NS \cdot \overline{GC}$
	*VEE	=	TARG·MH·RH
	PIPR	=	$VEE \cdot \overline{GC}$
	*PIE	=	VEE·GC
	*PDPEFFBEAM	=	$EFFBM \cdot (\overline{PDP\ dead\ time})$
	*S·C·EFFBEAM	=	$EFFBM \cdot (\overline{spark\ chamber\ dead\ time})$

TABLE 12 - Fast Logic Signals

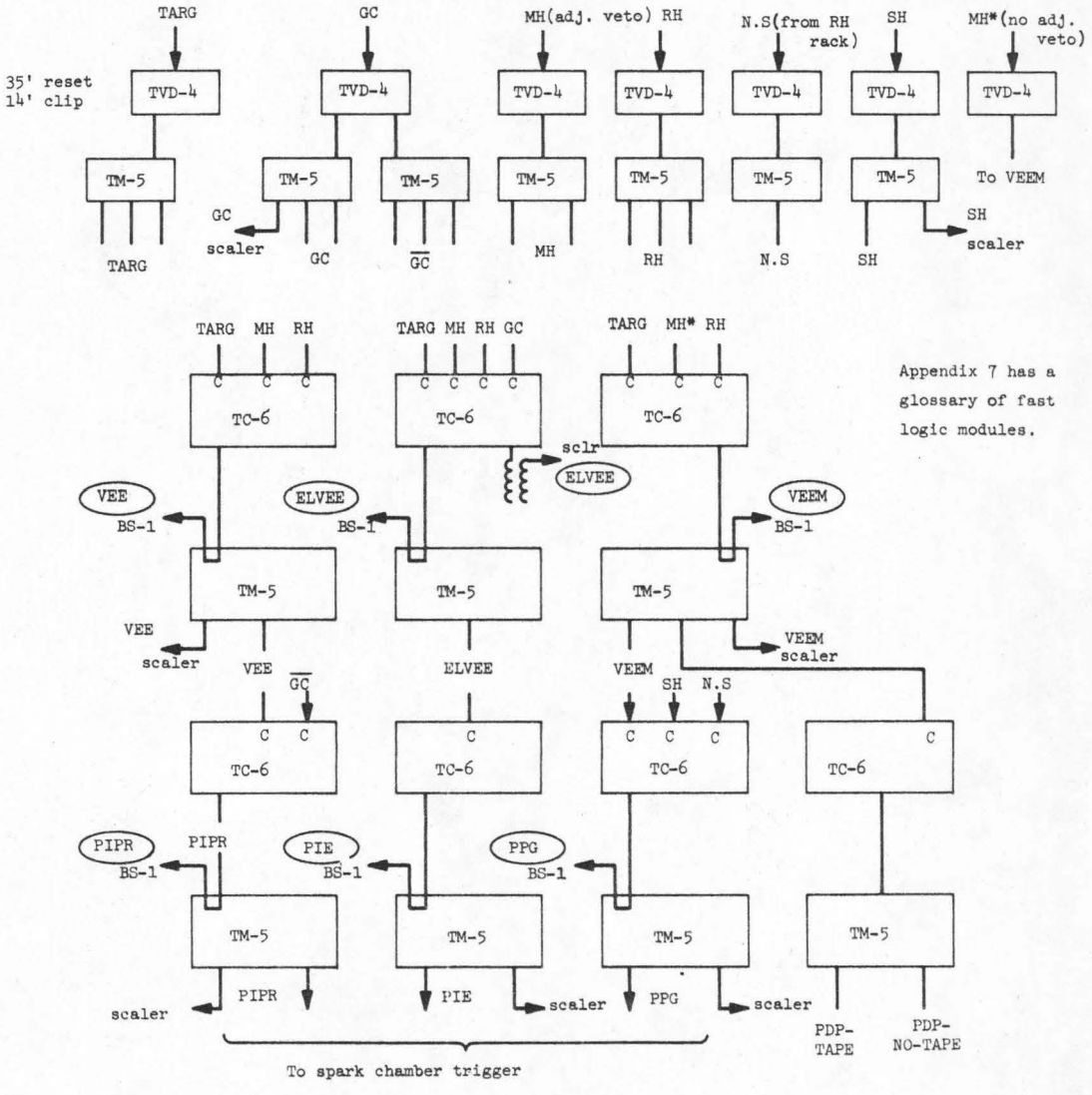

Figure 31 - Fast Trigger Logic.

APPENDIX VIII-TRACK MEASURING AND RECONSTRUCTION

The typical accepted event had two tracks which diverged from a vertex in the Production-Decay Region chambers and propagated through the Magnetic Spectrometer (three spark chambers) and into the Shower Chambers (see Figure 1). These tracks left strings of sparks (track segments) in each spark chamber they traversed that were recorded on film with a 90^{o} sereo optical system (see Appendix IX). These segments were measured with digitized protractor measuring machines in which the film image was projected onto a table on which the image was measured. The operator aligned a measuring line and a cross hair with the track segments. The machine then digitized the position of the cross hair and angular orientation of the line and recorded the information on a computer card. The measuring machines were accurate to $\pm$ .007 inches in position on the table (this corresponded to about .025 inches in the real space of the apparatus) and 2 milliradians in angle. The optical alignment and calibration of the measuring machines were checked periodically by measuring points on the projected image of an accurate cartesian grid.

On each measured frame the track segments were measured relative to a set of transfer fiducials that were flashed for each event. These transfer fiducials set the magnification, the position, and the orientation of each frame. The position of each spark chamber image was determined relative to the transfer fiducials by periodically measuring the transfer fiducials and the full fiducials which were flashed once per beam pulse. The full fiducials were accurately surveyed in the apparatus coordinate system. They consisted of electro-luminescent

strips which were notched every four inches. There was one full fiducial strip per spark chamber image. The average of ten full fiducial measurements was used in the analysis of each measured event. The full fiducial measurements were distributed over a range of about 10,000 serial numbers. Movements of the optical systems (changes in the positions of the transfer fiducials relative to the full fiducials) occurred at the level of 1/30" (real space) per 50,000 serial numbers. Thus the positions and orientations of the tracks were measured relative to the full fiducials (accurately surveyed) through the intermediary transfer fiducials.

An example of a Production-Decay Region data frame is shown in Figure 32a. The numbers are the order in which the various objects were measured. Numbers 1, 2, 5, 6, 7 and 8 are transfer fiducials whose positions are digitized. Numbers 3 and 4 are the beam tracks whose positions and angles are digitized in both views (elevation and plan views, respectively). Measurements 9, 10, 11, and 12 are the digitizations of the two tracks in the two views (angles and positions are measured). Figure 32b is a full fiducial frame. Measurements 9 through 16 are full fiducial points whose positions were digitized. Measurements 1 to 8 are the same as on the data frame.

Once the track segments were digitized the measurements were analyzed by a program which constructed track segments in three space (of the apparatus) from the two space projections of the two views. Optic axis corrections and distortion corrections were made as described in Appendix IX. The nominal measurement accuracies (after corrections) for each view of each chamber are listed below (these are the errors used in the reconstruction programs).

(a)

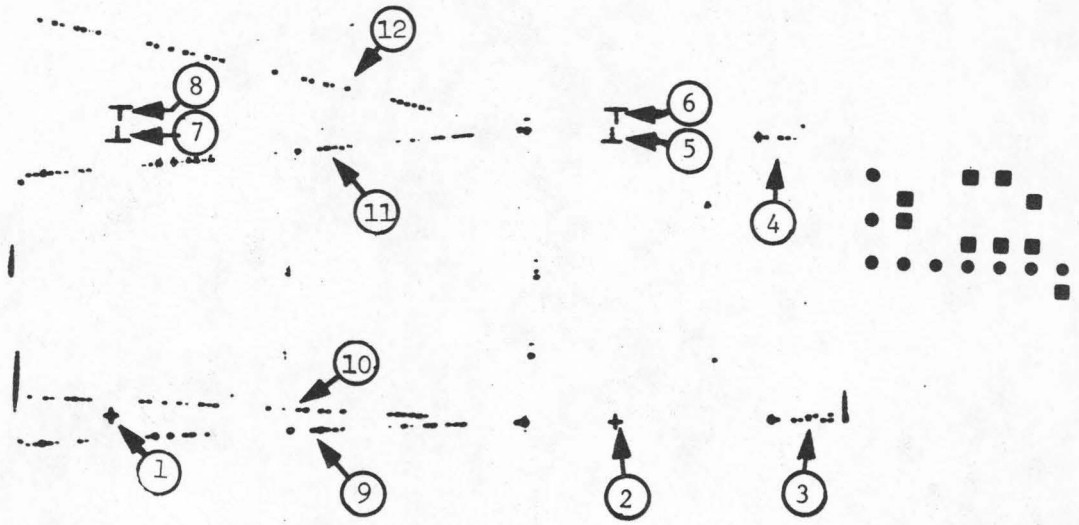

(b)

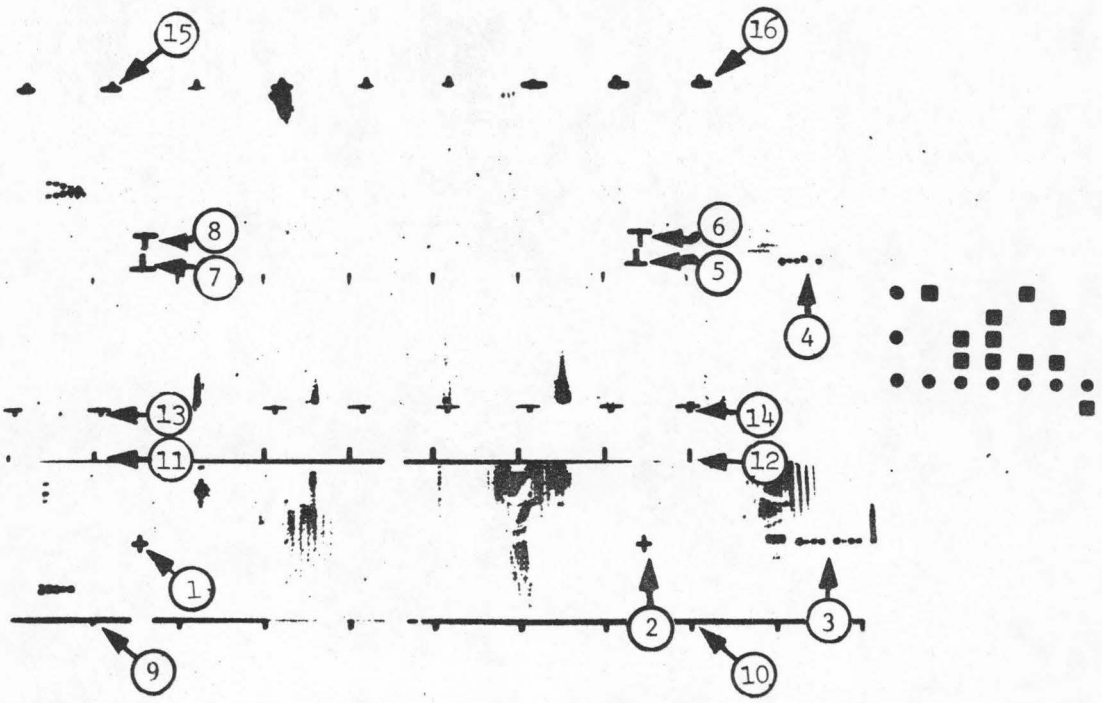

Figure 32 - A) Typical Production-Decay Region data frame.
B) Typical Production-Decay Region full fiducial frame.
(The numbers are the order of measurement of the various objects in A and B.)

Chamber		Elevation View	Plan View
Production-Decay		.08", 6Mr	.11", 6Mr
Momentum Spectrometer	FM	.03",17Mr	.03",500Mr
	MM	.06",17Mr	.06",500Mr
	RM	.03",17Mr	.03",17Mr
Shower		.20",17Mr	.20",17Mr

The angular error of 500Mr assigned to the FM and the MM chambers was a technique for removing these angular measurements from the fitting procedure. These measured angles were found to vary systematically (± 35 Mr) with the magnetic field so they were effectively dropped as a constraint by applying this large error (500 Mr). The above errors were determined both from distortion grid measurements and from measurements of "straight-through" tracks (no magnetic field). The measurements of the straight-through tracks also aided in checking the relative alignment of the spark chambers (independently of the survey).

As described in Chapter III the measuring of events occurred in two steps. First the track segments in the Production-Decay Region and the Shower Region were measured and preliminary trajectories were reconstructed. These preliminary trajectories were then used to tell the measurer where to look for tracks in the Momentum Spectrometer Chambers. The measurer was instructed to measure everything within 4" (in apparatus space) of where he was told to look. The closest measurement to the preliminary trajectory was then used as the measured track segment if it fell within certain limits of the first fitted trajectory. These limits were:

Chamber	Elevation View	Plan View
FM	± 1"	± 1"
MM	± 1"	± 2"
RM	± 1"	± 2"

If an acceptable measurement could not be found for a trajectory in a certain chamber then that track segment was not used in the final fit. The acceptable measurements were then used in a second fit. The χ^2 per degree of freedom for each measurement relative to this second fit was calculated. If the worst χ^2/d.f. was greater than 18, then that measurement was dropped and a third fit performed. This process was repeated until either there was no measurement with a χ^2/d.f. $>$ 18 or all droppable measurements had been dropped. Dropping the Production-Decay Region measurement was not permitted and dropping both the RM measurement and the Shower measurement was not permitted. In addition, the fit constrained the two tracks to form a vertex in the Production-Decay Region.

The fitted momenta for each track were then used to calculate invariant masses for the two charged secondaries under various assumptions about the nature of the secondaries (whether they were pions, muons, electrons, or protons). This information along with bookkeeping information, scintillation counter information (from the experiment data tape), trajectory parameters and error matrices were then recorded in 1000 word records on magnetic tape.

APPENDIX IX - THE OPTICAL SPARK CHAMBERS

The spark chambers in this experiment were arranged in three groups serving three functions. These groups are: the Production-Decay Chambers, the Momentum Spectrometer Chambers, and the Shower Chambers (see Figure 1). The Production-Decay Chambers were used for observing the K^o decay position distributions. These chambers were scanned for "vees" and measured to determine the vertex position of the vee and the positions and orientations of the two charged secondaries. The Momentum Spectrometer Chambers were measured to determine angles and accurate positions for the two charged secondaries at three points (entrance, middle and exit) in the magnetic spectrometer. These measurements were then used for accurate momentum ($\pm$ 7%) and trajectory reconstruction. The Shower Chambers were scanned for gamma ray showers and two non-electron tracks. The measurements of the two tracks were also used in the momentum reconstruction.

Each of the above groups of chambers had its own optics system and 35 mm double frame Flight Research Camera model 207. The track segments on the film were measured relative to a set of "transfer" fiducials which were flashed for every frame. The positions of the transfer fiducials were measured relative to the "full" fiducials which were flashed for every beam pulse. The positions of the "full" fiducial in real space were known to 1/32" from the result of an apparatus survey (see Appendix VIII).

The gas system for the chambers consisted of a continuously circulating and purified 90/10 Ne-He mixture. The gas was purified at liquid nitrogen temperatures by a charcoal absorption unit.

The position of the optic axis (the optical path to the camera which is parallel to one of the axes of the experimental coordinate system) for each view of all the chambers was determined to an accuracy of 1/2" by two techniques (path length $\approx$ 300"). The first technique consisted of replacing the camera by a laser. The laser beam was reflected off a mirror mounted parallel to the "beam line" (the center line of the apparatus) and oriented either exactly ($\pm$ .001 radians) vertical or horizontal by a precision level. When the laser beam was pointed along the optic axis, it was reflected back on itself by this mirror. The second technique consisted of photographing accurately surveyed grids placed at various distances from the camera. When the grid is moved along an axis parallel to one of the experimental coordinates (horizontal or vertical) the point on the grid corresponding to the optic axis does not move on the film. The two techniques agreed to the stated accuracy of $\pm$ 1/2". This error corresponds to a track measurement error of about 1/32" under the most extreme circumstances.

The optical grids that were used in determining the optic axis were also used to map out optical distortions in the Production-Decay Region and the first two chambers of the Momentum Spectrometer Region. The Production-Decay Region distortions were of the order of .15" in space and the Momentum Spectrometer Region distortions were of the order of .075". These distortions arose primarily from warping in the mirrors of the optical system. These mirrors consisted of 1" and 3" aluminum

hexel sandwiched and epoxied between a 1/4" glass backing and a 1/4" glass front surfaced (aluminum) mirror. Many of them were old and had warped.

The sweep fields for the chambers were typically 90 V. This resulted in a 50% efficiency live time of 1 μsec. The chambers fired 400 μsec after the trigger event occurred. At the operating beam rate of 2×10^5 pions per pulse this resulted in extra beam tracks in about half the pictures.

The above discussion deals with characteristics that were shared by all the chambers. The following sections describe the three regions of the apparatus individually.

Production-Decay Chambers

The Production-Decay Region of the apparatus is diagrammed in Figure 2. There were 7 spark chamber modules distributed throughout this region. There were 6 modules behind the first target and 2 behind the second target. One of the modules in front of the first target was for observing the incoming beam pion. Each module was 4" thick and there was a 2" gap between modules. The plates of the module were approximately perpendicular to the beam (they were tilted slightly so that the optical path to the camera was parallel to the plates) and were 8" high and 18" wide. Each module had 11, 1/4" gaps. The plates were removable and each plate consisted of .0015" crinkled aluminum foil sandwiched between two sheets of .0015" aluminum foil mounted on a brass wire loop that circumvented the decay region. Each module therefore presented .01 radiation lengths of material to particles traveling parallel to the beam line.

Each module was pulsed by a triggered spark gap which connected it to a 3.9 uf capacitor charged to 9KV. With this arrangement the two track efficiency was 99% for minimum ionizing tracks. Heavily ionizing nuclear fragments could degrade this efficiency, however.

The modules, which along with the targets were mounted on a removable cart, were viewed from a distance of 480" with an F4.5 lens (9" focal length) through 5 front surfaced aluminized mirrors. The wide aperture was used to obtain the high spark efficiency (99%). However, this produced a problem with aberrations that made the sparks appear quite wide (.1") in places (near the periphery of the frame). Because of geometric constraints the plan view image had to be split in half (down the beam line) and reassembled later in the optical system. This led to a "blind spot" in the optics of the plan view that ran the length of the Production-Decay Region. This blind spot was between 1/8" and 1/4" wide. For the purpose of monitoring this blind spot and the relative alignment of the two halves of the plan view, two "I" shaped transfer fiducials ran across the gap between the two halves of the plan view (they appeared as two "T"'s in each half). For events from the first target this blind spot did not seriously affect the scanning and measuring because it was very unlikely that a track could be obscured for its entire length.

After all the optical effects both on the measuring tables and in the apparatus were corrected for, the measuring accuracy in the plan view was $\pm$ .11" and in the elevation view it was $\pm$ .08". The angular accuracy in both views was $\pm$ .006 radians. It was found that the typical vertex for a $K \rightarrow 3\pi$ event could be reconstructed to an accuracy of $\pm$ .5" in

the beam direction. This is greater than for $K \rightarrow 2\pi$ events ($\pm$ .3") because the opening angles are smaller for $K \rightarrow 3\pi$ events.

The Momentum Spectrometer Chambers

In this part of the apparatus there were three groups of chambers: the front momentum chamber, the middle momentum chamber, and the rear momentum chambers. In all these chambers the plates were made from a sandwich of a 1/8" styrofoam sheet between two sheets of .0005" aluminum foil. The total mass that a particle traverses in these three sets of chambers is .007 gm/cm^2. These chambers were viewed through an F9.2 lens aperture (6" focal length). The rear momentum chambers were dimmed relative to the others by a filter which passed 1/4 of the light. The images for the rear chambers had to pass through fewer mirrors so that they were relatively too bright.

The front momentum chamber was located between counter S5 and the front window of the Cerenkov counter. It had 6, 1/4" gaps that were pulsed with 9 KV from a 3.9 uf capacitor. It was 8" high and 24" wide. The elevation view passed through 7 mirrors to the camera for a total path length of 382". The plan view passed through 5 mirrors to the camera for a path length of 375". The position resolution in the elevation view was $\pm$ .02" and the resolution in the plan view was $\pm$ .04". The angular resolution was $\pm$ .02 radians.

The middle momentum chamber was located just behind the Multiples Hodoscope and near the center of the magnet pole piece. It was 18" high and 60" wide and had 4, 3/8" gaps. It was pulsed by 2, 3.9 uf capacitors charged to 12 KV. A shorting gap which cut off the pulse shortly after it was initiated was included in the pulser electronics. This shorting gap

improved the multi-track efficiency of the chamber. The elevation view of this chamber passed through 7 mirrors to the camera with a path length of 361". The plan view passed through 5 mirrors with a path length of 414". The resolution in the elevation view was ± .03" in position and ± .02 radians in angle. The resolution in the plan view was ± .06" in position and ± .03 radians in angle.

The rear momentum chambers were located just in back of the exit to the magnet and just in front of the Rear Hodoscope. While the front momentum chamber and the middle momentum chamber were oriented perpendicular to the beam line, the two rear chambers were placed at a 16° angle from the perpendicular to the beam line. With this orientation the average particle trajectory through the magnet passed through these chambers at a perpendicular angle (see Figure 1). The two chambers were located on opposite sides of the center line of the apparatus (beam line) and overlapped by 6" at the center. Each had 6, 3/8" gaps. They were both 36" high and 60" wide. Each had its own pulsing unit, that delivered a 12 KV pulse from 3, 3.9 uf capacitors. Shorting gaps were included in the pulser electronics. The plan views for these chambers had to travel 366" through 3 mirrors to the camera. The position resolutions in this view were ± .03" and the angular resolutions were .015 radians. The elevation view for the rear momentum chamber on the north side (in front of Rear Hodoscope counters #1 to #16) had to pass through 5 mirrors and 420" to the camera. Its resolution was ± .04" in position and .02 radians in angle. The elevation view for the other chamber passed through 3 mirrors and 353" to the camera. Its resolution was ± .03" in position and ± .015 radians in angle.

The Shower Chambers

There were two sets of shower chambers which were located on opposite sides of the apparatus center line and which touched at the center line. They were both cocked at 16° from being perpendicular to the beam in the same way as the rear momentum chambers. Each of these two sets consisted of 3 chamber modules stacked in front of each other. Each module was 6" thick, 4' high and 6' wide, and had 6, 3/8" gaps and 9 plates. The plates were made of a sandwich of .02" Pb between 2, .02" sheets of Al. This gave each module a total of 1 radiation length and .065 collision length of material. The modules were individually pulsed by sets of 4, 3.9 uf capacitors charged to 12 KV. Shorting gaps were included in the pulsers. The first and the third modules were provided with prisms so that the camera (455" away) could see down the plates. The position resolution in the shower chambers was .2" and the angular resolution was .02 radians. The poor position resolution was due both to large distortions and a shaky optical system. The camera lens had a 6" focal length and an F12 aperture setting.

APPENDIX X - SMEARING OF THE TIME DISTRIBUTION

The proper times of the K^o decays in this experiment were determined by the following formula:

$$\tau = \frac{M}{p_o c}(\ell_D - \ell_p) = \frac{ML}{p_o c} \qquad (AX.1)$$

where ℓ_p is the production point, ℓ_D is the decay point, p_o is the K^o momentum, M is the mass of the K^o, and c is the velocity of light. The track measurements in the Production-Decay Region allow the reconstruction of ℓ_D to $\pm$ .5". Because the decays are three body decays and only two tracks are measured, ℓ_p had to be taken as the center of the target $\pm$ .4" (the target is 1.2" long). The quantity $(\frac{1}{p_o})$ was not measured for each event (again because of the partial reconstruction) but instead was taken as the mean inverse K^o momentum of the accepted events (determined in the Monte Carlo calculation). The effect of these three sources of error in τ on the time distribution are discussed below.

To examine the effect of the momentum uncertainty on the fitted decay distribution we note that this distribution is given by

$$G(L) = \frac{dN}{dL} = \int F(\frac{ML}{pc})\ \frac{M}{pc}\ \varepsilon(p,L)\rho(L)dp \qquad (AX.2)$$

where $F(\tau)$ is given by equation (1.4); $\rho(p)dp$ is the number of K^o's of momentum p produced in the target (see Figure 9); and $\varepsilon(p,L)$ is the acceptance of the apparatus for events of momentum p and decay length L. Expanding the time distribution in a Taylor series

$$F(\frac{ML}{p_o c}) = F(\frac{ML}{p_o c}) - F'(\frac{ML}{p_o c})\ \frac{ML}{p_o^2 c}\ (p-p_o) + \frac{1}{2}\left[(\frac{ML}{p_o^2 c})^2 F'' + \frac{2ML}{p_o^3 c}\ F'\right](p-p_o)^2 + \ldots \qquad (AX.3)$$

so that $G(L) = G_1(L) + G_2(L) + \ldots$ corresponds to the various terms in the series. Then

$$G_2(L) = -\frac{M^2 L}{p_o^2 c^2} F' \int \rho(p)\epsilon(p,L)\left(\frac{p-p_o}{p}\right)dp \ . \qquad \text{(AX.4)}$$

By choosing

$$p_o(L) = \frac{\int \rho(p)\epsilon(p,L)dp}{\int \frac{\rho(p)\epsilon(p,L)}{p}dp} \qquad \text{(AX.5)}$$

this term (G_2) vanishes and up to first order

$$G(L) = \frac{M}{p_o c} F\left(\frac{ML}{p_o c}\right)A(L) \qquad \text{(AX.6)}$$

where $A(L) = \int \rho(p)\epsilon(p,L)dp$ is the acceptance function of the decays (see Figure 12). Both $A(L)$ and $p_o(L)$ were determined in the Monte Carlo calculation described in Appendix XI. It was found that to $\pm$ 2% p_o was independent of L and was therefore taken to be a constant.

The relative error induced in the position distribution by the width of the K^o momentum distribution (representing G(L) by equation AX.6 instead of equation AX.2) is

$$\frac{G_3}{G} = \frac{1}{2}\left(\frac{\sigma_p}{p_o}\right)^2 \left[\frac{F''t^2 + 2F't}{F}\right] \qquad \text{(AX.7)}$$

where $t = \frac{ML}{p_o c}$ and σ_p is the width of the momentum spectrum of the accepted events. The term in brackets is zero at $t = 0$ and $t = \infty$, and is always less than 2 for $|W| < .5$ (the denominator can go singular for large W). From the Monte Carlo calculation p_o was 2.3 GeV/c and σ_p was .32 GeV/c so

$$\frac{G_3}{G} < \left(\frac{\sigma_p}{p_o}\right)^2 = .02$$

This error is completely negligible compared to the statistical error in G(L).

Next we consider the error in G(L) from the error in L. The error in L arises from the errors in ℓ_D and ℓ_p ($\pm.5$" and $\pm.4$") described at the beginning of this appendix. The error in L is $\sigma_L = .6$" when we combine the errors in ℓ_D and ℓ_p. Assuming that the errors are Gaussian the measured distribution (H(L)) is given by:

$$H(L) = \int_{-\infty}^{\infty} G(L') \frac{1}{\sigma_L}\sqrt{\frac{2}{\pi}}\, e^{-\frac{(L-L')^2}{2\sigma_L^2}}\, dL' \quad . \tag{AX.8}$$

If we expand G(L') in a Taylor series,

$$G(L) = G^o(L_o) + G'(L_o)(L-L_o) + \ldots \tag{AX.9}$$

and just keep the first two terms then the change in the position distribution divided by the magnitude is:

$$\frac{H(L)-G(L)}{G(L)} = \frac{G'(L)}{G(L)} \frac{1}{\sigma_L}\sqrt{\frac{2}{\pi}} \int_{-\infty}^{\infty} (L-L')e^{-\frac{(L-L')^2}{2\sigma_L^2}}\, dL' = \frac{G'}{G}\sigma_L\sqrt{\frac{2}{\pi}} \quad .$$

For $L = 0$, G'/G is maximal and is less than a fifth for $|W|$ less than a half. Putting in the value of σ_L we find that $\frac{\Delta G}{G} < 1/10$ in the worst case. This is well within the statistical error ($\pm 25\%$ is the error on the number of events in the first K_S lifetime) of the region where G'/G might be large.

APPENDIX XI - THE MONTE CARLO PROGRAM

The Monte Carlo calculations for this experiment are discussed extensively in Chapter IV. As stated there, it was first necessary to analyze $K_S \rightarrow 2\pi$ decays in order to determine the momentum and angular distributions of the K^o beam which emerged from the brass targets as a result of associated production (Equation 3.2) from a 3 GeV/c π^- beam. These distributions were unfolded from the data with the aid of a Monte Carlo calculation which determined the apparatus acceptance as a function of the K^o momentum and angle.

The Monte Carlo $K \rightarrow 2\pi$ decays were randomly generated in the center of mass (uniform c.m. angular distribution) and then Lorentz transformed into the laboratory frame using preselected K^o momenta and angles. The decay length was determined randomly from an exponential decay law using the known K_S lifetime. The decay secondaries were then traced through the magnetic field. If the tracks were found to pass through the magnet without striking the pole pieces, the yoke, or the coils, then the events were checked for the following requirements:

1) The decay vertex had to be in the fiducial volume of the Production-Decay Region.

2) Both tracks had to pass through an aperture at S5 of $\pm$ 8" horizontally (z) and $\pm$ 4" vertically (y).

3) One track had to hit S5.

4) Both tracks had to pass through the front window of the gas counter ($\pm$3.5" vertically).

5) Both tracks had to go through MH counters separated from each other by at least one counter.

6) Both tracks had to hit different RH counters.

7) Both tracks had to pass through the aperture defined by the shower counters.

The Monte Carlo events which satisfied the above requirements were recorded on magnetic tape for comparison with the data.

By comparing the successful Monte Carlo events to the $K \rightarrow 2\pi$ data the momentum and angular distributions of the K^o beam were determined (see Chapter IV). These distributions were then used in a new Monte Carlo $K \rightarrow 2\pi$ calculation in which the K^o momenta and angles were determined randomly (weighted with the above distributions). The accepted Monte Carlo events (from this second calculation) were then compared to the data directly. The K^o momentum and angular distribution are compared in Figure 10 and the decay length distributions are compared in Figure 11 (Chapter IV). The position distributions of the secondaries at the S5, MH, and RH apertures are compared in Figures 33 and 34 for T1 events. The only discrepancy is a slight depletion of tracks near the center of the plan view (Figure 34). This is probably caused by a tendency to lose tracks near the center of the shower chambers where the optics and the chambers are split into two halves (tracks would often cross each other here and get confused). Also this is the region in which extra beam tracks appear. These extra tracks could cause the rejection of an event by projecting into a triggered RH counter. The effect of this depletion on the vertex distribution in the Production-Decay Region was found to be negligible.

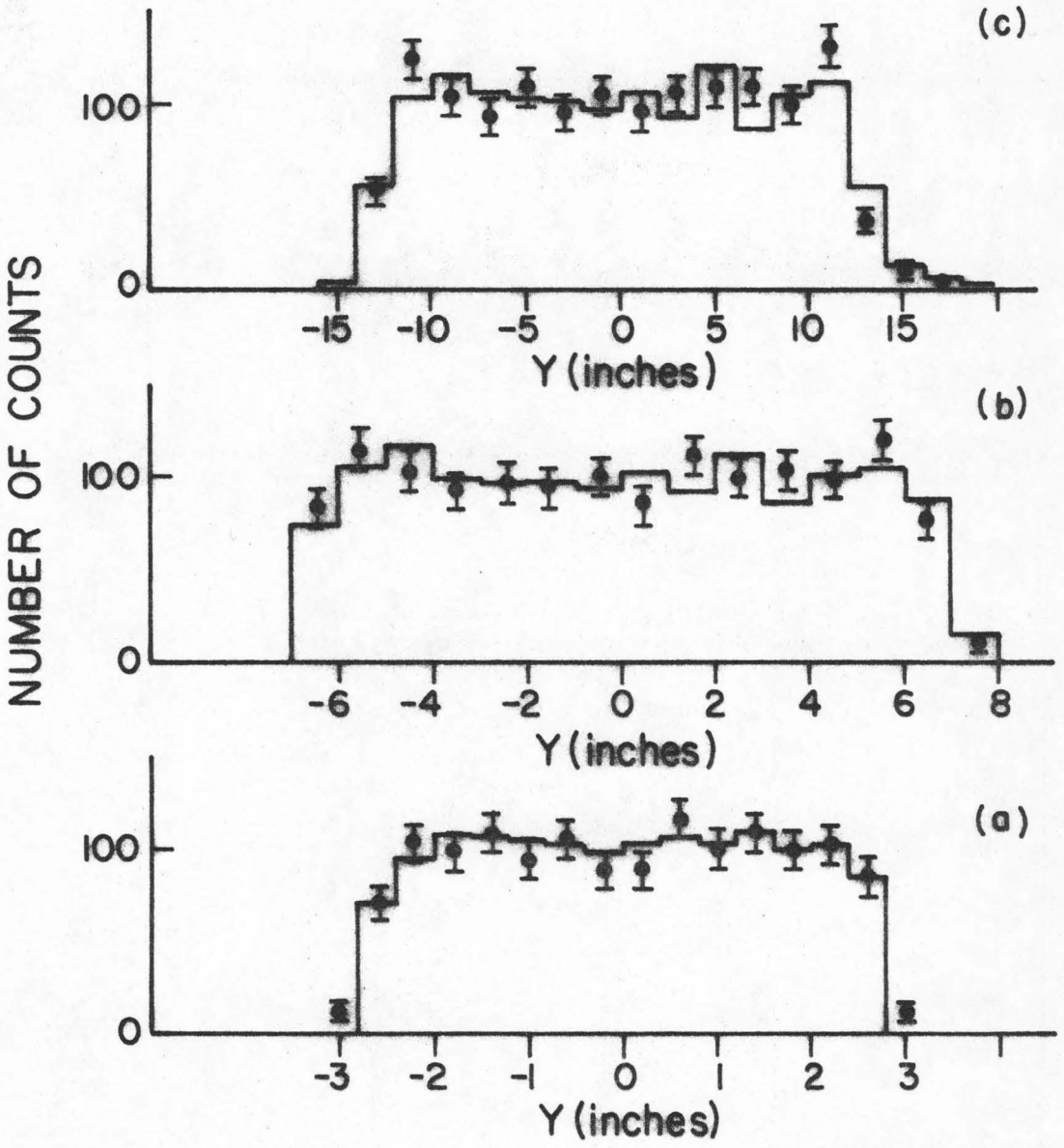

Figure 33 - Comparison of track density distributions between calibration run data (points) and Monte Carlo events in the elevation views at the (a) S5, (b) MH, and (c) RH apertures.

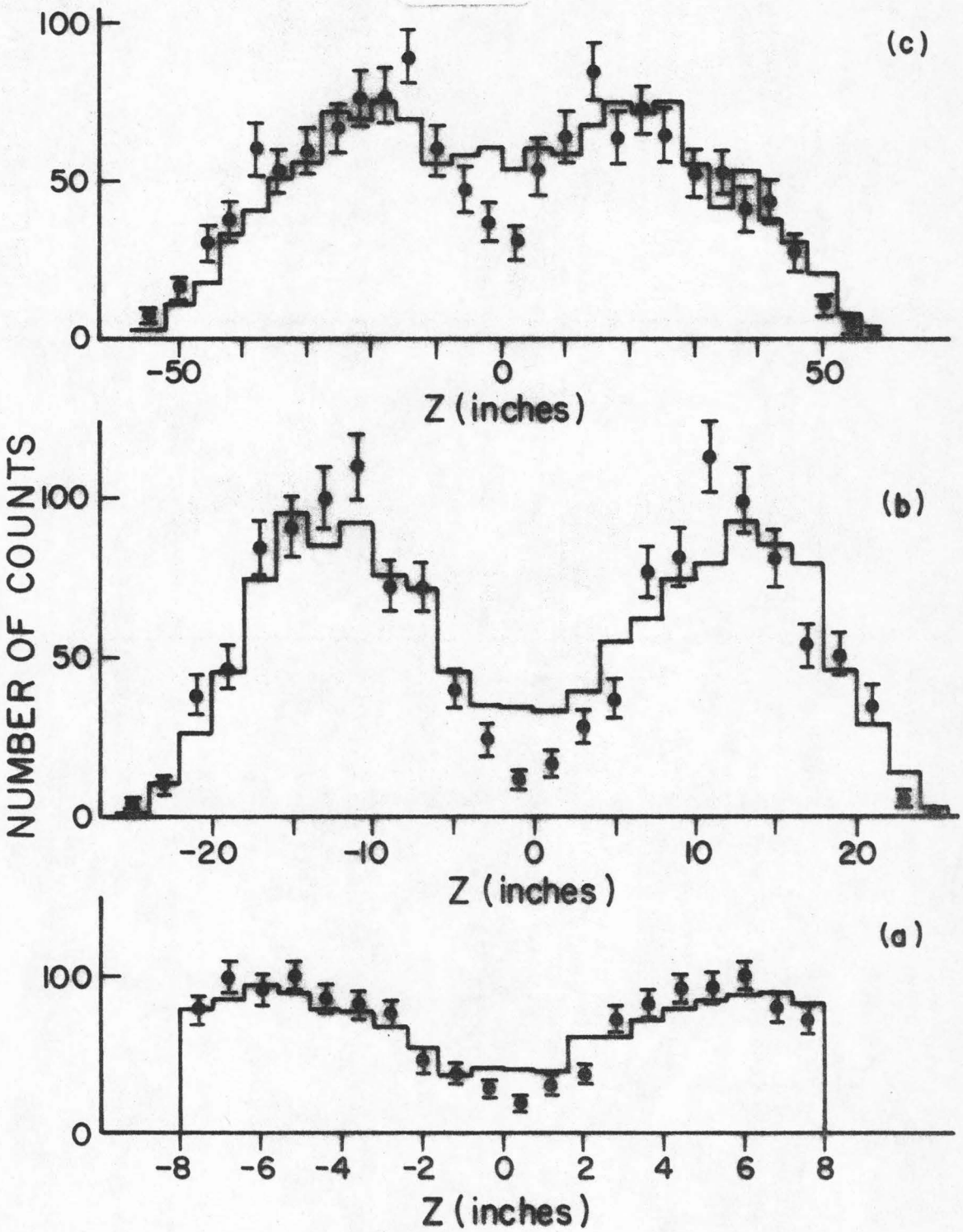

Figure 34 - Comparison of track density distributions between calibration run data (points) and Monte Carlo events in the plan views at the (a) S5, (b) MH, and (c) RH apertures.

The largest discrepancy between the $K_S \rightarrow 2\pi$ data and the Monte Carlo calculation was that there was only 70% ± 10% as many T2 events as expected (relative to the number of T1 events). This effect could have been caused by the different geometrics of the two targets (both location and size). Charged secondaries generated in T2 could strike the MH (thus vetoing the event) without passing through V2 (this was not true of T1). Charged secondaries in T2 had less brass to traverse (1/2 the diameter of T1) in order to reach V2. Finally, Λ's generated in T2 were substantially closer to the MH (55" vs 80") so that their decay products could strike the MH more readily thus vetoing the event. It was not possible to include these effects in the Monte Carlo calculations so this normalization difficulty remains unsolved. Partially for this reason the $K \rightarrow 3\pi$ events from T2 were not used in the final data sample.

$K \rightarrow 3\pi$

The $K \rightarrow 3\pi$ Monte Carlo calculation was done in much the same way as the $K \rightarrow 2\pi$ calculation. The momentum and angular distributions of the K^O's as determined from the $K \rightarrow 2\pi$ calculations were used to generate K^O decays at four longitudinal positions in the Production-Decay Region. The decays were initially generated with a uniform Dalitz plot distribution. The charged secondaries were then put through the same program as the $K \rightarrow 2\pi$ events in order to trace the orbits through the magnet and to apply aperture requirements. The same requirements were made on these events as the $K \rightarrow 2\pi$ events with the following differences:

a) The MH requirement (# 5) did not demand the one counter separation between the triggered counters.

b) The tracks did not have to pass through the gas counter window (# 3).

c) The tracks had to be on opposite sides of the RH (# 6). (One had to go through RH #1-#16 while the other went through #17-#32.)

d) One of the γ-rays from the π^o decay had to hit the shower counters.

The events which met these demands were written out on magnetic tape.

Later these $K \rightarrow 3\pi$ events on the tape were subjected to additional requirements (see the discussion in Chapter IV). These events were weighted and cut to include the effects of:

1) The Dality plot density dependence on $M_{\pi^+\pi^-}$.

2) The shower counter γ-ray energy bias (see Figure 15).

3) The geometric effects of the computer scan.

4) The Λ-mass cut at $M_\Lambda > 1.2$ GeV.

The successful events were then compared with the events in the $K \rightarrow 3\pi$ data sample. The comparisons of the $\pi^+\pi^-$ mass squared distributions and the opening angle distributions are shown in Figures 19 and 20. The track position distributions at the counter apertures S5, MH, RH, and the shower counters are shown in Figures 35, 36, 37, and 38. The γ-ray shower counter position distributions are compared in Figure 39. The number of events with the three possible topologies (forms of the trajectories) are compared in Figure 40.

In all of the above distributions the Monte Carlo events compare quite well with the data events. This lends confidence to both the Monte Carlo calculation and to the data reduction procedures.

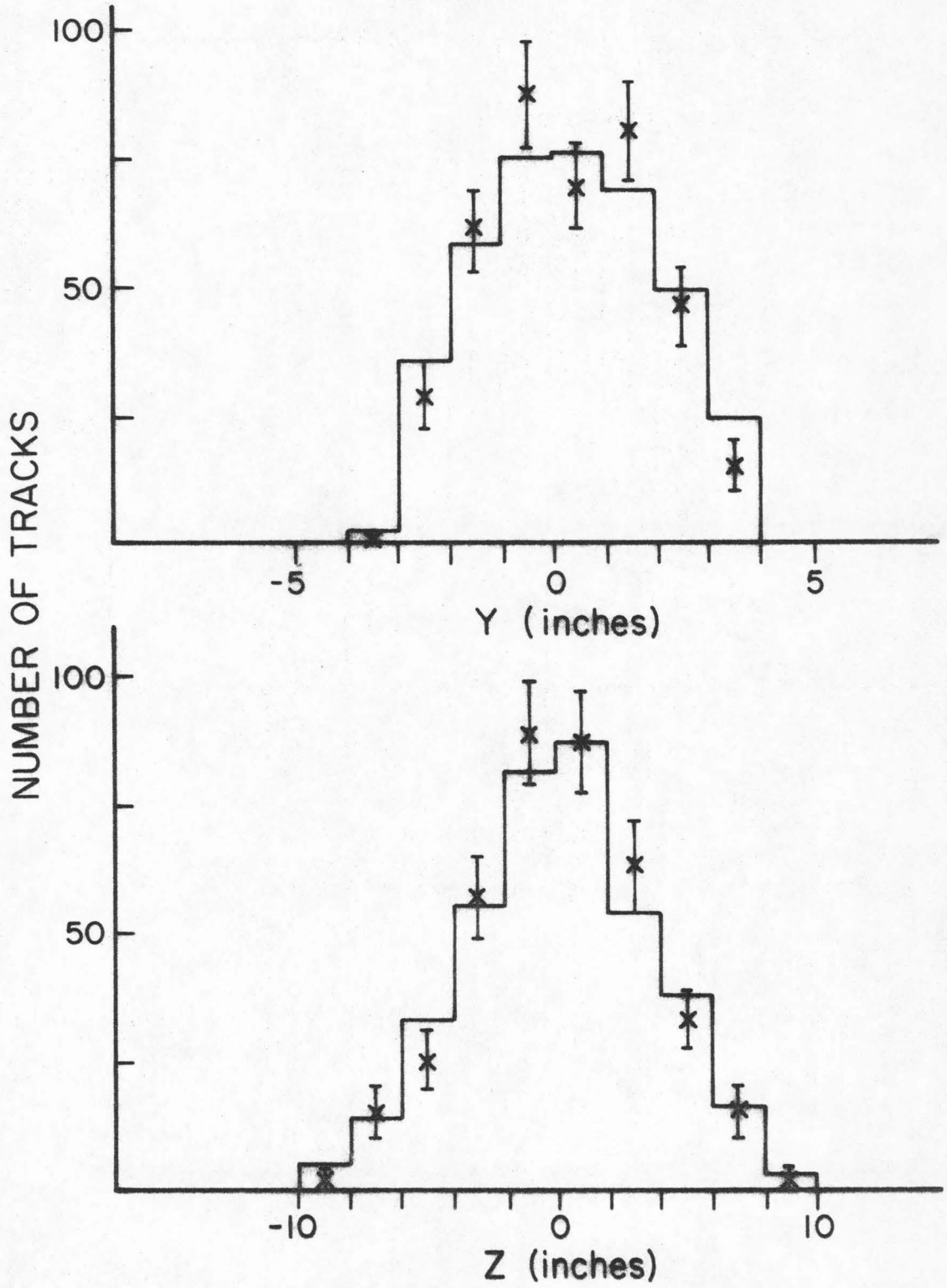

Figure 35 - Comparison of the track density distributions between $K \rightarrow 3\pi$ data events (X) Monte Carlo events (histograms) at the S5 counter aperture. The elevation view is Y and the plan view is Z.

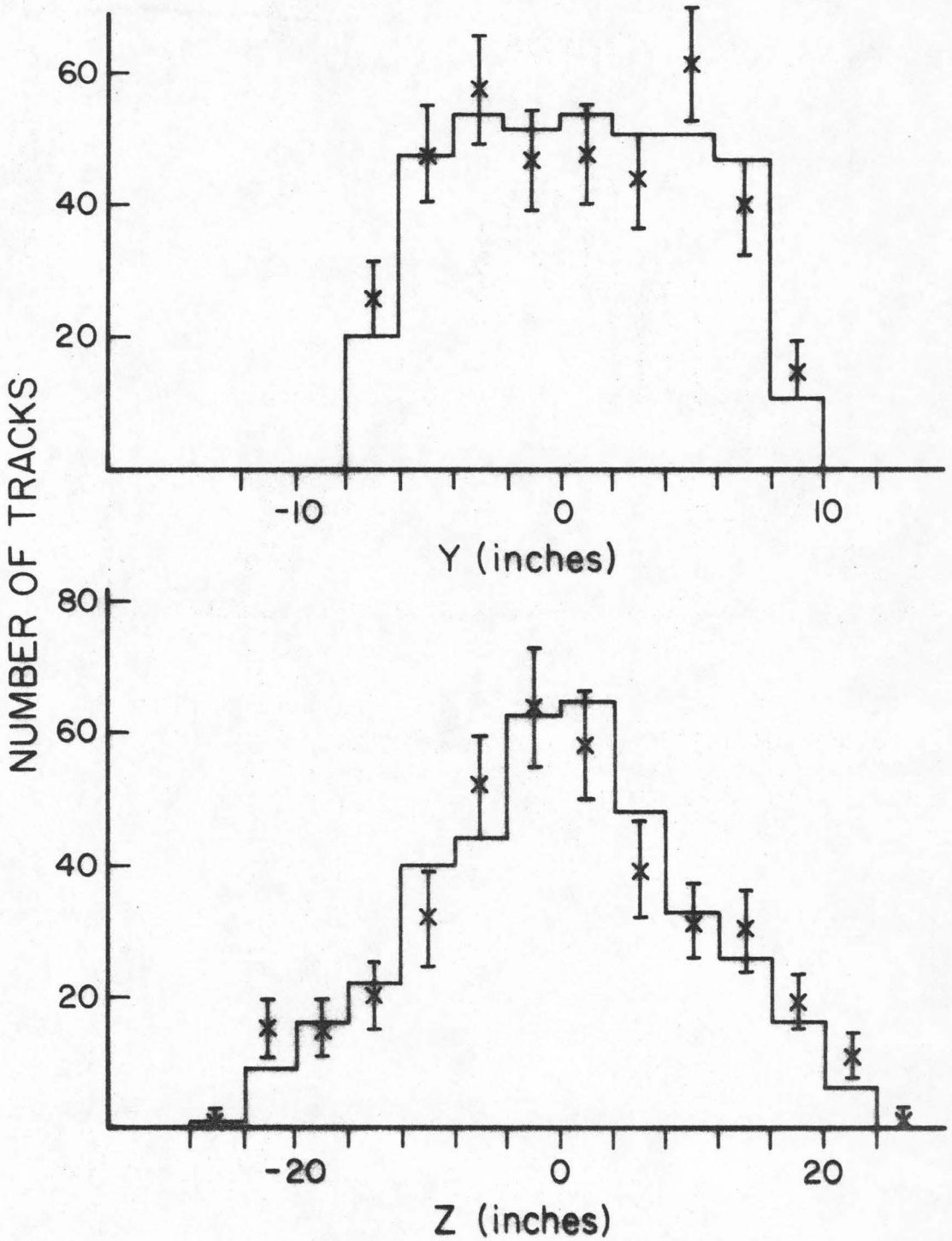

Figure 36 - Comparison of the track density distributions between $K \rightarrow 3\pi$ data events (X) Monte Carlo events (histograms) at the MH counter aperture. The elevation view is Y and the plan view is Z.

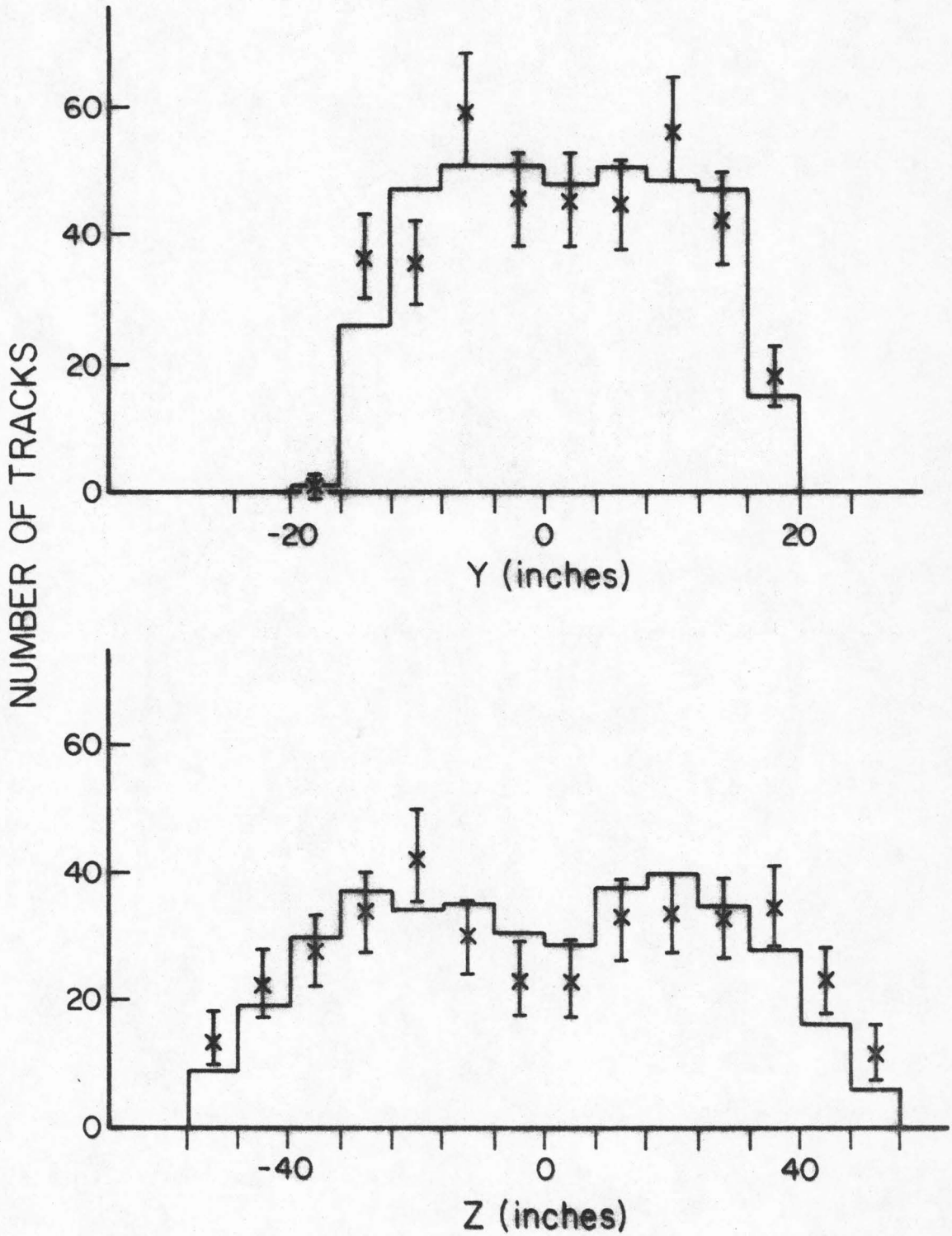

Figure 37 - Comparison of the track density distributions between $K \rightarrow 3\pi$ data events (X) Monte Carlo events (histograms) at the RH counter aperture. The elevation view is Y and the plan view is Z.

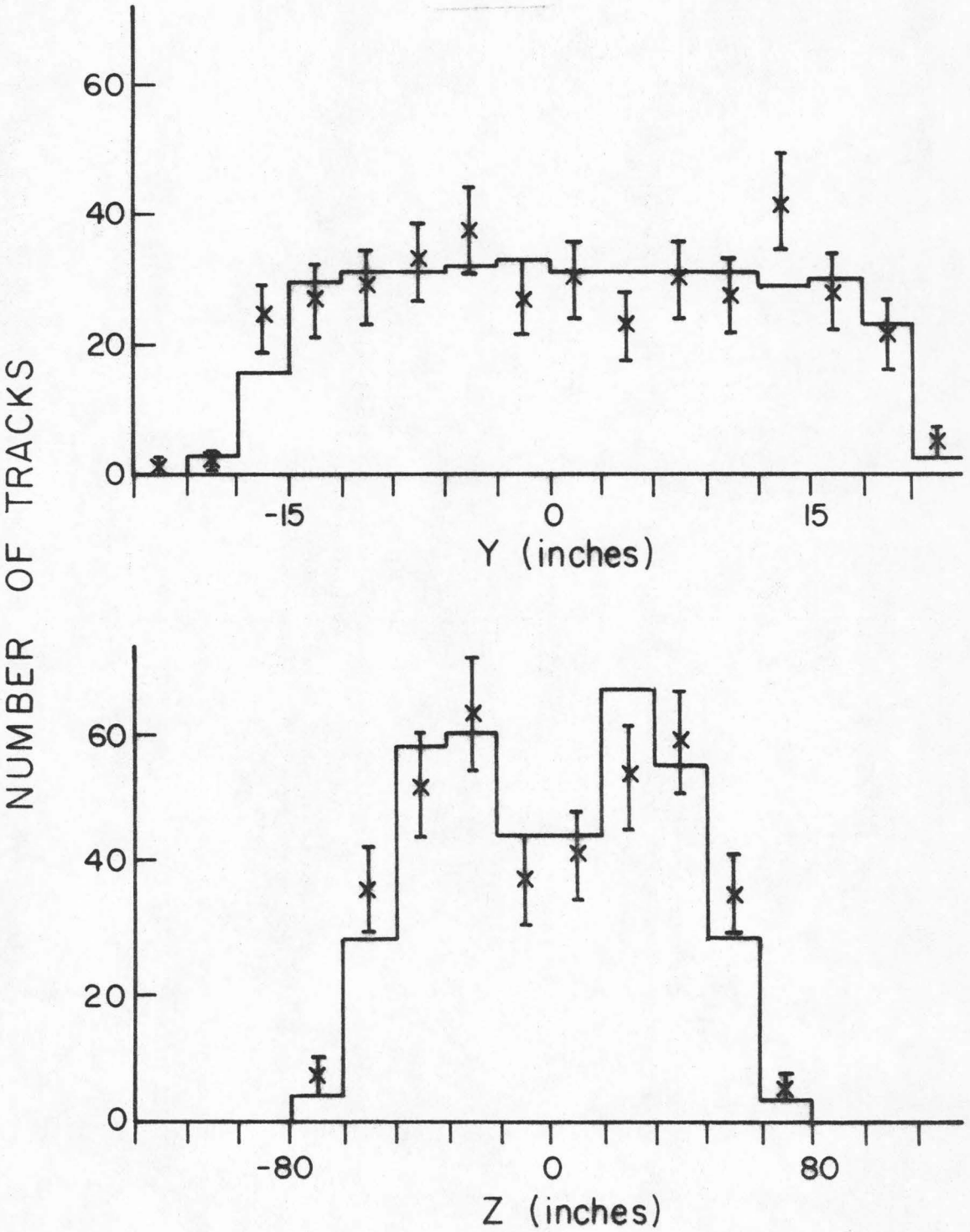

Figure 38 - Comparison of the track density distributions between $K \rightarrow 3\pi$ data events (X) Monte Carlo events (histograms) at the shower counter aperture. The elevation view is Y and the plan view is Z.

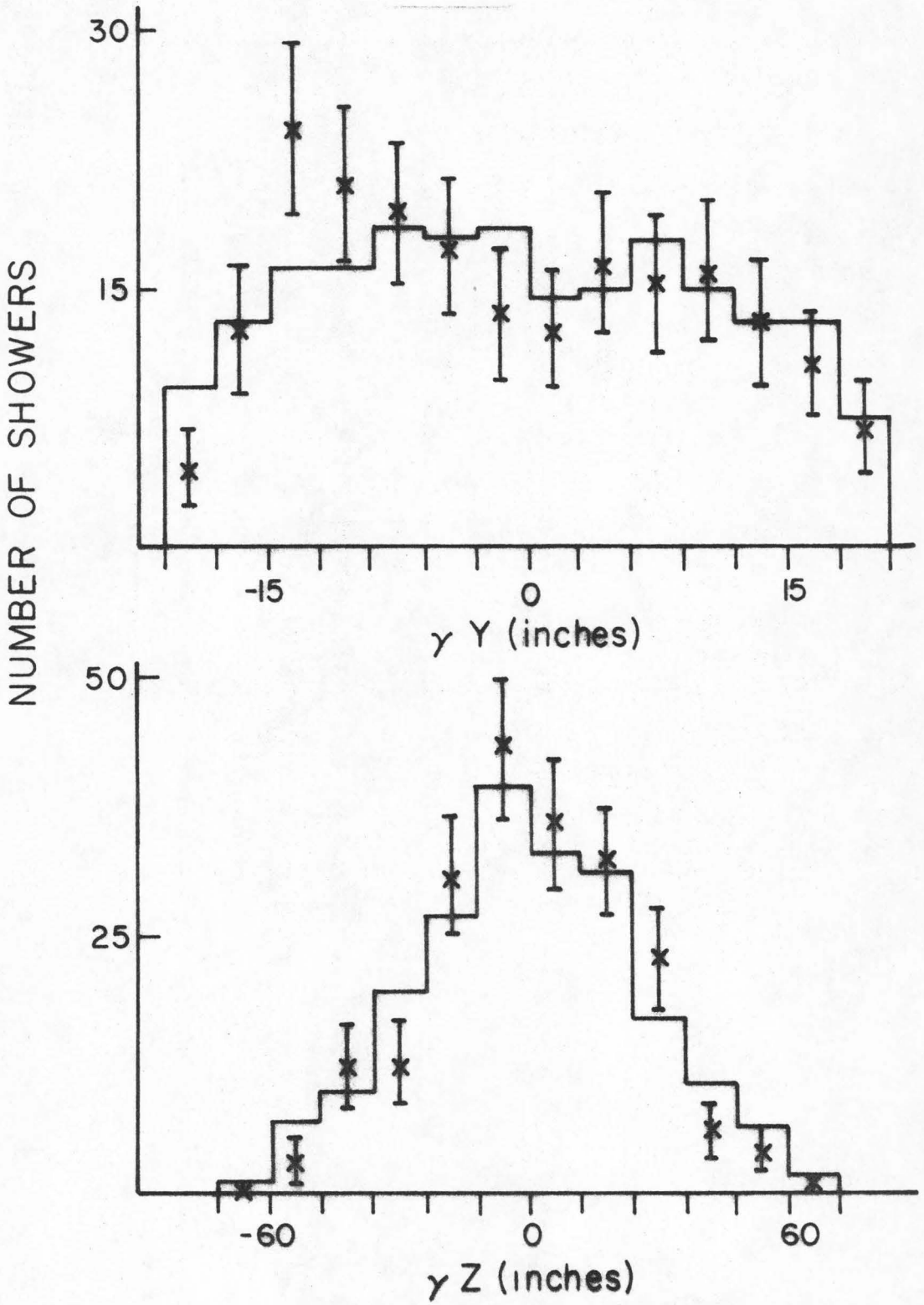

Figure 39 - Comparison of the γ-ray density distributions between $K \rightarrow 3\pi$ data events (X) Monte Carlo events (histograms) at the shower counter aperture. The elevation view is Y and the plan view is Z.

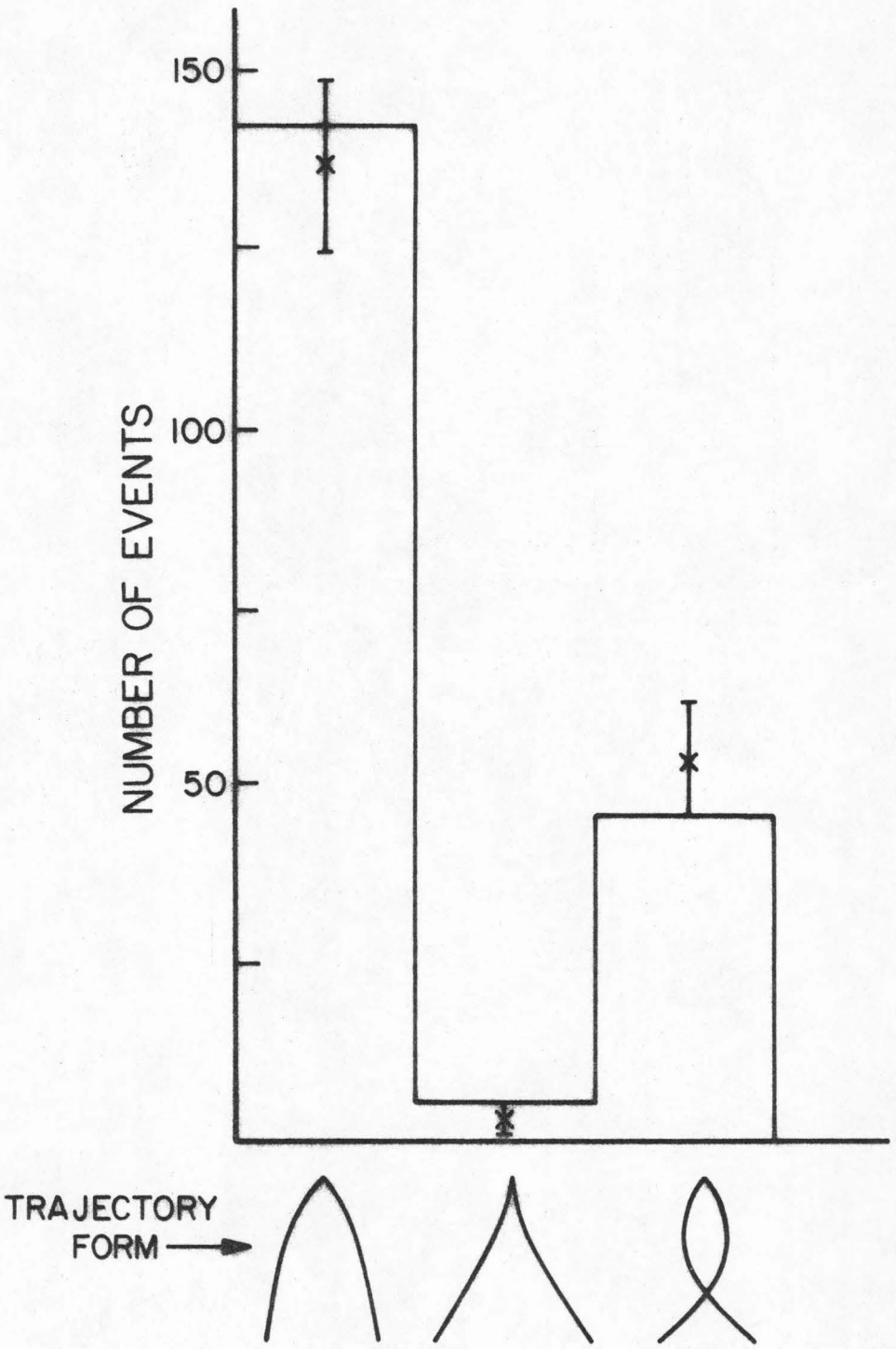

Figure 40 - Event Topologies.

APPENDIX XII - DOWNSTREAM COUNTERS AND HODOSCOPES

The first counter encountered by particles entering the magnet was S5. The scintillator for this counter was 8" high, and 18" wide, and 1/8" thick. The firing of this counter in coincidence with the "TARG" signal from the targets indicated the production of a neutral in the target and its decay in front of S5 which was located immediately in back of the Production-Decay Region. S5 was made as thin as possible to minimize the conversion of γ-rays in its material. The electrons for S5 were included in the beam logic (BM5). It is diagrammed in Figure 26 in Appendix IV.

The gas counter was located in back of S5 between the pole pieces of the magnet (see details in Appendix VI). It was sensitive to electrons with momenta greater than 11.1 MeV/c, and produced the logic signal GC when an electron traversed it.

The Multiples Hodoscope consisted of 15 pieces of Pilot γ scintillator, 60" long, 1" wide, and 3/8" thick. These were stacked vertically to form an array 15.7" high and 60" wide, located perpendicular to the beam, 8.7" downstream of the magnet center, directly in back of the rear window of the gas counter. The scintillator was chosen for its low attenuation in order to avoid a right-left position bias. The M value (mean number of photo electrons) for the Poisson distribution of pulse heights ranged from 20 at the far end to 60 at the end near the photo tube. This large number of photo-electrons and an examination of position distributions of accepted events indicate that no lateral asymmetry was induced by this hodoscope. Each counter was provided with a 6655A photo tube. The

photo tubes were located in a vertical gap in the return path of the magnet and were thus subject to relatively small fields.

The electronics for the Multiples Hodoscope is diagrammed in Figure 41. There are three basic internal logic signals generated:

MHG1: more than 1 counter triggered.

MHG2: more than 2 counters triggered.

MHAC: adjacent counters triggered.

These signals are combined with the beam signal (BM5) to yield the two basic MH outputs:

$$MH^{*} = MHG1 \cdot \overline{MHG2} \cdot BM5$$

$$MH = MHG1 \cdot \overline{MHG2} \cdot \overline{MHAC} \cdot BM5$$

MH^{*} indicates that two (and only two) counters triggered. It was used in the "VEEM" ($K \rightarrow 2\pi$) trigger and the "PPG" ($K \rightarrow 3\pi$) trigger. MH indicates that two (and only two) counters triggered and that these two counters were separated by at least one counter that did not trigger. This signal was used in the "PIE" ($K \rightarrow \pi e \nu$) trigger. The separation requirement helped to reduce the $e^{+}e^{-}$ background which usually triggered adjacent MH counters because of its small opening angles.

Both MH^{*} and MH were designed to bias for two charged secondaries in the active region of the Momentum Spectrometer.

The Rear Hodoscope further reinforced the requirement of two charged secondaries passing through the Momentum Spectrometer. It consisted of 32 counters (Pilot γ scintillator) 42" long, 4" wide, and 1/4" thick, oriented vertically. The counters were mounted in two groups, 42" high, and 65" wide. The normal to each group was 16° to the beam line so that the average track was perpendicular to the group. The two

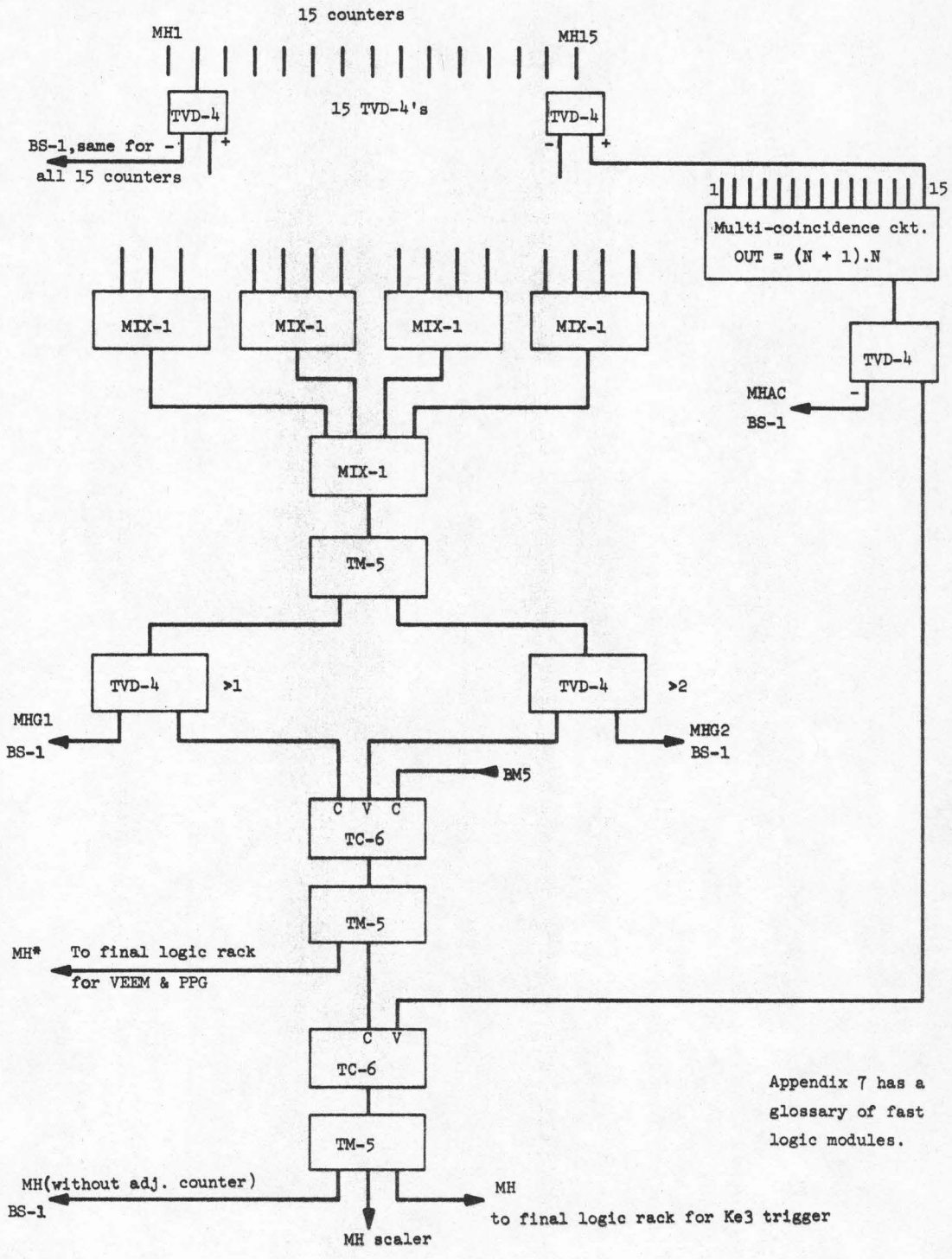

Figure 41 - Fast Multiples Hodoscope Logic (MH).

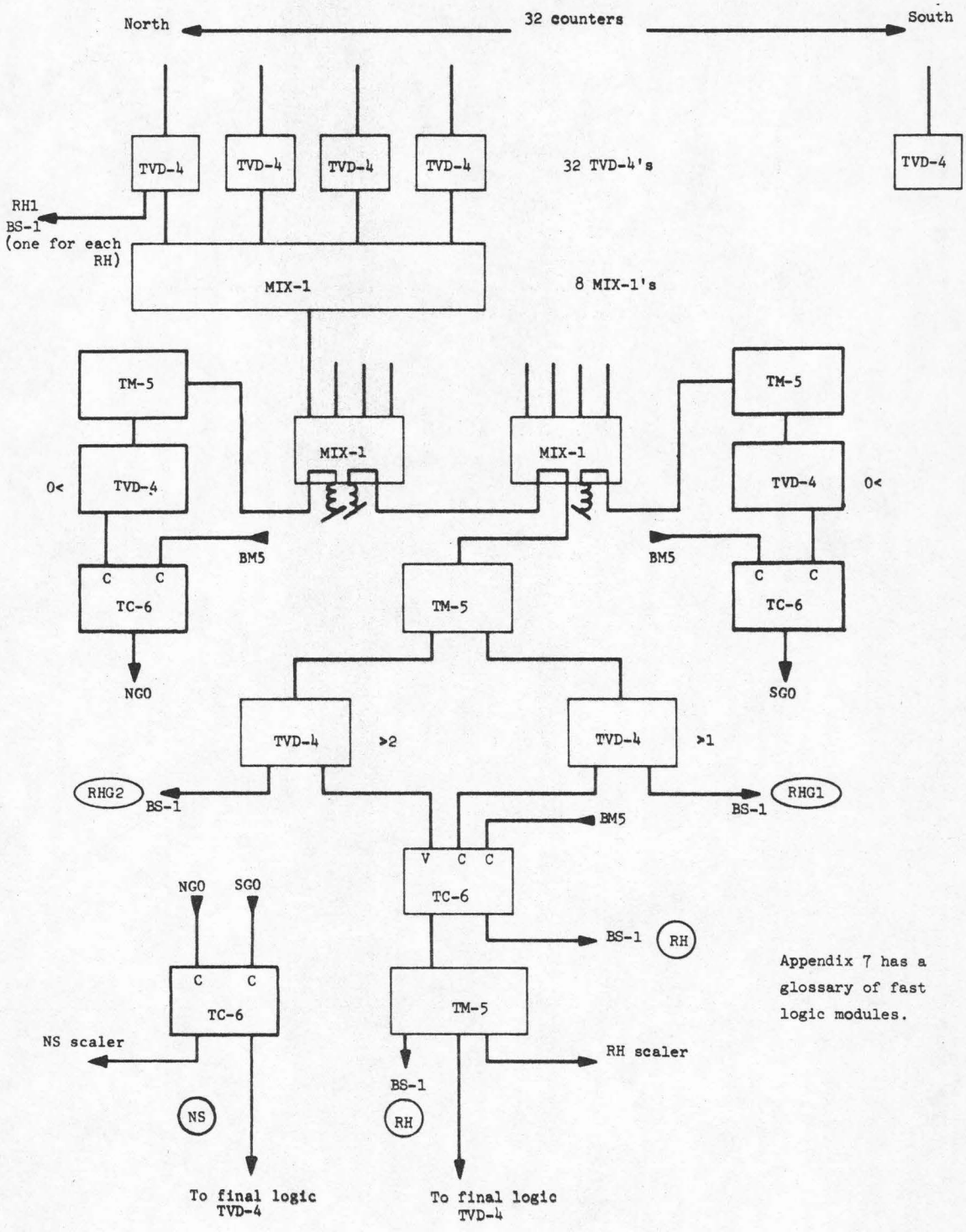

Appendix 7 has a glossary of fast logic modules.

Figure 42 - Fast Rear Hodoscope Logic (RH).

groups touched at the center line. Counters #1 to #16 were on the north side of the apparatus and counters #17 to #32 were on the south side. Each group was mounted on a moveable cart with the Shower Chamber and Shower Counter directly behind it.

The logic for the Rear Hodoscope is shown in Figure 42. Four outputs to the BS-1 were generated. The RHG1 indicates that more than one counter triggered. RHG2 indicates that more than two counters triggered. As with MHG1 and MHG2 the logic here was done by adding the pulse-shaped signals for all the counters and then feeding them into discriminators which fire when the signal exceeds a level corresponding to the sum of a certain number of pulses. The outputs which were used in the fast logic and also went to the BS-1 were RH and NS. RH indicates that two (and only two) counters fired and is used in all the triggers. NS indicates that at least one counter on each side of the apparatus triggered. It was used in the PPG ($K \rightarrow 3\pi$) trigger to isolate events in which the pions were on opposite sides of the center line.

The Shower Counters consisted of 14 modules arranged symmetrically about the center line in two groups of seven. Each group was mounted behind its shower chamber which was behind its Rear Hodoscope, and all were mounted on the same cart with their normal at a 16^{o} angle to the beam. Each module consisted of two pieces of Ne 102 scintillator, 52" high, 10" wide, and 3/8" thick. The two 6655A photo tubes for each module were attached at opposite ends to their scintillator and their pulses were added, thus the attenuation tended to average out. The photo tubes were attached through light pipes that made a 90^{o} bend in order to make the assembly more compact. Between the two slabs of

scintillator for each module there was a .4" sheet of lead (2 radiation lengths) sandwiched between 2, 1/4" sheets of styrofoam which were sandwiched between 2 sheets of aluminum. There were 2 such aluminum-styrofoam-lead sandwiches. Each one served as the radiator in one of the groups of 7 shower modules. The pulse height for each module was analyzed and became part of the tape record for each event. The fast logic associated with the shower counter is shown in Figure 43. The pulse from each group of 7 modules was added. If the sum for the group on the north side exceeded 3 times minimum ionizing then the logic signal SHN was generated. If this happened for the group of 7 on the south side then SHS was generated. If either SHN or SHS occurred then SH was generated. SH was one of the requirements for the PPG ($K \rightarrow 3\pi$) trigger. It biased towards events with an associated γ-ray. Throughout the running of the experiment the gains on the photo tubes for each module were adjusted so that the pulses produced by the modules were the same for minimum ionizing tracks.

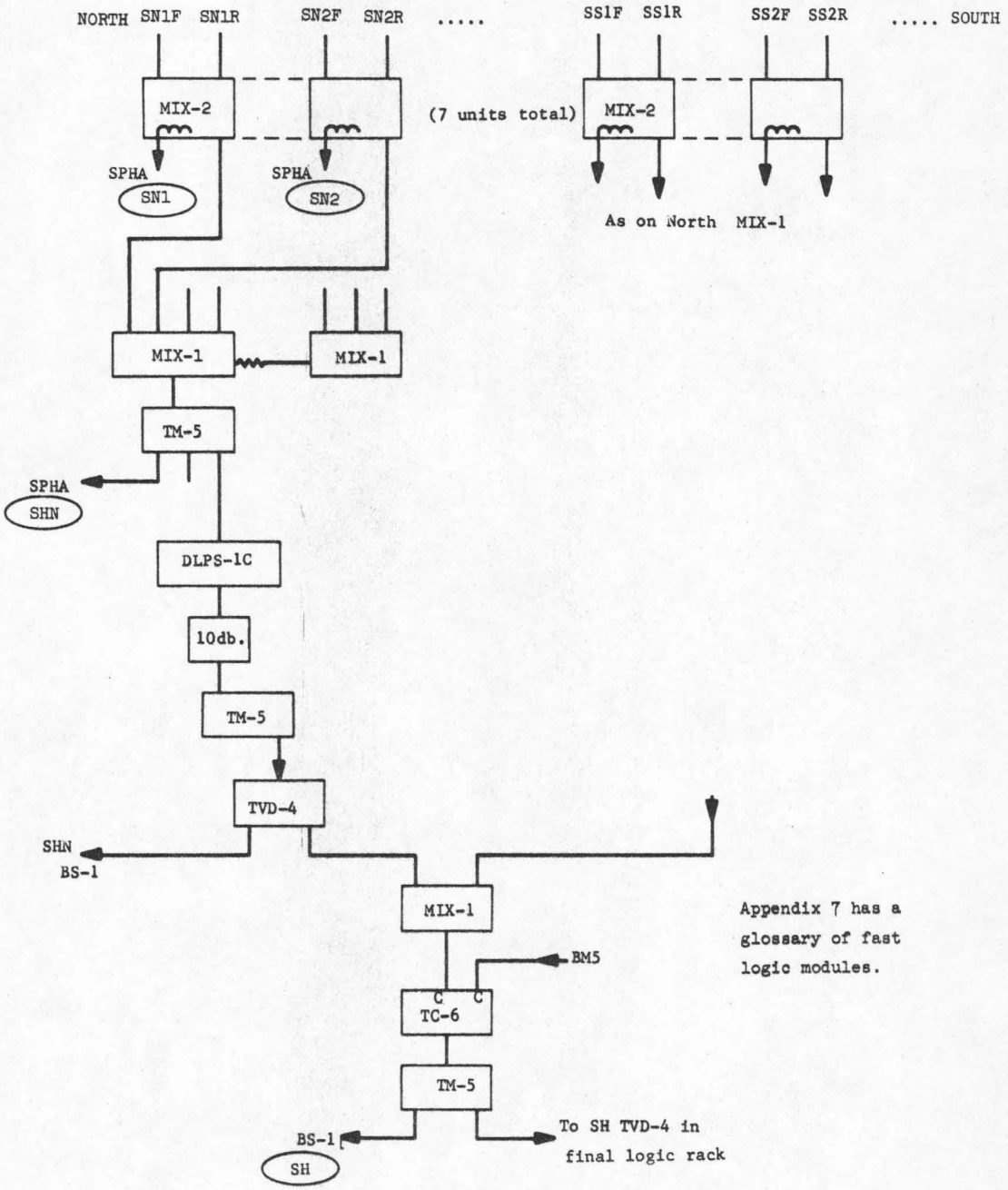

Figure 43 - Fast Shower Counter Logic (SH).

APPENDIX XIII - APPARATUS CHECKS AND RUNNING PROCEDURES

The apparatus for this experiment was a multi-media extravaganza. Left to itself something was likely to go wrong in a few hours of running. Therefore a procedure of checks was adopted to monitor all pieces of equipment that were likely to misbehave. The cameras were examined whenever the film was changed (~ twice per day). The firing of all the spark chambers and fiducials were visually checked every four hours. At the same time the photo tube supply voltages and the lights that connected the BS-1 to the electroluminescence panels for displaying logic information were checked. Each role of film was checked to monitor the performance of the logic lights and the overall optical recording system.

During each data run (there were ~700) the number of counts for various counters and logic signals was scaled. At the end of the run these counts were normalized to the total beam counts and plotted with previous runs. Any irregularities in the performance of these counters were quickly spotted and corrected. In addition the PDP-8 computer kept histograms of counting rates in the various hodoscopes. The display of these histograms on a CRT allowed the diagnosis of trouble in the logic path from the counters to the computer. The gains in the Cerenkov counters were checked periodically against a reference source (C_S 137 embedded in the scintillator and glued to the face of the photo tube). The photo tube voltages were adjusted to obtain a predetermined pulse height from the reference source. The pulse heights for the shower counters were calibrated against minimum ionizing tracks. Necessary adjustments were made periodically.

During the period of data taking the magnetic field in the spectrometer was reversed 25 times. This was done to cancel out any geometric charge asymmetries in the apparatus for the benefit primarily of the Ke_3 experiment. Each time the field was reversed the gains in the Cerenkov counter and the shower counters were adjusted to compensate for the effect of the changed fringe field on the photo tubes. The hodoscope counters were also checked for any difficulties. The magnetic currents were monitored to .1% and the field in the spectrometer was checked to 1% by means of a flip coil near the center of one of the pole faces. Later the field was mapped spatially to 1% with a mobile coil.

During the data taking the normal apparatus trigger was "PIE" (Ke_3 trigger) together with "PPG" ($K \rightarrow 3\pi$ trigger)(see Appendix VII). Approximately every 12 hours a calibration run of about 1500 triggers was taken. The "vee" trigger ($K \rightarrow 2\pi$ trigger) was put in parallel with the above two triggers ("veem" was used instead of "vee" after the first month of running). The "vee" trigger then produced the vast majority of the events in the calibration runs. These triggers were later used to isolate $K \rightarrow 2\pi$ events to aid in the Monte Carlo analysis. Also the periodic use of this more basic trigger provided additional checks on the apparatus.

APPENDIX XIV - SLOW ELECTRONICS

The slow electronics consisted of a PDP-8 computer (4K memory and a 1.5 US memory cycle time), the BS-1 buffer storage circuits, the SPHA slow pulse height analyzer (64 channel capacitor storage included), the data light control circuits and camera control units. The sequence of events was that the fast digital information was read into the BS-1 for temporary storage and the fast analog information (pulse heights) was stored in the capacitor storage channels of the SPHA. The electronics were then clamped and the spark chambers were fired. After the spark chamber noise settled down a read control circuit read into the PDP-8 accumulator the digital information on the BS-1 and the analog information stored as charges on the capacitors (read these through the intermediary of the SPHA). The resident PDP-8 program, EXPO (see DECUS No. 8-161 for details) was interrupted (from what ever it was doing at the time) and the new data was stored in the memory as 12 bit words (12 counters to a word). The analog information (pulse heights) used 6 bits per counter. After the computer had accumulated three events (both data events and tape events) the information was written as a record on magnetic tape by means of a double buffered (low dead time) DATAMEC D2020 tape unit. Along with handling these input-output operations the EXPO program kept histograms for monitoring the apparatus performance.

At the same time that the BS-1 information was being read into the computer, some of the information was used to activate electro-luminescent panels which left images on the film to aid in the scanning. The circuitry

for the lights was electronically isolated from the BS-1 (to prevent noise pick up from the spark chambers) by transmitting the information as a light pulse through light pipes to LASCR's. These LASCR's then activated the relays that pulsed the electro-luminescent panels. After these logic lights, the transfer fiducial lights and the serial number lights were pulsed, the camera control units advanced the cameras one frame. Between each beam pulse the full fiducial lights were pulsed and loop generators in each camera pulled seven frames of film off the feed reel. These frames saved the camera from having to work against the inertia of the 1200 foot reels.

APPENDIX XV - THE $K\mu_3$ MODE

The contribution from the $\pi\mu\nu$ mode to equation (1.6) is complicated by the lack of good data and the appearance of an additional form factor in the decay. The most general form for the matrix element assuming the V-A theory is:

$$F = \frac{1}{\sqrt{P_{K4}P_{\pi 4}}}\left[(P_K+P_\pi)_\lambda f_+(q^2) + (P_K-P_\pi)_\lambda f_-(q^2)\right]\ \psi_\ell \gamma_\lambda(1+\gamma_5)\psi_\nu \qquad \text{(AXV.1)}$$

where $P_{K\lambda}$ and $P_{\pi\lambda}$ are the momentum four vectors of the K and the π, and λ is summed from 1 to 4. The $f(q^2)$'s are form factors which are functions of $q^2 = (P_K-P_\pi)^2$ only. The γ's are the Dirac γ matrices and the ψ's are the spinors of the lepton and the neutrino. f_+ contributes to Ke_3 and $K\mu_3$ decays but f_- contributes substantially only to $K\mu_3$ decays because it is suppressed by a factor of $\frac{M_\ell}{M_K}$. F represents the $\Delta S = -\Delta Q$ transition amplitude by replacing F by g, f_+ by g_+ and f_- by g_-, then the $\Delta S = \Delta Q$ violating parameter, X, for the electron mode is defined by:

$$X = \left\langle\frac{g_e}{F_e}\right\rangle \qquad \text{average over } q^2$$

$$X = \left\langle\frac{g_+}{f_+}\right\rangle \qquad \text{(AXV.2)}$$

For the muon mode a similar parameter X' is defined by:

$$X' \approx X + \frac{m_\mu}{M_K}\left(\frac{g_-}{f_+} - \xi X\right) \qquad \text{(AXV.3)}$$

where $\xi = \frac{f_-}{f_+}$. $\qquad$ (AXV.4)

When equation (AXV.1) is squared and summed over the spins and multiplied by the phase space, the distribution of decays in q^2 and $\cos\alpha$ (α is the angle between the leptons and the pion in the center of mass of the leptons) is:

$$\frac{dN}{d(q^2)d(\cos\alpha)} = \frac{\vec{P}_\pi{}^3(-q^2-m_\ell{}^2)^2}{16\pi^3(-q^2)^2}\left(|A_R|^2 + |A_L|^2\right) \qquad \text{(AXV.5)}$$

where $A_R = f_+\sin\alpha$ (AXV.6)

is the amplitude for right spining muons in the leptons C.M. and

$$A_L = \frac{m_\mu}{\sqrt{-q^2}}\left(\frac{1}{2M_K P_\pi}(-q^2 f_- + (M_K{}^2 - M_\pi{}^2) f_+) + f_+\cos\alpha\right) \qquad \text{(AXV.7)}$$

is the amplitude for left spinning muons in that frame. $\vec{P}_\pi$ is the pion momentum in the rest frame of the K^o.

The contribution of the $\pi\mu\nu$ mode to $\mathrm{Im}\Gamma_{K\bar{K}}$ (defined by equation 1.6) occurs in two pieces. The A_R and A_L in equation (AXV.5) represent orthogonal spin states and are therefore to be treated separately in the sum in equation (1.6). The contribution from the right hand muons is:

$$2(i\mathrm{Im}\Gamma_{K\bar{K}})_{\text{right }\mu} = \int dq^2 d(\cos\alpha)\pi\varphi_{\pi\mu\nu}(f_+^* g_+ - g_+ f_+^*)(\sin^2\alpha) \qquad \text{(AXV.8)}$$

$$= 2i\mathrm{Im}X\ \gamma_{K_L\to \text{ right }\mu}$$

as with equation (5.7). For the left hand muons we get:

$$2(i\mathrm{Im}\Gamma_{K\bar{K}})_{\text{left }\mu} = \int dq^2 d(\cos\alpha)\pi\varphi_{\pi\mu\nu}(A(f)^*_L A(g)_L - A(g)_L A(f)^*_L) \qquad \text{(AXV.9)}$$

where $2\pi\varphi_{\pi\mu\nu} = \dfrac{P_\pi{}^3(-q^2-m_\ell{}^2)^2}{16\pi^3(-q^2)}$ and $A_L(g)$ is defined by AXV.7 with g's replacing f's. When AXV.9 is integrated over q^2 and $\cos\alpha$ assuming no

q^2 dependence to the f's and the g's* we get

$$2i(\mathrm{Im}\Gamma_{K\bar{K}})_{\text{left }\mu} = \gamma_{K_L\to,\ \text{left }\mu}\, 2i\mathrm{Im}\left\{(1.51+.29\xi^*)X+(.29+.084\xi^*)\frac{g^-}{f_+}\right\} \tag{AXV.10}$$

where $\gamma_{K_L\to\ \text{left }\mu}$ was calculated assuming $\xi = -1$. This gave

$$\frac{\gamma_{K_L\to\ \text{left }\mu}}{\gamma_{K_L\to\text{right }\mu}} = .53$$

Assuming ξ is real (references 26,27) and is -1 we then get the total contribution to $\mathrm{Im}\Gamma_{K\bar{K}}$ from the muon mode as:

$$2(i\mathrm{Im}\Gamma_{K\bar{K}})_{\pi\mu\nu} = i(2\mathrm{Im}X(1.07) + (.143)\mathrm{Im}\,\frac{g^-}{f^+})\gamma_{K_L\to\pi\mu\nu} \tag{AXV.11}$$

From the above equation, the branching ratio for $K_{L\mu 3}$ and K_{Le3}[14], equation (5.7), and the assumption that $|\frac{g^-}{f^+}| < 1$ (corresponding to a maximal $\Delta S = \Delta Q$ violation) we get:

$$i\mathrm{Im}\Gamma_{K\bar{K}} = i(\mathrm{Im}X(1.03) \pm .03)\gamma_{K_L\to\ \text{all leptons}} \tag{AXV.12}$$

The error ($\pm$ .03) is reduced even further in Chapter V by utilizing measurements of X' (equation AXV.3) to limit g^-/f^+.

---

*This approximation is good to $\pm$15% over the range of q^2 (see reference 26).

APPENDIX XVI - THE $K\mu_3$ TIME DISTRIBUTION

The $K\mu_3$ experiments which were quoted in Chapter V (references 19 and 25) used the following time distribution to fit the data (initially pure K^o beams),

$$N_{\pm}(t) = \frac{h|f_+|^2}{4}\,(I' \pm II' - III') \qquad \text{(AXVI.1)}$$

$$I' = (1 + 2\mathrm{Re}X' + |X'|^2)e^{-\gamma_S t} + (1 - 2\mathrm{Re}X' + |X'|^2)e^{-\gamma_L t} \qquad \text{(AXVI.2a)}$$

$$II' = 2(1 - |X'|^2)\cos(\Delta m t)e^{-(\gamma_S+\gamma_L)t/2} \qquad \text{(AXVI.2b)}$$

$$III' = 4(\mathrm{Im}X')\sin(\Delta m t)e^{-(\gamma_S+\gamma_L)t/2}\,, \qquad \text{(AXVI.2c)}$$

where N_+ and $+II'$ is for positive muons and N_- and $-II'$ is for negative muons, γ_S and γ_L are the decay rates of the K_S and K_L, and Δm is their mass difference.

The above distribution is a fair approximation to the complete distribution but is not adequate if we wish to get information on g^-/f^+. The correct (accurate) pieces of this distribution are[37] ($X=g^+/f^+$ and $\xi = f_-/f_+$)*:

$$\begin{aligned} I = {} & \Big\{1+2\mathrm{Re}X+|X|^2+a\big(\xi(1+\mathrm{Re}X)+\mathrm{Re}\big[(1+X^*)g^-/f^+\big]\big) \\ & + b\big(\xi^2+2\xi\mathrm{Re}\big[g^-/f^+\big]+|g^-/f^+|^2\big)\Big\}e^{-\gamma_S t} \\ & + \Big\{1-2\mathrm{Re}X+|X|^2+a\big(\xi(1-\mathrm{Re}X)-\mathrm{Re}\big[(1-X^*)(g^-/f^+)\big]\big) \\ & + b\big(\xi^2-2\xi\mathrm{Re}\big[g^-/f^+\big]+|g^-/f^+|^2\big)\Big\}e^{-\gamma_L t} \end{aligned} \qquad \text{(AXVI.3a)}$$

$$II = 2\Big\{\big(1-|X|^2+a\big(\xi-\mathrm{Re}\big[X^*(g^-/f^+)\big]\big)+b\big(\xi^2-|g^-/f^+|^2\big)\Big\}\cos(\Delta m t)e^{-(\gamma_S+\gamma_L)t/2} \qquad \text{(AXVI.3b)}$$

$$III = 4\Big\{\big(\mathrm{Im}X + \tfrac{a}{2}\big(\xi\mathrm{Im}X+\mathrm{Im}\big[g^-/f^+\big]\big)+b\xi\mathrm{Im}\big[g^-/f^+\big]\Big\}\sin(\Delta m t)e^{-(\gamma_S+\gamma_L)t/2}\,, \qquad \text{(AXVI.3c)}$$

* If ξ is not assumed to be real all these expressions are modified as follows: $\xi(1+\mathrm{Re}Z)\to\mathrm{Re}[\xi(1+Z)]$, $\xi\mathrm{Re}Z\to\mathrm{Re}(\xi Z)$, $\xi\mathrm{Im}Z\to\mathrm{Im}(Z\xi)$ and $\xi^2\to|\xi|^2$.

where the $(-q^2)$(the lepton-neutrino invariant mass squared) dependence of the form factors has been neglected.

The parameters a, b, c, d and h are given by:

$$a = \left[\iint A\epsilon(dq^2)(d\cos\alpha)\right]/h \qquad \text{(AXVI.4a)}$$

$$b = \left[\iint B\epsilon(dq^2)(d\cos\alpha)\right]/h \qquad \text{(AXVI.4b)}$$

$$c = \left[\iint C\epsilon(dq^2)(d\cos\alpha)\right]/h \qquad \text{(AXVI.4c)}$$

$$d = \left[\iint D\epsilon(dq^2)(d\cos\alpha)\right]/h \qquad \text{(AXVI.4d)}$$

$$h = \iint (C+D)dq^2)(d\cos\alpha) \qquad \text{(AXVI.4e)}$$

where ϵ is the efficiency function of the measuring apparatus as a function of (q^2) and $(\cos\alpha)$ (α is the angle between the π and the u in the lepton c.m.). The functions A,B,C, and D are determined from the Ke_3 kinematics to be:

$$A = \frac{P_\pi^2 m_\ell^2 (-q^2-m_\ell^2)^2}{16\pi^3 M_K (-q^2)^2}\left[\frac{(M_K^2-M_\pi^2)}{2P_\pi M_K} + \cos\alpha\right] \qquad \text{(AXVI.5a)}$$

$$B = \frac{P_\pi m_\ell^2 (-q^2-m_\ell^2)^2}{64\pi^3 M_K^2 (-q^2)} \qquad \text{(AXVI.5b)}$$

$$C = \frac{P_\pi^3 (-q^2-m_\ell^2)^2}{16\pi^3 (-q^2)^2}\left[\sin^2\alpha\right] \qquad \text{(AXVI.5c)}$$

$$D = \frac{P_\pi^3 (-q^2-m_\ell^2)^2 m_\ell^2}{16\pi^3 (-q^2)^3}\left[(\cos\alpha + \frac{M_K^2-M_\pi^2}{2P_\pi M_K})^2\right] \qquad \text{(AXVI.5d)}$$

where P_π = pion momentum in the K^o c.m.

(e.g. $(-q^2 = M_K^2 + M_\pi^2 - 2M_K\sqrt{P_\pi^2+M_\pi^2}$)

m_ℓ = lepton mass

M_π = pion mass

M_K = kaon mass

The values for a, b, c, and d have been obtained from a numerical integration of (AXVI.4) assuming no efficiency dependence ($\epsilon = 1$) to get:

$$a = .1932 \qquad \text{(AXVI.6a)}$$

$$b = .0289 \qquad \text{(AXVI.6b)}$$

$$c = .531 \qquad \text{(AXVI.6c)}$$

$$d = .469 \quad , \qquad \text{(AXVI.6d)}$$

for muons ($m_\ell = m_u = .106$ GeV). When we calculate these integrals for electrons ($m_\ell = m_e \approx 0$) we get:

$a \approx b \approx d \approx 0$, $c \approx 1$ and

$$\frac{h_e}{h_u} = 1.550 \; . \qquad \text{(AXVI.7)}$$

The coefficients A, B, C, and D appear in the various rate equations for K decay as the q^2, $\cos\alpha$ dependent factors times continuation of the form factors. From examination of AXV.1 and 5 we see that for K^o decay into $\pi^- \ell^+ \nu$ we get:

$$\frac{dN}{dq^2 d\cos\alpha} = |f_+|^2 C + |f_+|^2 D + |f_+ f_-^*| A + |f_-|^2 B \qquad \text{(AXVI.8)}$$

where the first term (C) corresponds to right helicity (in lepton c.m.) muons and the last three terms correspond to left helicity muons. In terms of these coefficients then (for the $\pi^- u^+ \nu$ mode)

$$\frac{d\Gamma_{K\bar{K}}}{dq^2 \cos\alpha} = \frac{1}{2}\left[(f_+^* g_+)(C+D) + \frac{(f_+^* g_- + f_-^* g_+)A}{2} + (f_-^* g_-)B\right] \; . \qquad \text{(AXVI.9)}$$

Then integrating over q^2 and $\cos\alpha$ with no form factor dependences on q^2 we get:

$$(\mathrm{Im}\Gamma_{K\bar{K}})_{\pi u\nu} = \frac{h_u|f_+|^2}{2}\,\mathrm{Im}(X+\frac{a}{2}(\xi^* X+g^-/f^+)+b\xi^*(g^-/f^+)). \qquad \text{(AXVI.10)}$$

This equation reduces to the sum of (AXV.8) and (AXV.10) by putting in numbers for a and b, c and d and noting that

$$\gamma_{K_L\rightarrow \text{ right helicity } u^+} = h_u|f_+|^2(\frac{c}{X})(\frac{1}{2}) \quad . \qquad \text{(AXVI.11)}$$

It is also clear that (AXVI.10) is equal to the non-time dependent part of (AXVI.3c) (that is III) so that the fit to this term in the $K\mu_3$ time distribution (AXVI.1) produces directly the number which contributes to $(\mathrm{Im}\Gamma_{K\bar{K}})_{\pi u\nu}$. This is the analysis that is used to obtain result (5.9) from the $K\mu_3$ data (references 19 and 25).

The fits to the $K\mu_3$ data, however, are not quite correct. The experimenters have used equations (AXVI.2) instead of the accurate equations (AXVI.3) (see reference 37). Without the actual data it is not possible to tell for sure what the results would have been if the accurate distribution (AXVI.3) was used with limit on X from the Ke_3 data (Table 9). However, if X is assumed to be negligible the $K\mu_3$ distribution is:

$$N_\pm(t) = \frac{hk|f_+|^2}{4}(I''\pm II''-III'') \quad , \qquad \text{(AXVI.12)}$$

with:

$$I'' = \left(1+\left(\frac{a+2b\xi}{k}\right)\mathrm{Re}\left[g^-/f_+\right]+\frac{b}{k}|g^-/f_+|^2\right)e^{-\gamma_S t}$$

$$+\left(1-\left(\frac{a+2b\xi}{k}\right)\mathrm{Re}\left[g^-/f_+\right]+\frac{b}{k}|g^-/f_+|^2\right)e^{-\gamma_L t} \qquad \text{(AXVI.13a)}$$

$$II'' = 2\left(1-\frac{b}{k}|g^-/f_+|^2\right)\cos(\Delta mt)e^{-(\gamma_S+\gamma_L)t/2} \qquad \text{(AXVI.13b)}$$

$$III'' = 4\left(\frac{1}{2}\left(\frac{a+2b\xi}{k}\right)\mathrm{Im}\left[g^-/f_+\right]\right)\sin(\Delta mt)e^{-(\gamma_S+\gamma_L)t/2} \qquad \text{(AXVI.13c)}$$

and

$$k = 1 + a\xi + b = .83 \text{ if } \xi = -1 \qquad \text{(AXVI.13d)}$$

(from equations (AXVI.6a and b) a = .193 and b = .023).

Note that the $|g^-/f_+|$ term in II'' appears with a coefficient $\sqrt{\frac{b}{k}} = .167$ while the $\mathrm{Im}(g^-/f_+)$ term in III'' appears with a coefficient $\frac{a+2b\xi}{2k} = .082$.

The ratio of these two coefficients is 2 to 1 whereas the ratio of the analogous coefficients in the distribution used to fit the $K\mu_3$ data is 1 to 1 (equations AXVI.2). Therefore, $K\mu_3$ data is more sensitive to $|g^-/f_+|$ in comparison to $\mathrm{Im}\left[g^-/f_+\right]$ than one would expect from analogy with Ke_3 data.

The next step in this analysis is to note that the time distribution for $\pi^+e^-\nu$ at $t \approx 0$ is extremely sensitive to $|g^-/f_+|$. If $|g^-/f_+| = 0$ then there should be no $\pi^+u^-\nu$ events at $t = 0$. On the other hand, the terms involving $\mathrm{Re}\left[g^-/f_+\right]$ and $\mathrm{Im}\left[g^-/f_+\right]$ both produce effects only in regions where there are events even if $|g^-/f_+| = 0$. Therefore, one could strongly suspect that the $K\mu_3$ experiments have principally measured $|X'|$ through the II'' term so that we can equate $|X'|$ with $|g^-/f_+|\sqrt{b/k}$. From the result (5.8) then

$$|X'| < .18 \ ,$$

$$\text{so that} \quad |g^-/f_+| < \frac{.18}{.167} = 1.08 \ . \qquad \text{(AXVI.15)}$$

This analysis is clearly shaky but it does suggest that a re-fitting

of the available data would be worthwhile. It is possible that the limits on $|g^-/f_+|$ could be reduced by a factor of two. The present limit assuming that the fits were sensitive to III' (worst case) is

$$\mathrm{Im}\left[g^-/f_+\right] = .68 \pm 2.18 \qquad \text{(AXVI.16)}$$

from the data in result (5.8).

REFERENCES

1. J. Christenson, J. Cronin, V. Fitch and R. Turlay, Phys. Rev. Letters 13, 138 (1964).

2. (a) $|\eta^{+-}| = (1.95 \pm .03)\times10^{-3}$

   $\varphi^{+-} = (44 \pm 3)$ degrees

   $\varphi^{oo} = (51 \pm 30)$ degrees

   Particle Data Group, Reviews of Modern Physics 43, 515 (1971).

   (b) $|\eta^{oo}|_{average} = (1.97 \pm .11)\times10^{-3}$ is the average of the following two results:

   $|\eta^{oo}| = (1.95 \pm .12)\times10^{-3}$ from the results of P.Darriulat, J. Deutsch, A. Fainberg, C. Grosso, M.Hansroul, M.Holder, S. Orito, J. Pilcher, E. Radermacher, C. Rubia, M.Scire, A. Staude, P.Strolin, K.Tittel and A. Villari (Aachen-CERN-Torino Collaboration), paper 144 contributed to the 1971 Amsterdam Conference.

   $|\eta^{oo}| = (2.02 \pm .23)\times10^{-3}$, V.V.Barmin, V.G.Barylov, V.S.Borisov, G.K.Bysheva, G.S.Veselovsky, V.M.Golubchikov, L.L.Goldin, G.V.Davidenko, A.G.Dolgolenko, V.S.Demidov, N.K.Zombkovskaya, L.N.Kondratiev, N.R.Konoplev, A.G.Meshkovsky, G.S.Mirosidi, G.K.Tumanov, T.A.Chistyakova, I.V.Chuvilo, V.A.Shebanov, E.M.Bogdanovicz, V.B.Vinogradov, I.A.Ivanovskaya, T.I.Kanarex, V.A.Maximenko, Z.I.Ogrzevalski, L.S.Okhrimenko, Z.S.Strugalski, Physics Letters 33B, 377 (1970).

   (c) The results of 2(a) and the average result of 2(b) indicate that $|\eta^{+-}-\eta^{oo}| < 1/2\ |\eta^{+-}|$. This indicates that the observed CP violation in the $K \to 2\pi$ decay mode cannot be accounted for solely with a CP violating $K \to 2\pi$ transition amplitude.

3. J. Marx, D. Nygren, J. Peoples and J. Steinberg, Physics Letters 32B, 219 (1970) obtain $\delta = (3.22 \pm .29)\times10^{-3}$ from an average of their experiment with a previous experiment. Combining this result with the compilation of "X" in Table 9 (Chapter V) we get

$$\mathrm{Re}\,\epsilon = 1/2\ \frac{|1-X|^2}{1-|X|^2}\ \delta = (1.55 \pm .15)\times10^{-3}.$$

   The definition of δ is: $\delta = \dfrac{\Gamma(K_L\to\pi^-\ell^+\nu)-\Gamma(K_L\to\pi^+\ell^-\nu)}{\Gamma(K_L\to\pi^-\ell^+\nu)+\Gamma(K_L\to\pi^+\ell^-\nu)}$.

4. T. D. Lee and L. Wolfenstein, Phys. Rev. 138B, 1490 (1965).

5. S. L. Glashow, Phys.Rev.Letters 14, 35 (1965).

6. L. Cabibbo, Symmetries in Elementary Particle Physics, p.285, edited by A. Zichichi, Academic Press, New York and London (1964).

7. Cronin, XIVth International Conference on High Energy Physics, Vienna, 285 (1968).

8. K. R. Schubert, B. Wolff, J.C. Chollet, J. M. Goillard, M.R. Jone, T. J. Ratcliffe, And J. P. Repellin, Physics Letters 31B, 622 (1970).

9. T. D. Lee and C. S. Wu, Annual Review of Nuclear Science 16, 533 (1966).

10. T. D. Lee and C. S. Wu, Annual Review of Nuclear Science 16, 519 (1966).

11. O. I. Dahl, L.M. Hardy, R. I. Hess, J. Kirz, and D. H. Miller, UCRL-16978 (1967).
O.I.Dahl, L.M.Hardy, R.I.Hess, J. Kirz, D.H.Miller, and J.Schwartz, UCRL-17217 (1967).

12. M.G. Albrow, D. Aston, D.P.Barber, L.Bird, R.J.Ellison, C.Halliwell, R.E.H.Jones, A.D.Kanoris, F.K.Loebinger, P.G.Murphy,M.Strong, J.Walters, A.J.Wynroe, D.D.Yovanovic, and R.F.Templeman. Physics Letters 33B, 516, (1970).

13. C.A.Heusch and C.Y.Prescott, IEEE Trans. in Nuclear Sci. Vol. NS-12, No.4, 213 (1965).

14. Particle Data Group, Reviews of Modern Physics, 43, 513 (1971).

$\tau_S = \frac{1}{\gamma_S} = .862\times10^{-10}$ sec $(.862 \pm .006)\times10^{-10}$ sec.

$\tau_L = (5.172 \pm .043)\times10^{-8}$ sec.

$(M_K - M_L) = (.5398 \pm .0033)\times10^{10}\ \hbar\ \text{sec}^{-1}$.

15. B. Aubert, L. Behr, F. L. Canavan, L.M.Chounet, J.P.Lowys, P.Mittner, C. Pascaud, Physics Letters 17, 59 (1965).

16. M. Baldo-Ceolin, E. Calimani, S.Ciampolillo, C.Filippi-Filosofo, H.Huzito, F.Mottiolli, and G.Miari. Nuovo Cimento 38, 684 (1965).

17. P.Franzini, L.Kirsch, P.Schmidt, J.Steinberg, and R.J.Plano. Phys. Rev. 140, B127 (1965).

18. L.Feldman, S.Frankel, V.L.Highland, T.Sloan, O.B.Van Dyck, W.D.Wales, R.Winston, D.M.Wolfe, Phys.Rev. 155, 1611 (1967).

19. Y.Cho, A.Dralle, J.Canter, A.Engles, H.Fisk, R.Kraemer, C.Meltzer, D.G.Hill, M.Sakitt, O.Skjeggestad, T.Kikuchi, D.K.Robinson, and C.Tilger, Phys.Rev. D1, 3031 (1970).

20. B.R.Webber, F.T.Solmitz, F.S.Crawford, and M.Alston-Garnjost, Phys. Rev. D3, 64 (1971).

21. F.James and H. Briand, Nucl.Phys. B8, 365 (1968).

22. L.S.Littenberg, J.H.Field, O.Piccioni, W.A.W. Wehlhop, S.S. Murty, P.H.Bowles, and T.H.Burnett, P.R.L. 22, 654 (1969).

23. F. J. Sciulli, J.D.Gallivan, D.M.Binnie, R. Gomez, M.L.Mallary, C.W. Peck, B.A. Sherwood, A.V. Tollestrup and J.D. van Putten, Phys.Rev.Letters 25, 1214 (1970).

24. This is the result of the Ke_3 measurement that was done as a companion experiment to the $K \to 3\pi$ experiment reported in this thesis. For greater details see J.D. Gallivan, California Institute of Technology, Doctoral Dissertation, 1970.

25. P.M. Mautsch, A. Abashian, M.F. Graham, L.H. Jones, J.R. Orr, J. H. Smith, R.D. Stutzke, M.J.Glaubman, Preprint C001195-210 (1971) University of Illinois, Urbana.

26. G. Neuhofer, F. Niebergall, M. Regler, H.E.Stier, K.Winter, J.J.Aubert, X. de Bouard, V. Lepeltier, L. Massonnet, H. Pessard, M.Vivargent, T. R. Willitts, M. Yvert, W. Bartl, and M. Steuer, paper 208 submitted to the Amsterdam International Conference on Elementary Particles (1971). See also CERN Report Number 71-3131 by K. Winter.

27. M. F. Graham. Abashian, L.H. Jones, P.M. Mautsch, J.R.Orr, J.H. Smith, R.D. Stutzke and M.J.Glaubman, Preprint C00-1195-208 (197), University of Illinois, Urbana.

28. D. Haidt, J. Stein, S. Natali, G. Piscitelli, F. Romano, E. Fett, J. Lemonne, T.L. Pederson, S.N. Tovey, V. Brisson, P.Petian, C.D.Esveld, J.J.M.Timmermans, B. Aubert, L.M.Chounet, LeDong, F. Bobisut, H.Husita, F. Sconza, A. Morzari-Chiesa, and A.E. Werbrouck, Phys.Rev.D3,10 (1971).

29. M.J.Longo, K.K.Young, J.A. Helland, Phys.Rev.181 , 2808 (1969).

30. Y. Cho, A. Dralle, J.Canter, A. Engler, H.Fisk, R. Kraemer, C. Meltzer, D.G. Hill, M.Sakitt, O. Skjeggestad, T. Kikuchi, D.K.Robinson, and C. Tilger, Phys.Rev. D3, 1557 (1971).

31. G. W. Meisner, W.A. Mann, S.S. Hertzbach, R.R. Kofler, S.S.Yamamoto, D. Berlez, S.P. Yamin, J. Thompson, and W.J.Willis, Phys.Rev. D3, 59 (1971).

32. L. Behr, V. Brisson, P.Petian, E. Bellotti, A.Pullia, M.Baldo-Ceolin, E.Calimani, S.Ciampolillo, H.Huzita, A. Sconza, B.Aubert, L.M.Chounet, J.P.Lowys, C.Pascaud, Physics Letters 22, 540 (1966).

33. J.A.Anderson, F.L.Crawford, R.L.Golden, D.Stern, T.O.Binford, V.G.Lind, P.R.L.14, 475 (1965); 15, 645 (1965).

34. B.R.Weber, F.T. Solmitz, F.S. Crawford, M.Alston-Garnjost, Phys.Rev. D1, 1967 (1970).

35. F.James, L.Montauet, E.Paul, E. Pauli, P.Soetre, D.M.Sendall, G.Burgun, E.Lesavoy, A. Muller, S. Zylberajch, and O.Skjeggestad, Physics Letters 35B, 265 (1971).

36. J.J.Aubert, G.Neuhofer, F.Niebergall, M.Regler, H.E.Stier, K.Winter, X. de Bouard, V. Lepeltier, L.Massonnet, H.Pessard, M.Vivargent, T.R.Willitts, M. Yvert, W. Bartl, M.Stever, paper 209 submitted to the Amsterdam International Conference of Elementary Particles (1971).

37. L.H.Jones, A. Abashian, M.F.Graham, P.M.Mautsch, J.R.Orr, J.H.Smith, R.D.Stutzke, and M.J.Glaubman, preprint COO-1195-209 (1971), University of Illinois, Urbana.

38. T.D.Lee and C.S. Wu, Annual Review of Nuclear Science 16, 478 (1966).

39. J.H.Field, Possible Contributions of $\Delta S=-\Delta Q$ amplitudes to Ke_3 Decay Rates, RHP/H/51, Rutherford High Energy Laboratory, December (1968).